UNIVERSITY OF CALIFORNIA SAN DIEGO

The Metabolic Plasticity of Lipid Synthesis in Cancer Cells

A dissertation submitted in partial satisfaction of the
requirements for the degree
Doctor of Philosophy

in

Bioengineering

by

Avi Kumar

Committee in charge:

Professor Christian Metallo, Chair
Professor Stephanie Fraley
Professor Nathan Lewis
Professor Alan Saghatelian
Professor Shankar Subramaniam

2021

The dissertation of Avi Kumar is approved, and it is acceptable in quality and form for publication on microfilm and electronically.

University of California San Diego

2021

DEDICATION

To my parents, Dr. Vipin and Renu Kumar, for their encouragement, support, and commitment to my success.

TABLE OF CONTENTS

LIST OF FIGURES

LIST OF TABLES

ACKNOWLEDGEMENTS

I have many people to thank for the completion of this work. First and foremost, I would like to thank my advisor, Dr. Christian M. Metallo, for his encouragement and mentorship throughout my graduate studies. I would not have been able to grow as much as I have without the opportunities he has afforded me and the cordial research environment he has cultivated in his group. I want to thank current and former members of the Metallo lab: Courtney Green, Thekla Cordes, Martina Wallace, Mehmet Badur, Thangaselvam Muthusamy, Esther Lim, Jivani Gengatharan, Michal Handzlik, Grace McGregor, Anna Trimble, Karl Wessendorf-Rodriguez, Ramya Kuna, Sanika Khare and Jack Mitchener. It has been a pleasure to work with and learn from all of you. I'm excited to see how our paths cross in the future. I would also like to thank my collaborators throughout the years for their invaluable guidance, especially Zachary A. King and Robert U. Svennson.

I want to thank the friends I've made in San Diego and beyond for providing welcomed breaks, especially during the events of the past couple of years. I thank my parents, as well as my siblings and their growing families for their unlimited supply of love and laughter. Finally, I want to thank Leah Shepersky for being my constant source of joy.

Chapter 1, is an introductory chapter which covers the literature and techniques relevant to this work. The topics that are covered include the metabolic reprogramming of diseased cells, fatty acid metabolism, mass spectrometry, and the analysis of stable isotope tracing studies.

Chapter 2, in full, is a reprint of the material as it appears in "NaCT/SLC13A5 facilitates citrate import and metabolism under nutrient-limited conditions" Cell Reports, vol. 36, 2021. Avi Kumar is the primary author of this publication. Thekla Cordes, Anna E. Thalacker-Mercer, Ana M. Pajor, and Anne N. Murphy are co-authors on the paper. Christian M. Metallo is the corresponding author of this publication.

Chapter 3 is currently being prepared for submission for publication. Avi Kumar is the primary author of this publication. Ramya Kuna, Hector Galvez, Grace H. McGregor, Courtney

R. Green, Thekla Cordes, Reuben J. Shaw, Robert U. Svensson are co-authors on the paper. Christian M. Metallo is the corresponding author of this publication.

Chapter 4, in full, is a reprint of the material as it appears in "Escher-Trace: A Web Application for Pathway-Based Visualization of Stable Isotope Tracing Data" BMC Bioinformatics, vol 21, 2020. Avi Kumar is the primary author of this publication. Jack Mitchener and Zachary A. King are co-authors on the paper. Christian M. Metallo is the corresponding author of this publication.

Chapter 5 is currently being prepared for submission for publication. Avi Kumar is the primary author of this publication. Christian M. Metallo is the corresponding author of this publication.

VITA

2021	Ph.D. in Bioengineering, University of California San Diego
2016	B.S. in Chemical Engineering, University of Minnesota Twin Cities

PUBLICATIONS

Kumar A, Cordes, T, Thalacker-Mercer, AE, Pajor, A, Murphy A, Metallo, CM. (2021) NaCT/ SLC13A5 facilitates citrate import and metabolism under nutrient-limited conditions. *Cell Reports*, vol. 36, 2021.

Yebra, M, Bhargava, B, **Kumar A**, Burgoyne, A, Tang, C, Yoon, H, Banerjee, S, Aguilera, J, Cordes, T, Sheth, V, Noh, S, Ustoy, R, Li S, Advani, S, Corless, C, Heinrich, M, Kurzrock, R, Lippaman, S, Fanta, P, Harismendy, O, Metallo, CM, Sicklick, J. (2021) Establishment of Patient-derived Succinate Dehydrogenase-deficient Gastrointestinal Stromal Tumor Models For Predicting Therapeutic Response. In Press at *Clin. Cancer Res.*

Su, H, Yang, F, Fu, R, Li, X, French, R, Mose, E, Pu, X, Trinh, B, **Kumar A**, Liu, J, Antonucci, L, Todoric, J, Liu, Y, Hu, Y, Diaz-Meco, MT, Moscat, J, Metallo, CM, Lowy AM, Sun B, Karin M. (2021) Cancer cells escape autophagy inhibition via NRF2-induced macropinocytosis. *Cancer Cell* 39(5): 678-693.

Ravi, A, Palamiuc, L, Loughran, RM, Triscott, J, Arora, G.K, **Kumar A**, Tieu, V, Pauli, C, Reist, M, Lew, R.J, Houlihan, S.L, Fellmann, C, Metallo, CM, Rubin, M.A, Emerling, B.M. (2021) PI5P4Ks drive metabolic homeostasis through peroxisome-mitochondria interplay. *Dev. Cell* 56(11): 1661-1676.

Kumar A, Mitchener, J, King, ZA, Metallo CM. (2020) Escher-Trace: a web application for pathway-based visualization of stable isotope tracing data. *BMC Bioinformatics* 21(297).

Jin, L, Chun, J, Pan, C, **Kumar A**, Zhang, G, Ha, Y, Li, D, Alesi, G.N, Kang, Y, Zhou, L, Yu, W.M, Magliocca, K.R, Khuri, F.R, Qu, C.K, Metallo, CM, Owonikoko, T.K, Kang, S. (2018) The PLAG1-GDH1 Axis Promotes Anoikis Resistance and Tumor Metastasis through CamKK2-AMPK Signaling in LKB1-Deficient Lung Cancer. Mol. Cell 69(1): 87-99.

CONFERENCE PRESENTATIONS

Kumar A, et al. (2021) The Metabolic Plasticity of Lipid Synthesis in Cancer Cells. (Presentation) Toran Therapeutics. Cambridge, MA.

Kumar A, et al. (2021) The Metabolic Plasticity of Lipid Synthesis in Cancer Cells. (Presentation) Agios Pharmaceuticals. Cambridge, MA.

Kumar A, et al. (2021) The Metabolic Plasticity of Lipid Synthesis in Cancer Cells. (Presentation) Calico Life Sciences. South San Francisco, CA.

King ZA, Kumar A, et al. (2019) Interactive Metabolic Pathway Visualization for Optimization of Energy Flux. (Poster) Genomic Sciences Program Annual Principal Investigator Meeting. Fairfax, VA.

ABSTRACT OF THE DISSERTATION

The Metabolic Plasticity of Lipid Synthesis in Cancer Cells

by

Avi Kumar

Doctor of Philosophy in Bioengineering

University of California San Diego, 2021

Professor Christian Metallo, Chair

The metabolic network has evolved over millennia into an intricate system of reactions which maintain cellular homeostasis. Highly proliferative cells, including cancers, reprogram the network to sustain elevated biomass accumulation. Lipid metabolism, in particular, is critical to support growth as these complex molecules serve numerous essential roles in cell biology. The chapters of this thesis are all independent bodies of work which explore mechanisms of fatty acid reprogramming in mammalian cells as well as present software tools which expedite analysis of metabolic studies. Chapter 1, titled “Profiling fatty acid metabolism in cancer cells using stable isotope tracing” is a review of relevant literature concerning the rewiring of central carbon and lipid metabolism under highly proliferative disease states as well as the utility of

stable isotope tracing and metabolic modeling. Chapter 2, titled "NaCT/SLC13A5 facilitates citrate import and metabolism under nutrient-limited conditions" quantifies the contribution of NaCT-mediated citrate uptake to central carbon metabolism in multiple cell systems. The findings demonstrated that citrate uptake promoted lipogenesis and proliferation in glutamine deprived conditions, as well as increased tolerance to zinc-induced toxicity. Chapter 3, titled "ATP-citrate lyase deficiency highlights critical sources of lipogenic acetyl-CoA in cancer cells" describes how multiple layers of redundancy support lipogenic acetyl-CoA synthesis. Cells were found to rely on non-canonical sources of acetyl-CoA including *de novo* acetate synthesis, and peroxisomal β-oxidation when deficient in functional ATP-citrate lyase (ACLY). Chapter 4, titled "Escher-Trace: A Web Application for Pathway-Based Visualization of Stable Isotope Tracing Data" describes a web-based visualization platform for analyzing stable isotope tracing data with the context of metabolic pathway architecture. The software simplifies the analytical pipeline for nominal resolution stable isotope tracing measurements, by automating multiple intermediary steps including natural isotope correction and data plotting. Chapter 5, titled "Analysis of high-resolution lipidomic data with Escher-Trace" details an analytical pipeline for analysis of high-resolution mass spectrometry (HRMS) data which incorporates the Escher-Trace platform. By expanding the feature set of Escher-Trace and introducing an intermediary script connecting the platform to existing HRMS analysis software, the pipeline is found to expedite analysis of complex HRMS datasets. Overall, these findings reveal compensatory mechanisms employed upon disruption of canonical lipogenesis as well as provide tools which contextualize stable isotope tracing data and facilitate analysis of metabolic studies.

Chapter 1

Profiling fatty acid metabolism using stable isotope tracing

1.1 Introduction

Lipid metabolism is dysregulated in numerous diseases including cancer, diabetes mellitus, fatty liver disease, and lysosomal storage diseases among others [1–4]. Fatty acids are the primary components of lipids and are utilized for a number of essential cellular processes such as membrane synthesis, cell signaling, protein modification, and energy storage. The primary source of fatty acids for nearly all somatic cells in the human body is dietary fat. Highly proliferative cells are often exposed to nutrient limited conditions and have been shown to upregulate *de novo* synthesis of fatty acids to sustain their growth. For this reason, the *de novo* lipogenic (DNL) pathway is believed to have a significant therapeutic window for cancer therapy. The subject of this dissertation is the plasticity of lipid metabolism, specifically, the mechanisms utilized by cells to compensate for disruption in canonical lipid synthesis. My studies have focused on perturbing fatty acid metabolism, by both genetically targeting enzymes in the DNL pathway as well as depleting the nutrients which feed the pathway, and observing downstream ramifications

on cell growth as well as broader metabolism using stable-isotope tracing, mass spectrometry, and quantitative flux modeling. Furthermore, I worked to advance tools for visualization and analysis of complex stable isotope tracing datasets.

1.2 Metabolically active cells are highly biosynthetic

Metabolism is the set of intracellular chemical processes responsible for nutrient break down, energy generation, macromolecule biosynthesis, and waste elimination which are essential for maintenance of cellular homeostasis. Over millennia, the mammalian metabolic network has evolved into a vast interconnected system of reactions with multiple layers of control, enabling cells to meet numerous functional requirements and thrive in disparate environments. This is evident in the human body where diverse cell types are responsible for anabolism and catabolism of distinct compounds despite operating with the same network blueprint. When the blueprint is mutated or control systems are overwhelmed, metabolic disease states emerge.

To maintain rapid growth, highly proliferative cells sustain continuous macromolecule biosynthesis by upregulating consumption of glucose, amino acids, and fatty acids. This process, in addition to poor tumor vascularization, often leave cancer cells in nutrient depleted environments [5]. To compensate, cells reprogram their metabolism and rely on alternative nutrient sources such as lactate, branched chain amino acids, and ketone bodies [6, 7]. Reprogramming methods that support processes central to maintaining proliferation, such as lipid synthesis, are promising targets for therapeutic intervention as their disruption has the potential to significantly impact transformed cells while leaving healthy tissue intact.

The classic example of metabolic reprogramming in cancer cells is the Warburg effect which was the observation in the 20^{th} century that even in aerobic conditions cancer cells favored energy generation by glycolytic flux rather than mitochondrial oxidative phosphorylation [8]. As a result of this phenomena, the amount of glucose carbon flux shuttled to the mitochondria

is significantly reduced as glycolytically derived pyruvate is fermented to lactate. Because less glucose carbon enters the mitochondria, glucose's contribution to mitochondrial tricarboxylic acid (TCA) cycle intermediates, including citrate, is reduced. In lipogenic cells, including cancer cells, mitochondrial citrate is exported to the cytosol by the mitochondrial citrate carrier and can be utilized for synthesis of cytosolic acetyl-CoA and *de novo* lipogenesis.

In recent decades it has been shown that highly proliferative cells are able to compensate for this loss of glucose carbon flux by reductively catabolizing glutamine derived α-ketoglutarate to citrate by the reductive action of isocitrate dehydrogenase and aconitase (Figure 1). This reductive TCA flux is further upregulated when the cells are exposed to hypoxia, resulting in the majority of *de novo* fatty acid carbon being derived from glutamine *in vitro* [9–11].

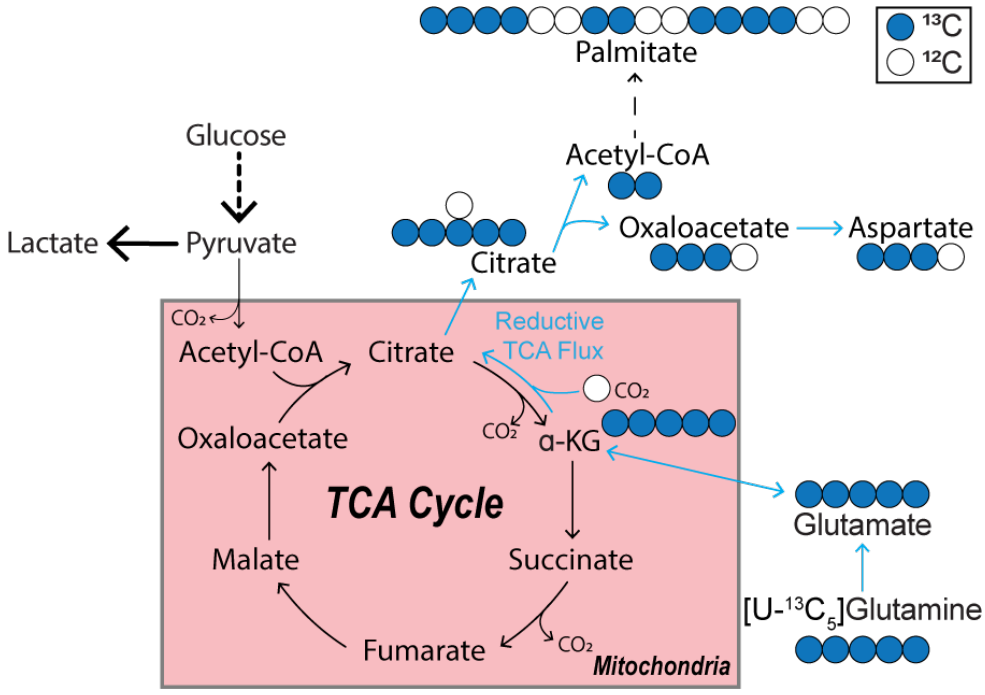

Figure 1.1: **Metabolic Reprogramming in Cancer Cells.** Pathway map of central carbon metabolism, highlighting the pyruvate fermentation (Warburg effect) as well as glutaminolysis and reductive carboxylation with colored circles signifying ^{13}C labeled atoms and white circles signifying ^{12}C unlabeled atoms.

However reproducing the reductive glutamine phenotype *in vivo* has generated mixed results [12–15]. This may be due to the significant difference in nutrient profile of cell culture

media compared to *in vivo* microenvironments [16–18]. Plasma and interstitial fluid have complex nutrient profiles and contain metabolites which impact cellular metabolism but are routinely excluded from common experimental medias. Citrate is abundant in plasma, however absent in most cell culture medias, thus its impact may be overlooked in many *in vitro* studies. Synthesized in the mitochondria by citrate synthase, citrate serves as a critical substrate for biosynthesis, acetylation, and the regeneration of NAD(P)H via the tricarboxylic acid cycle [19]. Import of extracellular citrate is of particular interest in lipogenic tissues as it theoretically provides the most direct mechanism for feeding *de novo* lipogenesis.

The only plasma membrane transporter in mammals known to preferentially import citrate into cells is the sodium-dependent citrate transporter (NaCT), which is encoded by *SLC13A5* also known as mINDY. Expression of *SLC13A5* is highly tissue specific, with transcription primarily occurring in the liver and brain [20, 21]. Multiple studies have linked the expression and activity of NaCT to hepatic glucose and fatty acid metabolism. Specifically, *SLC13A5* was found to be upregulated in patients with nonalcoholic fatty liver disease (NAFLD) and targeting NaCT pharmacologically as well as genetically attenuates hepatic lipogenesis [22–24]. Furthermore, loss-of function mutations in *SLC13A5* are linked to pediatric epilepsy and other brain disorders [25–29].

In chapter 2 we confirmed that hypoxia upregulates reductive glutamine catabolism in hepatocellular carcinoma cells (HCC) and observed that extracellular citrate addition reduced flux through this pathway. We profiled the ability of *SLC13A5* expressing hepatoma cells to take up and catabolize extracellular citrate. We found that the hepatoma cells reliance on extracellular citrate for TCA anaplerosis, fatty acid synthesis, as well as toxic metal ion tolerance increases with nutrient limitation (O_2, glutamine depletion) and show that these phenotypes are reversed upon genetically targeting NaCT with CRISPR/Cas9. Our results suggest that extracellular citrate is not a major biosynthetic substrate in nutrient rich conditions, however, it is an important resource to cells experiencing severe stresses (e.g. hypoxia, amino acid deprivation, metal toxicity).

1.3 Lipid metabolism is a complex and resilient multi-organelle process

Lipids are essential for cell structure, energetics, and biological function. The molecular diversity of lipid species is vast, with thousands of identified species, categorized across eight classes (fatty acyls, glycerolipids, glycerophospholipids, sphingolipids, sterols, prenol lipids, saccharolipids, and polyketides) [30, 31]. Several lipid classes are known to serve distinct roles in the cell, for example sterols control membrane fluidity and are a precursor for steroid hormone synthesis, triacylglycerides are the primary mode of energy storage, and glycerophospholipids are the dominant component of lipid membranes with further structural and functional classification based on headgroup composition (e.g. those with inositol head groups, known as phosphatidylinositols, are involved in cell signaling cascades) [32]. Lipid metabolism spans multiple organelles, with synthesis of subunits including fatty acids, mevalonate, amino acids, and glycerol occurring in the cytosol, fatty acid modification along with membrane lipid assembly taking place in the endoplasmic reticulum (ER), lipid degradation actioned in the lysosome, and further fatty acid oxidation transpiring in the mitochondria and peroxisome [33]. A variety of disease states emerge from dysregulation of lipid metabolism including type 2 diabetes, heart disease, obesity, Gaucher's disease, and Tay Sachs disease among others [34, 35]. Furthermore, many cancer cells exhibit high rates of lipid synthesis and turnover to support growth and survival [9, 36, 37].

Fatty acids are esterified to multiple types of lipid backbones such as glycerol in glycerolipids and ceramide derived sphingoid bases in sphingolipids. In addition to being incorporated into lipids, fatty acids are utilized for protein modification and cell signaling [38]. Variation in acyl chain length, saturation level, and double bond cis/trans isomerism impart unique attributes to fatty acids. Most fatty acids in mammalian cells are capable of being synthesized intracellularly from the 16-carbon straight chain fatty acid palmitate. However, essential fatty acids (EFAs),

omega-6 alpha-linoleic acid and omega-3 linoleic acid, must be derived from the diet in humans [38]. While nearly all healthy tissues rely on uptake of dietary lipids to maintain lipid homeostasis [39], *de novo* lipogenesis is active in only a few somatic cell types (specifically liver, adipose, and lactating mammary gland tissue). However DNL is required for proliferation of many tumor types [40, 41].

De novo fatty acids are synthesized from two carbon acyl-units provided by cytosolic acetyl-CoA. Canonically, mitochondrial citrate is exported to the cytosol and catabolized by ATP-Citrate Lyase (ACLY) to generate acetyl-CoA, as described earlier. Acetate has also been found to contribute to cytosolic acetyl-CoA by the action of acetyl-CoA synthetase (ACSS2) [37, 42]. This cytosolic acetyl-CoA is then elongated by acetyl-CoA Carboxylase (ACC) and subsequently fatty acid synthase (FASN) ultimately generating palmitate (Figure 2). Fatty acids can be further modified by elongation (ELOVL1-7) or desaturation (SCD, FADS1-3) and incorporated into lipids in the ER [43].

Numerous inhibitors have been developed to target *de novo* lipogenic enzymes for both treatment of cancers and metabolic diseases. Pharmacological inhibition of FASN reduces body weight of mice [44] as well as oncogene expression [45] and *in vivo* tumor growth [46] of human breast cancer cell lines. Targeting acetyl-CoA carboxylase, both genetically and pharmacologically, decreases fatty acid synthesis and tumor proliferation *in vivo* [47]. Additionally, in patients with hepatic steatosis, liver specific inhibition of ACC significantly reduced hepatic lipogenesis and steatosis [48]. A study analyzing patient data across 101,236 participants found that specific single nucleotide polymorphisms (SNPs) in ACLY were associated with reduced low-density lipoprotein cholesterol (LDL-C) levels and reduced incidence of major cardiovascular events [49]. Furthermore, ACLY is overexpressed in a number of cancers and higher expression is associated with worse patient prognosis in multiple cancers [50–56]. High expression of ACSS2 is also associated with poor prognosis in breast, glioblastoma, ovarian, and lung cancers [42, 57, 58]. Interest in developing inhibitors of these cytosolic acetyl-CoA synthesizing enzymes is growing

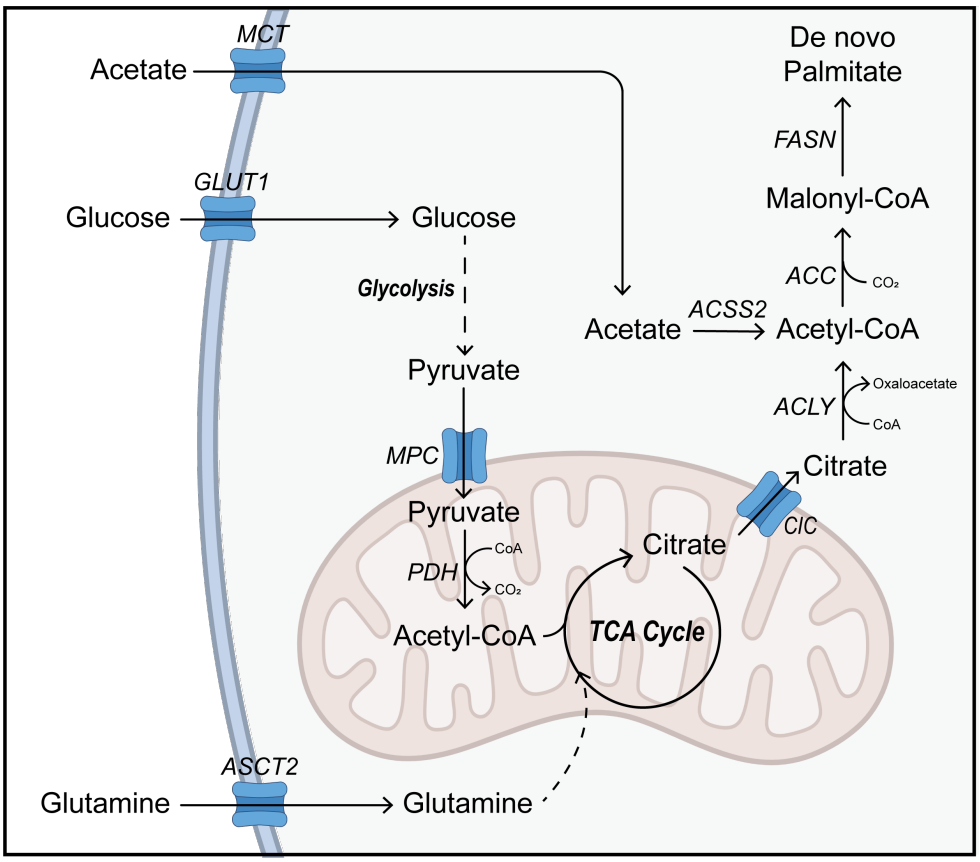

Figure 1.2: ***De novo* Synthesis of Fatty Acids.**Pathway map of *de novo* lipogenesis and the nutrients which fuel the pathway. Abbreviations: ACC: acetyl-CoA Carboxylase, ACLY: ATP-Citrate Lyase, ACSS2: acetyl-CoA synthetase isoform 2, ASCT2: alanine, serine, cysteine transporter 2, CIC: the citrate carrier, FASN: fatty acid synthase, GLUT1: glucose transporter 1, MCT: monocarboxylate transporter, MPC: mitochondrial pyruvate carrier, PDH: pyruvate dehydrogenase

across multiple therapeutic arenas as cytosolic acetyl-CoA is utilized for fatty acid synthesis as well as cholesterol synthesis and protein acetylation [59–62]. The liver specific ACLY inhibitor bempedoic acid was recently FDA approved for treatment of high cholesterol [63, 64]. Although not a canonical source of lipogenic acetyl-CoA, peroxisomal metabolism is known to generate acetyl-CoA through oxidation of very long chain fatty acids (VLCFA) and branched chain fatty acids (BCFA). Previous studies have found that peroxisomal acetyl-CoA contributes to protein acetylation in hepatic tissue [65]. Furthermore, enzymes involved in peroxisomal β-oxidation of BCFAs (ACOX3 and HSD17B4) are overexpressed in prostate tumors compared to surrounding healthy tissue [66].

As shown in chapter 3, lipogenic acetyl-CoA synthesis is highly elastic in cells. We were interested in identifying how impeding lipogenic acetyl-CoA synthesis would alter fatty acid metabolism and proliferation of lipogenic cells. By genetically targeting ACLY and/or ACSS2, in non-small cell lung cancer and hepatoma cell lines we confirmed that ACLY-deficiency reduced *de novo* lipogenesis, reduced cell viability, and increased reliance on extracellular lipids. ACSS2 expression and acetate utilization were upregulated upon knockout of ACLY, with supplemental acetate becoming the primary lipogenic substrate in multiple ACLY-KO cell lines. Targeting both ACLY and ACSS2 (DKO) induced a growth limiting stress even when cells were cultured in nutrient rich media. However, both ACLY-KO cells and DKO cells sustained some proliferation and maintained protein acetylation comparable to wildtype, suggesting the existence of alternative acetyl-CoA generating mechanisms. Fatty acid oxidation became a significant source of lipogenic acetyl-CoA in ACLY-KO and DKO cell lines and there was a distinct depletion of lipids containing very long chain fatty acids in these cells. Additionally, growth of ACLY-KO and DKO cells was sensitive to Thioridazine, a peroxisomal β-oxidation inhibitor, suggesting that peroxisomal β-oxidation plays an outsized role in supporting acetyl-CoA synthesis and growth in the knockout lines. Collectively, our results highlight the critical roles of biosynthetic and catabolic lipid metabolism in maintaining acetyl-CoA levels in lipogenic cells, particularly in the context of

targeting ACLY.

1.4 Mass spectrometry can elucidate changes in metabolism and *de novo* lipogenesis

Mass spectrometry is an invaluable tool for studying metabolism. Consisting of an ion source, which ionizes a sample of interest, a mass filter, which allows passage of select ions based on mass to charge ratio (m/z), and a detector, which counts the filtered ions, mass spectrometers generate mass spectra which provide m/z "fingerprints" that can be decoded to quantify the molecular composition of tested samples. In the mid-20th century, mass spectrometers were paired to gas- and liquid-chromatography (GC-MS, LC-MS/MS) separation systems, making unambiguous identification of molecular components possible. Currently GC-MS and LC-MS/MS techniques are a core technology utilized across numerous sectors including forensics, toxicology, food science, plant science, and medicine [67]. Further advancements in chromatography, mass spectrometry, and nuclear magnetic resonance (NMR) technology have allowed for robust quantitation of small molecules (metabolomics) as well as macromolecules (lipidomics, proteomics) enabling unprecedented insight into cellular function. However, static measurements of molecule abundances provide a narrow perspective on the metabolic state of a system. To gain biologically relevant insight, flux through metabolic pathways must be observed. Stable isotope tracing studies are the current state-of-the-art method for investigating intracellular fluxes [68, 69]. Alterations in tricarboxylic acid [70, 71], serine [72], branched chain amino acids [73, 74], and NAD(P)H metabolism [75–77] have been identified by applying tracer studies to a variety of cell and organ systems. These investigations consist of administering stable isotope labeled metabolites to an *in vitro* or *in vivo* system and measuring the isotopic labeling distributions, resulting from catabolism of the tracer and distribution of its heavy isotopes across the metabolic network. The mass isotopomer distributions (MIDs) are used to make direct inferences about metabolic flux or

inserted into metabolic flux analysis models to quantitatively estimate intracellular fluxes.

^{13}C Metabolic flux analysis (MFA) is a modeling approach which utilizes a metabolic network with defined atom transitions, extracellular flux measurements, cell growth rates, and stable isotope tracing data to quantitatively estimate intracellular fluxes in an unbiased manner. For commonly used steady state MFA two key assumptions are made, the first is that the cells are operating at metabolic steady state, meaning there is no net accumulation of metabolites beyond those accounting for an increase in cell biomass, and the second is that the cells are operating at isotopic steady state, meaning that the labeling distributions resulting from catabolism of the applied tracer are not changing over time [69]. The models generate simulated labeling distributions of all network metabolites and modulate prospective intracellular flux values to minimize the sum of squared residual (SSR) between the simulated and experimentally determined MIDs. Recently, advances in algorithms designed to solve ^{13}C MFA models, through use of the elementary metabolite units (EMU) framework, in addition to the availability of user-friendly software packages, such as INCA, have made stable isotope labeled MFA an important tool in metabolic engineering and basic science research [78, 79]. In chapter 2 we generated a ^{13}C MFA model of compartmentalized central carbon metabolism to confirm that extracellular citrate, taken up by hepatoma cells, is directly catabolized in the cytosol.

Isotopomer spectral analysis (ISA) is an additional modeling approach used to estimate polymer biosynthesis (g(t) value) and precursor pool dilution (D value) from a stable isotope tracer of interest. The models consist of a set of nonlinear equations, defined by combinatorial probability theory as functions of the g(t) and D values, which characterize the expected fractional abundance of all possible isotopologues of a polymer [80, 81]. Nonlinear regression is used to adjust the g(t) and D values and minimize the error between the simulated MIDs and the experimental MIDs of the polymer resulting from catabolism of the applied tracer. A classic ISA model commonly used in stable isotope tracing studies is of palmitate synthesis [82]. Using this model, the fraction of newly synthesized palmitate and fraction of lipogenic acetyl-CoA precursor

enriched by the applied tracer are estimated. In both chapters 2 and 3 we used the palmitate ISA to quantify fatty acid synthesis and observed alterations to the contributions of lipogenic substrates to fatty acid synthesis with either introduction of unique nutrient availability or genetic and/or pharmacological inhibition of lipogenic enzymes.

Metabolite abundances and labeling distributions are a product of intracellular fluxes as well as metabolic pathway architecture. However, stable isotope tracing data sets are typically presented in large data tables containing the abundances and labeling patterns for measured compounds across all samples. Without significant background knowledge of metabolism, interpretation of these data tables is prohibitively difficult. Furthermore, reporting metabolomics and tracing results often involves normalizing and plotting the data numerous times. Thus, identifying novel insights from tracing experiments is extremely time consuming when dealing with a large number of metabolites or samples. A tool which automates these intermediary steps and presents metabolite abundances and isotopologue distributions in the context of metabolic networks would accelerate analysis of tracing experiments as well as make the data accessible to the broader scientific community. In chapter 4 we showcase Escher-Trace, a web-based visualization platform for stable isotope tracing data which facilitates evaluation of tracing datasets in the context of a metabolic network. The software allows users to correct for natural isotope abundance, generate publication quality graphs of metabolite labeling, and present data in view of Escher pathway maps [83] (Figure 3). As an open-source GitHub project, Escher-Trace will continue to expand and improve. Although originally designed for interpretation of nominal resolution data generated by GC-MS systems, in chapter 5 we extend the functionality of Escher-Trace to allow for analysis of data from high-resolution mass spectrometer systems through compatibility with El-MAVEN, a widely used software for integration of high-resolution MS data. Escher-Trace has proven to be a valuable tool in the Metallo lab and has active users in the U.S. as well as internationally.

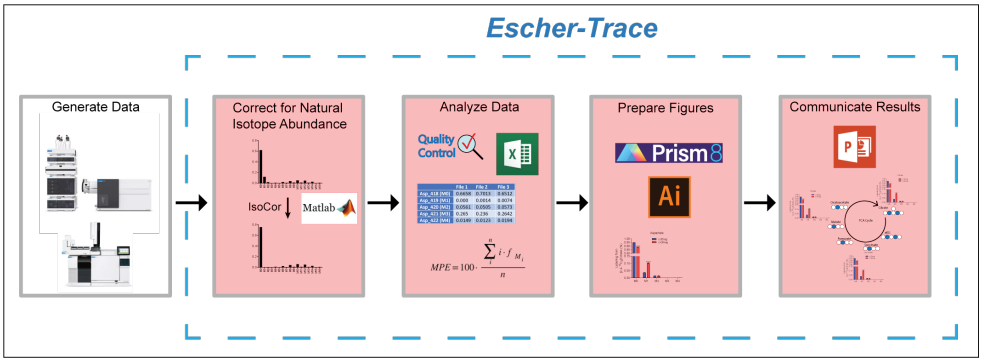

Figure 1.3: **Escher-Trace analytical pipeline.** Escher-Trace allows for natural isotope abundance correction, analysis and visualization of stable isotope labeling data sets in the context of Escher metabolic maps.

1.5 Dissertation contents

In my thesis work I used stable-isotope tracing paired with both gas- and liquid- chromatography mass spectrometry, along with MFA to quantify labeling and abundances of mitochondrial intermediates, amino acids, fatty acids, and lipids as well as intracellular pathway fluxes in cancer cells. In the following chapters, these techniques are utilized and extended to profile changes in fatty acid metabolism and cancer cell proliferation upon disruption of nutrient uptake and synthesis of key substrates.

Chapter 2, titled "NaCT/SLC13A5 facilitates citrate import and metabolism under nutrient-limited conditions" evaluates the functional roles of extracellular citrate in NaCT expressing cell types. The contribution of extracellular citrate to TCA anaplerosis and fatty acid metabolism is quantified in hepatoma and neuronal cells. We establish that citrate uptake by NaCT is protective against glutamine deprivation and zinc-induced cellular toxicity. These findings demonstrate the importance of applying a variety of stresses when evaluating the utility of non-canonical nutrient sources in lipogenic cells, as phenotypes may only be observable with application of the appropriate stress.

Chapter 3, titled "ATP-citrate lyase deficiency highlights critical sources of lipogenic acetyl-CoA in cancer cells" demonstrates that lipogenic acetyl-CoA synthesis has multiple layers

of redundancy by evaluating fatty acid synthesis and proliferation of liver and lung derived cells deficient in ATP-Citrate Lyase (ACLY) and/or acetyl-CoA Synthetase (ACSS2). Upon depletion of canonical acetyl-CoA synthesis mechanisms, fatty acid synthesis and cancer cell proliferation were found to rely on non-canonical acetyl-CoA synthesis pathways including *de novo* acetate synthesis and peroxisomal fatty acid oxidation.

Chapter 4, titled "Escher-Trace: A Web Application for Pathway-Based Visualization of Stable Isotope Tracing Data" provides a walkthrough of how to incorporate and visualize ^{13}C metabolic tracing data into the Escher-Trace data visualization platform. With Escher-Trace, users are able to correct for natural isotope abundance, generate publication quality graphs of metabolite labeling, and present data in the context of pathways. The freely available website is designed to ease interpretation of complex ^{13}C tracing data sets, by overlaying the data on Escher metabolic maps.

Chapter 5, titled "Analysis of high-resolution lipidomic data with Escher-Trace" details an extension of the Escher-Trace platform for interpretation of high-resolution lipidomic data. A data analysis pipeline is presented which expands the feature set of Escher-Trace, and provides compatibility with El-MAVEN, a widely used software for analysis of high-resolution mass spectrometer data.

1.6 Acknowledgements

Chapter 1 is an introductory chapter to this thesis. Avi Kumar is the primary author. Christian M. Metallo is the corresponding author.

1.7 References

1. Angulo, P. Nonalcoholic fatty liver disease. *New England Journal of Medicine* **346,** 1221–1231 (2002).

2. Kahn, B. B. & Flier, J. S. Obesity and insulin resistance. *The Journal of Clinical Investigation* **106,** 473–481 (2000).

3. Platt, F. M. Sphingolipid lysosomal storage disorders. *Nature* **510,** 68–75 (2014).

4. Röhrig, F. & Schulze, A. The multifaceted roles of fatty acid synthesis in cancer. *Nature Reviews Cancer* **16,** 732–749 (2016).

5. White, E. Exploiting the bad eating habits of Ras-driven cancers. *Genes and Development* **27,** 2065–2071 (2013).

6. Deberardinis, R. J. & Chandel, N. S. Fundamentals of cancer metabolism. *Science Advances* **2** (2016).

7. Puchalska, P. & Crawford, P. A. Multi-dimensional Roles of Ketone Bodies in Fuel. *Cell Metabolism* **25,** 262–284 (2016).

8. Vander Heiden, M. G., Cantley, L. & Thompson, C. Understanding the Warburg Effect: The Metabolic Requirements of Cell Proliferation. *Science* **324,** 1029 (2009).

9. Metallo, C. M., Gameiro, P. A., Bell, E. L., Mattaini, K. R., Yang, J., Hiller, K., Jewell, C. M., Johnson, Z. R., Irvine, D. J., Guarente, L., Kelleher, J. K., Vander Heiden, M. G., Iliopoulos, O. & Stephanopoulos, G. Reductive glutamine metabolism by IDH1 mediates lipogenesis under hypoxia. *Nature* **481,** 380–4 (2012).

10. Mullen, A. R., Wheaton, W. W., Jin, E. S., Chen, P. H., Sullivan, L. B., Cheng, T., Yang, Y., Linehan, W. M., Chandel, N. S. & Deberardinis, R. J. Reductive carboxylation supports growth in tumour cells with defective mitochondria. *Nature* **481,** 385–388 (2012).

11. Wise, D. R., Ward, P. S., Shay, J. E. S., Cross, J. R., Gruber, J. J. & Sachdeva, U. M. Hypoxia promotes isocitrate dehydrogenase-dependent carboxylation of α-ketoglutarate to citrate to support cell growth and viability. *Proc. Natl. Acad. Sci. U.S.A* **108,** 19611–19616 (2011).

12. Davidson, S. M., Papagiannakopoulos, T., Olenchock, B. A., Heyman, J. E., Keibler, M. A., Luengo, A., Bauer, M. R., Jha, A. K., O'Brien, J. P., Pierce, K. A., Gui, D. Y., Sullivan, L. B., Wasylenko, T. M., Subbaraj, L., Chin, C. R., Stephanopolous, G., Mott, B. T., Jacks, T., Clish, C. B. & Van Der Heiden, M. G. Environment impacts the metabolic dependencies of ras-driven non-small cell lung cancer. *Cell Metabolism* **23,** 517–528 (2016).

13. Le, A., Lane, A. N., Hamaker, M., Bose, S., Gouw, A., Barbi, J., Tsukamoto, T., Rojas, C. J., Slusher, B. S., Zhang, H., Zimmerman, L. J., Liebler, D. C., Slebos, R. J., Lorkiewicz, P. K., Higashi, R. M., Fan, T. W. & Dang, V. C. Glucose-independent glutamine metabolism via TCA cycling for proliferation and survival in b cells. *Cell Metabolism* **15,** 110–121 (2012).

14. Son, J., Lyssiotis, C. A., Ying, H., Wang, X., Hua, S., Ligorio, M., Perera, R. M., Ferrone, C. R., Mullarky, E., Shyh-Chang, N., Kang, Y., Fleming, J. B., Bardeesy, N., Asara, J. M., Haigis, M. C., Depinho, R. A., Cantley, L. C. & Kimmelman, A. C. Glutamine supports pancreatic cancer growth through a KRAS-regulated metabolic pathway. *Nature* **496,** 101–105 (2013).

15. Tardito, S., Oudin, A., Ahmed, S. U., Fack, F., Keunen, O., Zheng, L., Miletic, H., Sakariassen, P. Ø., Weinstock, A., Wagner, A., Lindsay, S. L., Hock, A. K., Barnett, S. C., Ruppin, E., Harald MØrkve, S., Lund-Johansen, M., Chalmers, A. J., Bjerkvig, R., Niclou, S. P. & Gottlieb, E. Glutamine synthetase activity fuels nucleotide biosynthesis and supports growth of glutamine-restricted glioblastoma. *Nature Cell Biology* **17,** 1556–1568 (2015).

16. Ackermann, T. & Tardito, S. Cell Culture Medium Formulation and Its Implications in Cancer Metabolism. *Trends in Cancer* **5,** 329–332 (2019).

17. Rossiter, N. J., Huggler, K. S., Adelmann, C. H., Keys, H. R., Soens, R. W., Sabatini, D. M. & Cantor, J. R. CRISPR screens in physiologic medium reveal conditionally essential genes in human cells. *Cell Metabolism* (2021).

18. Voorde, V. J., Ackermann, T., Pfetzer, N., Sumpton, D., Mackay, G., Kalna, G., Nixon, C., Blyth, K., Gottlieb, E. & Tardito, S. Improving the metabolic fidelity of cancer models with a physiological cell culture medium. *Science Advances* **5** (2019).

19. Wakil, S. J. & Abu-Elheiga, L. A. Fatty acid metabolism: Target for metabolic syndrome. *Journal of Lipid Research* **50,** S138–S143 (2009).

20. Inoue, K., Zhuang, L., Maddox, D. M., Smith, S. B. & Ganapathy, V. Structure, function, and expression pattern of a novel sodium-coupled citrate transporter (NaCT) cloned from mammalian brain. *Journal of Biological Chemistry* **277,** 39469–39476 (2002).

21. Pajor, A. M. Molecular cloning and functional expression of a sodium-dicarboxylate cotransporter from human kidney. *American Journal of Physiology-Renal Physiology* **270,** F642–F648 (1996).

22. Birkenfeld, A. L., Lee, H. Y., Guebre-Egziabher, F., Alves, T. C., Jurczak, M. J., Jornayvaz, F. R., Zhang, D., Hsiao, J. J., Martin-Montalvo, A., Fischer-Rosinsky, A., Spranger, J., Pfeiffer, A. F., Jordan, J., Fromm, M. F., König, J., Lieske, S., Carmean, C. M., Frederick, D. W., Weismann, D., Knauf, F., Irusta, P. M., De Cabo, R., Helfand, S. L., Samuel, V. T. & Shulman, G. I. Deletion of the mammalian INDY homolog mimics aspects of dietary restriction and protects against adiposity and insulin resistance in mice. *Cell Metabolism* **14,** 184–195 (2011).

23. Huard, K., Brown, J., Jones, J. C., Cabral, S., Futatsugi, K., Gorgoglione, M., Lanba, A., Vera, N. B., Zhu, Y., Yan, Q., Zhou, Y., Vernochet, C., Riccardi, K., Wolford, A., Pirman, D.,

Niosi, M., Aspnes, G., Herr, M., Genung, N. E., Magee, V. T., Uccello, D. P., Loria, P., Di, L., Gosset, J. R., Hepworth, D., Rolph, T., Pfefferkorn, J. A. & Erion, D. M. Discovery and characterization of novel inhibitors of the sodium-coupled citrate transporter (NaCT or SLC13A5). *Scientific Reports* **5,** 1–13 (2015).

24. Von Loeffelholz, C., Lieske, S., Neuschäfer-Rube, F., Willmes, D. M., Raschzok, N., Sauer, I. M., König, J., Fromm, M. F., Horn, P., Chatzigeorgiou, A., Pathe-Neuschäfer-Rube, A., Jordan, J., Pfeiffer, A. F., Mingrone, G., Bornstein, S. R., Stroehle, P., Harms, C., Wunderlich, F. T., Helfand, S. L., Bernier, M., de Cabo, R., Shulman, G. I., Chavakis, T., Püschel, G. P. & Birkenfeld, A. L. The human longevity gene homolog INDY and interleukin-6 interact in hepatic lipid metabolism. *Hepatology* **66,** 616–630 (2017).

25. Hardies, K., Kovel, D. C. G. F., Weckhuysen, S., Asselbergh, B., Geuens, T., Deconinck, T., Azmi, A., May, P., Brilstra, E., Becker, F., Barisic, N., Craiu, D., Braun, K. P. J., Lal, D., Thiele, H., Schubert, J., Weber, Y. & Slot, V. R. Recessive mutations in SLC13A5 result in a loss of citrate transport and cause neonatal epilepsy, developmental delay and teeth hypoplasia. *Brain* **138,** 3238–3250 (2015).

26. Klotz, J., Porter, B. E., Colas, C., Schlessinger, A. & Pajor, A. M. Mutations in the Na+/citrate cotransporter NaCT (SLC13A5) in pediatric patients with epilepsy and developmental delay. *Molecular Medicine* **22,** 310–321 (2016).

27. Matricardi, S., De Liso, P., Freri, E., Costa, P., Castellotti, B., Magri, S., Gellera, C., Granata, T., Musante, L., Lesca, G., Oertel, J., Craiu, D., Hammer, T. B., Møller, R. S., Barisic, N., Abou Jamra, R., Polster, T., Vigevano, F. & Marini, C. Neonatal developmental and epileptic encephalopathy due to autosomal recessive variants in SLC13A5 gene. *Epilepsia* **61,** 2474–2485 (2020).

28. Schossig, A., Bloch-Zupan, A., Lussi, A., Wolf, N. I., Raskin, S., Cohen, M., Giuliano, F., Jurgens, J., Krabichler, B., Koolen, D. A., Sobreira, N. L. d. M., Maurer, E., Muller-Bolla, M., Penzien, J., Zschocke, J. & Kapferer-Seebacher, I. SLC13A5 is the second gene associated with Kohlschütter-Tönz syndrome. *Journal of Medical Genetics* **54,** 54–62 (2017).

29. Thevenon, J., Milh, M., Feillet, F., St-Onge, J., Duffourd, Y., Jugé, C., Roubertie, A., Héron, D., Mignot, C., Raffo, E., Isidor, B., Wahlen, S., Sanlaville, D., Villeneuve, N., Darmency-Stamboul, V., Toutain, A., Lefebvre, M., Chouchane, M., Huet, F., Lafon, A., De Saint Martin, A., Lesca, G., El Chehadeh, S., Thauvin-Robinet, C., Masurel-Paulet, A., Odent, S., Villard, L., Philippe, C., Faivre, L. & Rivière, J. B. Mutations in SLC13A5 cause autosomal-recessive epileptic encephalopathy with seizure onset in the first days of Life. *American Journal of Human Genetics* **95,** 113–120 (2014).

30. Fahy, E., Subramaniam, S., Murphy, R., Nishijima, M., Raetz, C., Shimizu, T., Spener, F., Meer, G., Wakelam, M. & Dennis, E. Update of the LIPID MAPS comprehensive classification system for lipids. *The Journal of Lipid Research* **50,** S9–S14 (2009).

31. Shevchenko, A. & Simons, K. Lipidomics: Coming to grips with lipid diversity. *Nature Reviews Molecular Cell Biology* **11,** 593–598 (2010).

32. Harayama, T. & Riezman, H. Understanding the diversity of membrane lipid composition. *Nat Rev Mol Cell Bio* **19,** 281 (2018).

33. Jackson, C. L., Walch, L. & Verbavatz, J. M. Lipids and Their Trafficking: An Integral Part of Cellular Organization. *Developmental Cell* **39,** 139–153 (2016).

34. Hannun, Y. A. & Obeid, L. M. Sphingolipids and their metabolism in physiology and disease. *Nature Reviews Molecular Cell Biology* **19,** 175–191 (2018).

35. Lee, C. H., Olson, P. & Evans, R. M. Minireview: Lipid metabolism, metabolic diseases, and peroxisome proliferator-activated receptors. *Endocrinology* **144,** 2201–2207 (2003).

36. Iwamoto, H., Abe, M., Yang, Y., Cui, D., Seki, T., Nakamura, M., Hosaka, K., Lim, S., Wu, J., He, X., Sun, X., Lu, Y., Zhou, Q., Shi, W., Torimura, T., Nie, G., Li, Q. & Cao, Y. Cancer Lipid Metabolism Confers Antiangiogenic Drug Resistance. *Cell metabolism* **28,** 104–117.e5 (July 2018).

37. Kamphorst, J. J., Chung, M. K., Fan, J. & Rabinowitz, J. D. Quantitative analysis of acetyl-CoA production in hypoxic cancer cells reveals substantial contribution from acetate. *Cancer & Metabolism* **2,** 23 (2014).

38. Rustan, A. C. & Drevon, C. A. Fatty Acids: Structures and Properties. *Encyclopedia of Life Sciences* (2005).

39. Menendez, J. A. & Lupu, R. Fatty acid synthase and the lipogenic phenotype in cancer pathogenesis. *Nature Reviews Cancer* **7** (2007).

40. Cai, Y., Crowther, J., Pastor, T., Dehairs, J., Swinnen, V. J. & Sablina, A. A. Loss of Chromosome 8p Governs Tumor Progression and Drug Response by Altering Lipid Metabolism Article Loss of Chromosome 8p Governs Tumor Progression and Drug Response by Altering Lipid Metabolism. *Cancer Cell* **29,** 751–766 (2016).

41. Knobloch, M., Braun, S. M. G., Zurkirchen, L., Schoultz, V. C., Zamboni, N., Arauzo-bravo, M. J., Kovacs, W. J., Karalay, Ö., Machado, R. A. C., Roccio, M., Lutolf, M. P., Semenkovich, C. F. & Jessberger, S. Metabolic control of adult neural stem cell activity by Fasn-dependent lipogenesis. *Nature* **493,** 226–230 (2014).

42. Schug, Z. T., Peck, B., Jones, D. T., Zhang, Q., Grosskurth, S., Alam, I. S., Goodwin, L. M., Smethurst, E., Mason, S., Blyth, K., McGarry, L., James, D., Shanks, E., Kalna, G., Saunders, R. E., Jiang, M., Howell, M., Lassailly, F., Thin, M. Z., Spencer-Dene, B., Stamp, G., van den Broek, N. J., Mackay, G., Bulusu, V., Kamphorst, J. J., Tardito, S., Strachan, D., Harris, A. L., Aboagye, E. O., Critchlow, S. E., Wakelam, M. J., Schulze, A. & Gottlieb, E. Acetyl-CoA synthetase 2 promotes acetate utilization and maintains cancer cell growth under metabolic stress. *Cancer Cell* **27,** 57–71 (2015).

43. Guillou, H., Zadravec, D., Martin, P. G. & Jacobsson, A. The key roles of elongases and desaturases in mammalian fatty acid metabolism: Insights from transgenic mice. *Progress in Lipid Research* **49,** 186–199 (2010).

44. Loftus, T. M., Jaworsky, D. E., Frehywot, G. L., Townsend, C. A., Ronnett, V. G., Lane, M. D. & Kuhajda, F. P. Reduced Food Intake and Body Weight in Mice Treated with Fatty Acid Synthase Inhibitors. *Science* **288,** 2379–2382 (2000).

45. Menendez, J. A., Vellon, L., Mehmi, I., Oza, B. P., Ropero, S., Colomer, R. & Lupu, R. Inhibition of fatty acid synthase (FAS) suppresses HER2/neu (erbB-2) oncogene overexpression in cancer cells. *Proceedings of the National Academy of Sciences* **101,** 10715–10720 (2004).

46. Pizer, E. S., Thupari, J., Han, W. F., Pinn, M. L., Chrest, F. J., Frehywot, G. L., Townsend, C. A. & Kuhajda, F. P. Malonyl-Coenzyme-A Is a Potential Mediator of Cytotoxicity Induced by Fatty-Acid Synthase Inhibition in Human Breast Cancer Cells and Xenografts 1. *Cancer Research* **60,** 213–218 (2000).

47. Svensson, R. U., Parker, S. J., Eichner, L. J., Kolar, M. J., Wallace, M., Brun, S. N., Lombardo, P. S., Van Nostrand, J. L., Hutchins, A., Vera, L., Gerken, L., Greenwood, J., Bhat, S., Harriman, G., Westlin, W. F., Harwood, H. J., Saghatelian, A., Kapeller, R., Metallo, C. M. & Shaw, R. J. Inhibition of acetyl-CoA carboxylase suppresses fatty acid synthesis and tumor growth of non-small-cell lung cancer in preclinical models. *Nature Medicine* **22** (2016).

48. Kim, C. W., Addy, C., Kusunoki, J., Anderson, N. N., Deja, S., Fu, X., Burgess, S. C., Li, C., Chakravarthy, M., Previs, S., Milstein, S., Fitzgerald, K., Kelley, D. E. & Horton, J. D. Acetyl CoA Carboxylase Inhibition Reduces Hepatic Steatosis but Elevates Plasma Triglycerides in Mice and Humans: A Bedside to Bench Investigation. *Cell Metabolism* **26,** 394–406.e6 (2017).

49. Ference, B. A., Neff, D., Cabot, M., Catapano, A. & Ray, K. Genetic Target Validation for ATP-Citrate Lyase Inhibition. *Journal of the American College of Cardiology* **69,** 1655 (2017).

50. Beckner, M. E., Fellows-Mayle, W., Zhang, Z., Agostino, N. R., Kant, J. A., Day, B. W. & Pollack, I. F. Identification of ATP Citrate Lyase as a Positive Regulator of Glycolytic Function in Glioblastomas. *International Journal of Cancer* **126,** 2282–2295 (2011).

51. Migita, T., Narita, T., Nomura, K., Miyagi, E., Inazuka, F., Matsuura, M., Ushijima, M., Mashima, T., Seimiya, H., Satoh, Y., Okumura, S., Nakagawa, K. & Ishikawa, Y. ATP Citrate Lyase : Activation and Therapeutic Implications in Non – Small Cell Lung Cancer. *Cancer Research* **68,** 8547–8555 (2008).

52. Pope, E. D., Kimbrough, E. O., Vemireddy, L. P., Surapaneni, P. K., Copland, J. A. & Mody, K. Aberrant lipid metabolism as a therapeutic target in liver cancer. *Expert Opinion on Therapeutic Targets* **23,** 473–483 (2019).

53. Turyn, J., Schlichtholz, B., Dettlaff-Pokora, A., Presler, M., Goyke, E., Matuszewski, M., Kmieć, Z., Krajka, K. & Swierczynski, J. Increased Activity of Glycerol 3-phosphate Dehydrogenase and Other Lipogenic Enzymes in Human Bladder Cancer. *Hormone and Metabolic Research* **35,** 565–569 (2003).

54. Varis, A., Wolf, M., Monni, O., Vakkari, M.-l., Kokkola, A., Moskaluk, C., Frierson, H., Powell, S. M., Knuutila, S., Kallioniemi, A. & El-rifai, W. Targets of Gene Amplification and Overexpression at 17q in Gastric Cancer 1. *Cancer Research* **62,** 2625–2629 (2002).

55. Yancy, H. F., Mason, J. A., Peters, S., Iii, C. E. T., Littleton, G. K., Jett, M. & Day, A. A. Metastatic progression and gene expression between breast cancer cell lines from African American and Caucasian women. *Journal of Carcinogenesis* **6** (2007).

56. Zhou, Y., Bollu, L. R., Tozzi, F., Ye, X., Bhattacharya, R., Gao, G., Dupre, E., Xia, L., Lu, J., Fan, F., Bellister, S., Ellis, L. M. & Weihua, Z. ATP citrate lyase mediates resistance of colorectal cancer cells to SN38. *Molecular Cancer Therapeutics* **12,** 2782–2791 (2013).

57. Comerford, S. A., Huang, Z., Du, X., Wang, Y., Cai, L., Witkiewicz, A. K., Walters, H., Tantawy, M. N., Fu, A., Manning, H. C., Horton, J. D., Hammer, R. E., Mcknight, S. L. & Tu, B. P. Acetate dependence of tumors. *Cell* **159,** 1591–1602 (2014).

58. Xu, M., Nagati, J. S., Xie, J., Li, J., Walters, H., Moon, Y.-a., Gerard, R. D., Huang, C.-l., Comerford, S. A., Hammer, R. E., Horton, J. D., Chen, R. & Garcia, J. A. An acetate switch regulates stress erythropoiesis. *Nature Medicine* **20** (2014).

59. Lee, V. J., Carrer, A., Shah, S., Snyder, N. W., Wei, S., Venneti, S., Worth, A. J., Yuan, Z. F., Lim, H. W., Liu, S., Jackson, E., Aiello, N. M., Haas, N. B., Rebbeck, T. R., Judkins, A., Won, K. J., Chodosh, L. A., Garcia, B. A., Stanger, B. Z., Feldman, M. D., Blair, I. A. & Wellen, K. E. Akt-dependent metabolic reprogramming regulates tumor cell Histone acetylation. *Cell Metabolism* **20,** 306–319 (2014).

60. Shi, L. & Tu, B. P. Acetyl-CoA and the regulation of metabolism: mechanisms and consequences. *Current Opinion in Cell Biology* **33,** 125–131 (2015).

61. Sivanand, S., Rhoades, S., Jiang, Q., Lee, V. J., Benci, J., Zhang, J., Yuan, S., Viney, I., Zhao, S., Carrer, A., Bennett, M. J., Minn, A. J., Weljie, A. M., Greenberg, R. A. & Wellen, K. E. Nuclear Acetyl-CoA Production by ACLY Promotes Homologous Recombination. *Molecular Cell* **67,** 252–265.e6 (2017).

62. Wellen, K. E., Hatzivassiliou, G., Sachdeva, U. M., Bui, V. T., Cross, J. R. & Thompson, C. B. ATP-Citrate Lyase Links Cellular Metabolism to Histone Acetylation. *Science* **324,** 1076–1080 (2009).

63. Pinkosky, S. L., Newton, R. S., Day, E. A., Ford, R. J., Lhotak, S., Austin, R. C., Birch, C. M., Smith, B. K., Filippov, S., Groot, P. H. E., Steinberg, G. R. & Lalwani, N. D. Liver-specific ATP-citrate lyase inhibition by bempedoic acid decreases LDL-C and attenuates atherosclerosis (2016).

64. Ray, K. K., Bays, H. E., Catapano, A. L., Lalwani, N. D., Bloedon, L. T., Sterling, L. R., Robinson, P. L., Ballantyne, C. M. & Trial, C. H. Safety and Efficacy of Bempedoic Acid to Reduce LDL Cholesterol. *New England Journal of Medicine* **380,** 1022–1032 (2019).

65. He, A., Chen, X., Tan, M., Chen, Y., Lu, D., Zhang, X., Dean, J. M., Razani, B. & Lodhi, I. J. Acetyl-CoA Derived from Hepatic Peroxisomal β-Oxidation Inhibits Autophagy and Promotes Steatosis via mTORC1 Activation. *Molecular Cell* **79,** 30–42.e4 (2020).

66. Zha, S., Ferdinandusse, S., Hicks, J., Denis, S., Dunn, T., Wanders, R., Luo, J., Marzo, A. & Isaacs, W. Peroxisomal branched chain fatty acid beta-oxidation pathway is upregulated in prostate cancer. *Prostate* **63,** 316–23 (2005).

67. Gowda, G. A. N. & Djukovic, D. in *Mass Spectrometry in Metabolomics: Methods and Protocols* (ed Raftery, D.) 3–12 (Springer New York, New York, NY, 2014). https://doi.org/10.1007/978-1-4939-1258-2_1.

68. Sauer, U. Metabolic networks in motion: 13C-based flux analysis. *Molecular systems biology* **2,** 62 (2006).

69. Wiechert, W. 13C Metabolic Flux Analysis. *Metab Eng* **3,** 195–206 (2001).

70. Cordes, T. & Metallo, C. M. in *High-Throughput Metabolomics: Methods and Protocols* (ed D'Alessandro, A.) 219–241 (Springer New York, New York, NY, 2019).

71. Fendt, S. M., Bell, E. L., Keibler, M. A., Olenchock, B. A., Mayers, J. R., Wasylenko, T. M., Vokes, N. I., Guarente, L., Vander Heiden, M. G. & Stephanopoulos, G. Reductive glutamine metabolism is a function of the -ketoglutarate to citrate ratio in cells. *Nat Commun* **4,** 2236 (2013).

72. Locasale, J. W., Grassian, A. R., Melman, T., Lyssiotis, C. A., Mattaini, K. R., Bass, A. J., Heffron, G., Metallo, C. M., Muranen, T., Sharfi, H., Sasaki, A. T., Anastasiou, D., Mullarky, E., Vokes, N. I., Sasaki, M., Beroukhim, R., Stephanopoulos, G., Ligon, A. H., Meyerson, M., Richardson, A. L., Chin, L., Wagner, G., Asara, J. M., Brugge, J. S., Cantley, L. C. & Heiden, V. M. G. Phosphoglycerate dehydrogenase diverts glycolytic flux and contributes to oncogenesis. *Nature Publishing Group* **43** (2011).

73. Mayers, J. R., Torrence, M. E., Danai, L. V., Papagiannakopoulos, T., Davidson, S. M., Bauer, M. R., Lau, A. N., Ji, B. W., Dixit, P. D., Hosios, A. M., Muir, A., Chin, C. R., Freinkman, E., Jacks, T., Wolpin, B. M., Vitkup, D. & Vander Heiden, M. G. Tissue of origin dictates branched-chain amino acid metabolism in mutant Kras-driven cancers. *Science* **353,** 1161–5 (2016).

74. Wallace, M., Green, C., Roberts, L., Lee, Y., Justin, M., Joan, S., Meurs, N., Gengatharan, J., Hover, J., Phillips, S., Ciaraldi, T., Guertin, D., Cabrales, P., Ayres, J., Nomura, D., Loomba, R. & Metallo, C. Enzyme promiscuity drives branched-chain fatty acid synthesis in adipose tissues. *Nat Chem Biol* **14,** 1021 (2018).

75. Badur, M. G., Muthusamy, T., Parker, S. J., Ma, S., Mcbrayer, K., Cordes, T., Magana, J. H., Guan, K.-l. & Christian, M. Oncogenic R132 IDH1 Mutations Limit NADPH for De Novo Lipogenesis through (D)2-Hydroxyglutarate Production in Fibrosarcoma Cells. *Cell Reports* **25,** 1018–1026 (2018).

76. Fan, J., Ye, J., Kamphorst, J. J., Shlomi, T., Thompson, C. B. & Rabinowitz, J. D. Quantitative flux analysis reveals folate-dependent. *Nature* **510,** 298–302 (2014).

77. Lewis, C. A., Parker, S. J., Fiske, B. P., Mccloskey, D., Gui, D. Y., Green, C. R., Vokes, N. I., Feist, A. M., Heiden, V. M. G. & Metallo, C. M. Tracing Compartmentalized NADPH Metabolism in the Cytosol and Mitochondria of Mammalian Cells. *Molecular Cell* **55,** 1–11 (2014).

78. Antoniewicz, M. R., Kelleher, J. K. & Stephanopoulos, G. Elementary metabolite units (EMU): a novel framework for modeling isotopic distributions. *Metab. Eng.* **9,** 68–86 (2007).

79. Young, J. D. INCA: a computational platform for isotopically non-stationary metabolic flux analysis. *Bioinformatics* (2014).

80. Kelleher, J. K. & Nickol, G. B. *Isotopomer Spectral Analysis : Utilizing Nonlinear Models in Isotopic Flux Studies* 1st ed. (Elsevier Inc., 2015).

81. Kelleher, J. K. & Masterson, T. M. Model equations for condensation biosynthesis using stable isotopes and radioisotopes. *American Journal of Physiology-Endocrinology and Metabolism* **262,** E118–E125 (1992).

82. Kharroubi, A., Masterson, T., Aldaghlas, T., Kennedy, K. & Kelleher, J. Isotopomer spectral analysis of triglyceride fatty acid synthesis in 3T3-L1 cells. *Am. J. Physiol.* **263,** E667–75 (1992).

83. King, Z. A., Dräger, A., Ebrahim, A., Sonnenschein, N., Lewis, N. E. & Palsson, B. O. Escher: A Web Application for Building, Sharing, and Embedding Data-Rich Visualizations of Biological Pathways. *PLoS Computational Biology* **11,** 1–13 (2015).

Chapter 2

NaCT/SLC13A5 facilitates citrate import and metabolism under nutrient-limited conditions

2.1 Abstract

Citrate lies at a critical node of metabolism, linking tricarboxylic acid metabolism and lipogenesis via acetyl-coenzyme A. Recent studies have observed that deficiency of the sodium citrate transporter (NaCT), encoded by *SLC13A5*, dysregulates hepatic metabolism and drives pediatric epilepsy. To examine how NaCT contributes to citrate metabolism in cells relevant to the pathophysiology of these diseases, we apply 13C isotope tracing to *SLC13A5*-deficient hepatocellular carcinoma (HCC) cells and primary rat cortical neurons. Exogenous citrate appreciably contributes to intermediary metabolism only under hypoxic conditions. In the absence of glutamine, citrate supplementation increases *de novo* lipogenesis and growth of HCC cells. Knockout of *SLC13A5* in Huh7 cells compromises citrate uptake and catabolism. Citrate supplementation rescues Huh7 cell viability in response to glutamine deprivation or Zn^{2+}

treatment, and NaCT-deficiency mitigates these effects. Collectively, these findings demonstrate that NaCT-mediated citrate uptake is metabolically important under nutrient-limited conditions and may facilitate resistance to metal toxicity.

2.2 Introduction

Citrate serves as a critical substrate for biosynthesis, acetylation, and the regeneration of NAD(P)H. Within mitochondria, citrate is synthesized by citrate synthase and metabolized in the tricarboxylic acid (TCA) cycle to support bioenergetics. Citrate is also exported to the cytosol via the mitochondrial citrate transporter (SLC25A1/CTP) and metabolized by ATP-citrate lyase (ACLY) to generate acetyl-coenzyme A (AcCoA) for downstream metabolic processes, including lipid biosynthesis and acetylation [1]. Although mitochondrial production of citrate is the primary source for most cells, plasma concentrations are relatively high [2]. In addition, dysregulation of plasma citrate homeostasis has pathophysiological consequences including impaired blood clotting and bone disorders [2, 3]. The functional importance of exogenous citrate transport by cells has therefore garnered increasing interest [2, 4, 5].

A plasma membrane specific variant of *SLC25A1*, pmCIC, allows for import and catabolism of extracellular citrate in prostate cancer cells [6]. Further, several members of the SLC13 sodium sulfate/carboxylate symporter gene family are capable of importing citrate into cells in a sodium-coupled mechanism [7, 8]. Both *SLC13A2*, primarily expressed in the kidney and small intestine, and *SLC13A3*, widely expressed across tissues, are capable of importing citrate, although with significantly lower affinity compared to dicarboxylic TCA intermediates [7, 8]. Liver and brain tissue express the sodium-dependent citrate transporter (NaCT; also known as mINDY) encoded by *SLC13A5*, which preferentially transports citrate across the plasma membrane [9, 10].

SLC13A5 function has been linked to hepatic glucose and fatty acid metabolism, and development of NaCT inhibitors has garnered therapeutic interest [11, 12]. Deletion of *Slc13a5*

is protective against high-fat diet-induced insulin resistance and attenuates hepatic gluconeogenesis and lipogenesis [13]. Further, pharmacological inhibition of NaCT reduced hepatic lipid accumulation in mice fed a high-fat diet [11]. Additionally, hepatic *SLC13A5* expression correlated positively with both body and liver fat in a cohort of non-alcoholic fatty liver disease (NAFLD) patients [14]. Functional impacts of NaCT inhibition or knockdown have been proposed in cells, though findings are not necessarily dependent on the presence of extracellular citrate [15–17]. Citrate transport may also influence AcCoA metabolism and ionic homeostasis in the nervous system, as loss-of-function mutations in *SLC13A5* have been linked to pediatric epilepsy, Kohlschütter-Tönz syndrome, and other brain disorders [18–22]. Notably, citrate levels were significantly increased in plasma and cerebrospinal fluid (CSF) in such epilepsy patients [23]. Mice deficient in this transporter accumulated citrate in CSF while plasma abundances were not affected; moreover, *Slc13a5*$^{-/-}$ mice exhibited an increased propensity for seizures as well as impaired neuronal function [24]. While citrate's role in chelating metal cations has been hypothesized to drive this pathophysiology [4, 25], the mechanism(s) through which *SLC13A5*-deficiency drives pathogenesis in mammalian cells warrants further study.

Here, we have applied mass spectrometry and metabolic flux approaches to genetically engineered HCC cell lines and primary cortical neurons to decipher the impact of extracellular citrate import on metabolism and cell viability. *SLC13A5* was expressed in both cell types, and exogenous citrate was imported and metabolized to fatty acids and TCA cycle intermediates. However, citrate only contributed appreciably to these pathways under hypoxic conditions where pyruvate dehydrogenase (PDH) flux is reduced. Under these conditions, citrate was predominantly catabolized in the cytosol to support AcCoA generation. We also used CRISPR/Cas9 to generate *SLC13A5*-deficient HCC cell lines, which lacked the ability to transport and metabolize exogenous citrate. In addition, we observed that *SLC13A5* expression was required to increase the growth of hypoxic HCC cells under glutamine-deprived conditions. Finally, NaCT function was also necessary to allow for citrate-mediated protection against Zn^{2+} toxicity. Collectively, our study

highlights the biological roles of NaCT and citrate metabolism in mammalian cells, emphasizing the importance of metabolic stress in observing significant phenotypes.

2.3 Materials and Methods

2.3.1 Human Samples

Plasma samples from healthy fasted adults (29-42 years, 5 male, 3 female) were obtained from a clinical cohort recruited from Tompkins County, New York area as described previously [26]. Participants were excluded if they had a history of negative or allergic reactions to local anesthetic, used immunosuppressive medications, were prescribed anti-coagulation therapy, were pregnant, had a musculoskeletal disorder, suffered from alcoholism (>11 drinks per week for women and >14 drinks per week for men) or other drug addictions or were acutely ill at the time of participation [27, 28]. The Cornell University Institutional Review Board approved the protocol and all the subjects provided written informed consent in accordance with the Declaration of Helsinki.

2.3.2 Cell Lines

HepG2, Huh7, A549, MCF7, and 143B cells were obtained from ATCC and were incubated at 37C with 5% CO_2 and cultured using Dulbecco's Modified Eagle Media (DMEM) with 10% Fetal Bovine Serum and 1% Penicillin-Streptomycin. Cells tested negative for mycoplasma contamination. For hypoxia experiments, cells were maintained in a humidified glove box (Coy) at 5% CO_2 and either 1% O_2 (cancer cell lines) or 3% O_2 (primary cortical neurons). Primary cortical neurons and astrocytes were isolated and cultured in Neurobasal medium (neuron) or DMEM medium supplemented with 10 mM glucose, 0 mM glutamine, and 10% FBS (astrocytes) as described in detail by Cordes et al. 2020 [29]. All media were adjusted to pH = 7.3.

2.3.3 Cell Proliferation and ^{13}C Tracing

Proliferation studies were performed on 12 well plates with an initial cell number of 50,000/well for Huh7s and 100,000/well for HepG2s. Cells were plated in growth media and allowed to adhere for 24 hours before changing to the specified growth media. Cell counts were performed at days 0 and 4 using a hemocytometer.

For Zn^{2+} tolerance studies, cells were plated at 50,000/well and allowed to adhere for 24 hours. They were then placed in the hypoxia chamber for 24 hours before swapping to $\pm$ 5 mM citrate media. After changing media, cells were allowed to acclimate for 24 hours before 300 μM ZnCl2 in water was spiked into the designated wells. Cells were counted 24 hours after Zn^{2+} treatment using a hemocytometer.

13C isotope tracing media was formulated using glucose and glutamine free DMEM 5030 supplemented with either 20 mM [U-$^{13}C_6$]glucose, 4 mM [U-$^{13}C_5$]glutamine, or 500 μM [2,4-$^{13}C_2$]citrate (Cambridge Isotopes) and 10% dialyzed FBS. All studies were performed with a final concentration of 20 mM glucose and 4 mM glutamine. Cultured cells were washed with 1 mL PBS prior to applying tracing media for 24-72 hours as indicated in figure legends. For tracing experiments performed in hypoxia, cancer cells were acclimated to the hypoxia chamber in basal media for 24 hours prior to applying pre-hypoxified tracing media. Mole percent enrichment (MPE) of isotopes were calculated as the percent of all atoms within the metabolite pool that are labeled, using Escher-Trace [30]:

$$\frac{\sum_{i=0}^{n} i * M_{\mathrm{i}}}{n}$$

Where n is the number of carbon atoms in the metabolite and M_i is the relative abundance of the ith mass isotopomer. The MPE of [2,4-$^{13}C_2$]citrate is 33%, while MPE for [U-$^{13}C_6$]glucose and [U-$^{13}C_5$]glutamine is 100%.

2.3.4 Isotopomer Spectral Analysis (ISA)

Isotopomer spectral analysis (ISA) was performed to estimate the percent of newly synthesized palmitate as well as the contribution of a tracer of interest to the lipogenic acetyl-CoA pool [31, 32]. Parameters for contribution of 13C tracers to lipogenic acetyl-CoA (D value) and percentage of newly synthesized fatty acid (g(t) value) and their 95% confidence intervals are then calculated using a best-fit model from INCA MFA software. Experimental fatty acid labeling from [U-$^{13}C_6$]glucose, [U-$^{13}C_5$]glutamine, or [2,4-$^{13}C_2$]citrate after 48 hour trace was compared to simulated labeling using a reaction network where C16:0 is condensation of 8 AcCoA. ISA data plotted as mean $\pm$ 95% CI. $*$ indicates statistical significance by non-overlapping confidence intervals.

2.3.5 CRISPR/Cas9 engineered knockout cell lines

SLC13A5 knockout clones were generated using the strategy described previously [33]. Briefly, a guide RNA (gRNA) was designed to target the human *SLC13A5* gene using the CRISPOR webtool (gRNA sequence: AGGCACAATGAATAGCAGGG) [34]. The gRNA duplex was cloned into lentiCRISPRv2 (Addgene #52961) [35]. HepG2 and Huh7 cells were transfected with the *SLC13A5* specific gRNA to generate pooled knockouts. After puromycin selection, single-cell clones were isolated by diluting the pooled knockout lines at 1 cell/100 μL and plating 100 μL into each well of a 96 well plate. Clones were maintained by exchanging media every 3-5 days. HepG2 clones were cultured in 50% conditioned media to enhance proliferation at early stages of cloning. Conditioned media was generated by collecting the spent media that had been culturing HepG2s after 2 days, spinning down at 300g for 5 min, and filtering using a 0.2 micron filter to clear cellular debris. This media was diluted 1:1 with DMEM with 10% FBS 1% penstrep to generate the 50% conditioned media. Clones were validated via Sanger sequencing. Sequences were aligned using the NCBI BLASTN suite [36].

2.3.6 Lentivirus Production

One 10cm dish of HEK293FT cells at 60% confluency were transfected with 1.3 μg VSV.G/pMD2.G, 5.3 μg lenti-gag/pol/pCMVR8.2, and 4 μg of the gRNA duplexed lenti-CRISPRv2 using 16 μL Lipofectamine 3000 diluted in 0.66 mL of OPTI-MEM. Medium containing viral particles was harvested 48 and 72 hours after transfection, then concentrated by Centricon Plus-20 100,000 NMWL centrifugal ultrafilters, divided into aliquots and frozen at -80°C.

2.3.7 Determination of Extracellular Fluxes

Metabolic fluxes for citrate were calculated by collecting media at time 0 and spent media after 48 hours. Spent media was centrifuged at 300g for 5 min, to remove cell debris. Cell counts were performed at time 0 and after 48 hours as well. To calculate citrate uptake fluxes, citrate was quantified by GC-MS via standard curve. To calculate glucose, lactate, glutamine, and glutamate uptake fluxes media metabolites were quantified using a Yellow Springs Instruments (YSI) Biochemistry Analyzer 2950.

2.3.8 Metabolite Extraction and GC-MS Analysis

At the conclusion of the tracer experiment, media was aspirated. Then, cells were rinsed twice with 0.9% saline solution and lysed with 250 μL ice-cold methanol. After 1 minute, 100 μL water containing 1 μg/ml norvaline was added to each sample and vortexed for one minute. 250 μL chloroform was added to each sample, and all were vortexed again for 1 minute. After centrifugation at 21,130 g for 10 minutes at 4°C, 250 μL of the upper aqueous layer was collected and evaporated under vacuum at 4°C. The lower organic layer was evaporated under air at room temperature.

Plasma metabolites were extracted and quantified as follows. For metabolite extraction,

10 μL of each plasma sample was utilized. First, 90 μL of a 9:1 methanol:water mix was added to each sample and the samples were vortexed for 1 minute. After centrifugation at 16,000g for 10 minutes, 90 μL of supernatant was collected, evaporated under vacuum at -4°C and analyzed using GC/MS. Metabolite levels of TCA intermediates were quantified using external standard curves.

Dried polar and nonpolar metabolites were processed for gas chromatography (GC) mass spectrometry (MS) as described previously in Cordes and Metallo [31]. Briefly, polar metabolites were derivatized using a Gerstel MultiPurpose Sampler (MPS 2XL). Methoxime-tBDMS derivatives were formed by addition of 15 μL 2% (w/v) methoxylamine hydrochloride (MP Biomedicals, Solon, OH) in pyridine and incubated at 45°C for 60 minutes. Samples were then silylated by addition of 15 μL of N-tert-butyldimethylsily-N-methyltrifluoroacetamide (MTBSTFA) with 1% tert-butyldimethylchlorosilane (tBDMS) (Regis Technologies, Morton Grove, IL) and incubated at 45°C for 30 minutes. Nonpolar metabolites were saponified and transesterified to fatty acid methyl esters (FAMEs) by adding 500 μL of 2% H2SO4 in methanol to the dried nonpolar layer and heating at 50°C for 1 hour. FAMEs were then extracted by adding 100 μL of a saturated salt solution and 500 μL hexane and vortexing for 1 minute. The hexane layer was removed, evaporated, and resuspended with 60μL hexane for injection.

Derivatized polar samples were injected into a GC-MS using a DB-35MSUI column (30m x 0.25mm i.d. x 0.25μm, Agilent J&W Scientific, Santa Clara, CA) installed in an Agilent 7890B GC system integrated with an Agilent 5977a MS. Samples were injected at a GC oven temperature of 100°C which was held for 1 minute before ramping to 255°C at 3.5°C/min then to 320°C at 15°C/min and held for 3 minutes. Electron impact ionization was performed with the MS scanning over the range of 100-650 m/z for polar metabolites.

Derivatized nonpolar samples were injected into a GC-MS using a Fame Select column (100m x 0.25mm i.d. x 0.25μm, Agilent J&W Scientific, Santa Clara, CA) installed in an Agilent 7890A GC system integrated with an Agilent 5977A MS. Samples were injected at a GC oven

temperature of 80°C which was held for 1 minute before ramping to 170°C at 20°C/min then to 188°C at 1°C/min then to 250°C at 20°C/min and held for 10 minutes. Electron impact ionization was performed with the MS scanning over the range of 54-400 m/z for nonpolar metabolites. Metabolite levels and mass isotopomer distributions were analyzed with an in-house Matlab script which integrated the metabolite fragment ions and corrected for natural isotope abundances.

2.3.9 ^{13}C Metabolic Flux Analysis

^{13}C Metabolic Flux Analysis (MFA) was performed using INCA [32]. The model was comprised of the chemical reactions and atom transitions of central carbon metabolism, as well as extracellular fluxes of glucose, lactate, glutamine, glutamate, and citrate and the isotopic labeling distributions of intracellular metabolites from Huh7 cells traced with DMEM and 500μM citrate containing [U-$^{13}C_6$]glucose, [U-$^{13}C_5$]glutamine, or [2,4-$^{13}C_2$]citrate under hypoxia. The 13C MFA was performed with the following assumptions:

1. Cellular metabolism and isotopic labeling were assumed to be at steady state.
2. Cells were assumed to grow exponentially.
3. Labeled CO2 formed from decarboxylation reactions is dilute and assumed to never reincorporate in carboxylation reactions.
4. Separate mitochondrial and cytosolic pools of aspartate, oxaloacetate, malate, fumarate, α-KG, citrate, glutamate, pyruvate, and acetyl-CoA were modeled with exchange fluxes for malate, aspartate, glutamate, α-KG, and citrate.
5. The gross, per cell biomass requirements of proliferating Huh7 hepatoma cells were similar to those reported previously for mammalian cells [37].

Additional information regarding the estimated fluxes generated by the model, as well as the data incorporated into the model can be found in the supplementary material (Table S2, S3, Document S3).

2.3.10 RNA isolation and quantitative RT-PCR

Total RNA was purified from cultured cells using Trizol Reagent (Life Technologies) per manufacturer's instructions. First-strand cDNA was synthesized from 1 μg of total RNA using iScript Reverse Transcription Supermix for RT-PCR (Bio-Rad Laboratories) according to the manufacturer's instructions. Individual 20 μl SYBR Green real-time PCR reactions consisted of 1 μl of diluted cDNA, 10 μl of SYBR Green Supermix (Bio-Rad), and 1 μl of each 5 μM forward and reverse primers. For standardization of quantification, 18S was amplified simultaneously. The PCR was carried out on 96-well plates on a CFX Connect Real time System (Bio-Rad), using a three-stage program provided by the manufacturer: 95 °C for 3 min, 40 cycles of 95 °C for 10 s and 60 °C for 30 s. Gene-specific primers are tabulated in Table S1.

2.3.11 ^{14}C citrate uptake assay

Uptake of ^{14}C citrate was quantified as described previously [38]. Briefly, cells were seeded at 3 x 105 cells/well on 6 well collagen treated plates. After 24 hours, cells were acclimated to serum free media for 24 hours. To carry out the assay, each well was washed twice with choline buffer (mM: 140 Choline, 2 KCl, 1 MgCl2, 1 CaCl2, 10 HEPES, pH adjusted to 7.4 with 1M Tris), then incubated with 1 ml sodium buffer (mM: 140 NaCl, 2 KCl, 1 MgCl2, 1 CaCl2, 10 HEPES, pH adjusted to 7.4 with 1M Tris) or choline buffer containing 100 μM [^{14}C]-citrate for 30 minutes at 37oC with rocking. The uptake assays were stopped, and the cells were washed four times with 2.5 ml choline buffer. Cells were dissolved in 0.4 ml/well 1% SDS, transferred to scintillation vials with Econoscint Scintillation cocktail and then the radioactivity in the plates was counted using a scintillation counter.

2.3.12 Quantification and Statistical Analysis

Statistical analyses were performed using Graphpad PRISM software. Unless indicated, all results shown as mean ± SD of cellular triplicates obtained from one representative experiment as specified in each figure legend. P values were calculated using a Student's two-tailed t test, One-way ANOVA w/ Dunnet's method for multiple comparisons, or Two-way ANOVA w/ Tukey's method for multiple comparisons; *, P value < 0.05; **, P value < 0.01; ***, P value < 0.001, ****, P value < 0.0001. Unless indicated, all normalization and statistical tests compared to NTC cells, normoxia, or (-)citrate conditions.

2.4 Results

2.4.1 Extracellular citrate uptake is tissue-specific

Recent findings have highlighted the importance of circulating TCA intermediates as metabolic substrates or regulators of tissue function [39]. We quantified levels of TCA intermediates in human plasma and observed that the concentration of citrate was 108 ± 23 μM while other TCA cycle intermediates were 10-fold less abundant (all < 10 μM) (Fig. 1A). Although citrate is not present in typical culture media such as DMEM, RPMI, or OptiMEM, we found that complete medium including 10% FBS contained 16 ± 5 μM citrate, significantly lower than that observed in human plasma (Fig. 1B).

To identify cell types that might readily consume extracellular citrate, we first used a publicly available transcriptomics dataset from the Genotype-Tissue Expression (GTEx) project and compared *SLC13A5* expression across 32 human tissues [40]. *SLC13A5* transcripts were highest in liver, brain, reproductive tissues, and salivary gland (Fig. 1C). Next, we quantified the expression of *SLC13A5* in a panel of cells of different tissue origin. Consistent with published data [40], we found that the HCC cell lines HepG2 and Huh7 as well as primary cortical neurons

express detectable *SLC13A5* mRNA while little was detected in other cell lines (Figs. 1D, E). We next cultured cells in DMEM supplemented with 500 μM extracellular citrate for 48 hours and quantified uptake flux. Only the HCC cell lines exhibited net uptake of citrate, which correlated with *SLC13A5* transcription (Fig. 1F).

2.4.2 Citrate dilutes central carbon metabolism in HCC cells and neurons in hypoxia

The above results indicate that HCC cells import exogenous citrate. To quantify the contribution of citrate to central carbon metabolism in more detail, we cultured HepG2 and Huh7 cells in medium containing uniformly ^{13}C labeled ([U-$^{13}C_5$]) glutamine and quantified metabolite abundance and isotope enrichment (Fig. 2A). Studies were performed under normoxic (21% oxygen) or hypoxic (1% oxygen) conditions for 48 hours, as hypoxia is known to potently reduce citrate abundances due to decreased PDH flux [41–43]. Indeed, TCA intermediate abundances were significantly decreased in hypoxia, with citrate being the most decreased of those measured (Fig. S1A). As expected, labeling from [U-$^{13}C_5$]glutamine indicated that cells increased the contribution of reductive carboxylation to synthesis of aspartate and fatty acids, as well as glutamine anaplerosis under hypoxia (Figs. S1B-D). To indirectly determine whether exogenous citrate was metabolized in cells we cultured Huh7 and HepG2 cells with and without 500 μM unlabeled (^{12}C) citrate in medium containing [U-$^{13}C_5$]glutamine or [U-$^{13}C_6$]glucose, respectively. Citrate addition resulted in a dilution of glutamine's contribution to TCA cycle anaplerosis (Figs. 2B, S1E) and *de novo* lipogenesis through reductive carboxylation in HCC cell lines (Figs. 2C, D). We performed similar studies using primary rat cortical neurons, although [U-$^{13}C_6$]glucose was used given the higher enrichment obtained in differentiated neurons (Divakaruni et al., 2017). Although labeling of the intracellular citrate pool was significantly diluted, glucose-derived TCA labeling was not impacted (Fig. 2E). On the other hand, we observed a significant impact on the contribution of glucose to lipogenic AcCoA using ISA modeling (Fig. 2F). Our findings suggest

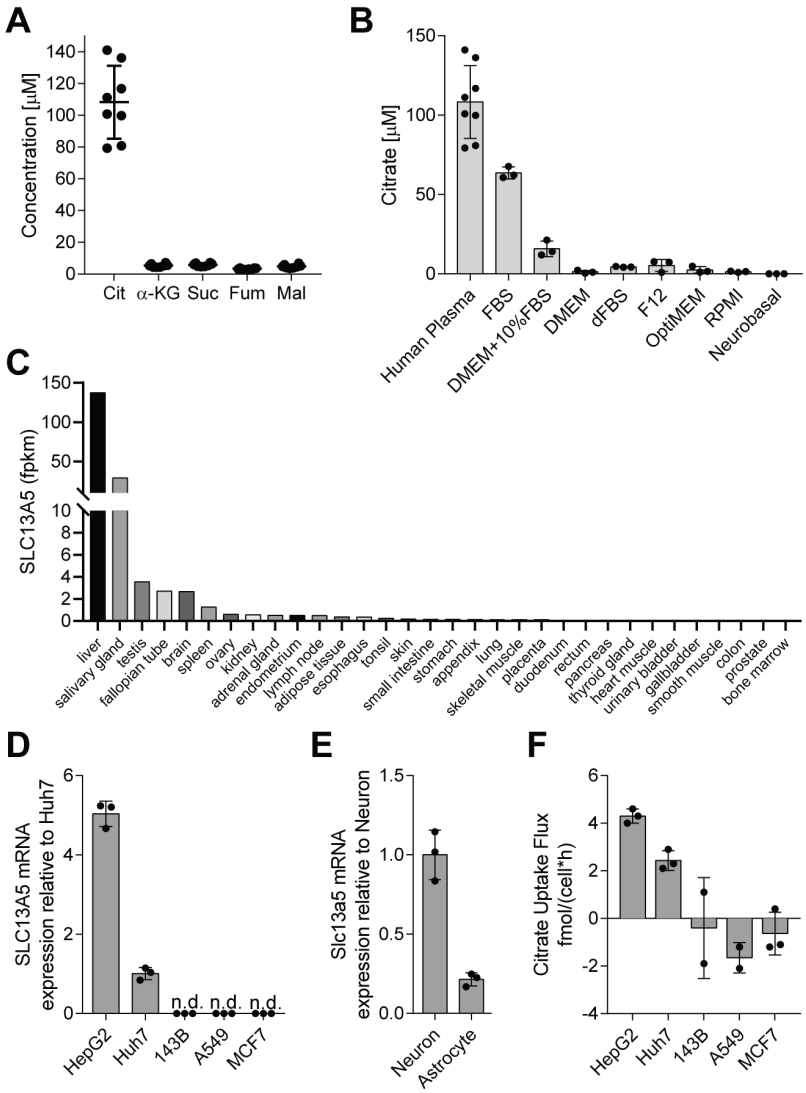

Figure 2.1: **Extracellular citrate uptake is tissue-specific.** A) Plasma concentration of TCA intermediates in humans (n=8). B) Citrate concentration in cell culture medias (n=3), human plasma (n=8) same as in panel 1A.C) *SLC13A5* mRNA expression in human tissues, from GTEx [40].D) *SLC13A5* mRNA expression in cancer cells grown in normoxia relative to Huh7s (n=3). E) *Slc13a5* mRNA expression in primary rat neuron and astrocyte cells in normoxia relative to neurons (n=3). F) Net citrate uptake flux in cancer cell lines over 48 hours (n=3). Cit, citrate; α-KG, α-ketoglutarate; Suc, succinate; Fum, fumarate; Mal, malate. All data are presented as means$\pm$SD. All data are representative of three sample replicates.

that extracellular citrate metabolically contributes as an anaplerotic and/or lipogenic substrate in low oxygen conditions, and further highlight the need for some metabolic stress to observe a significant contribution.

To more directly quantify how extracellular citrate is metabolized in *SLC13A5*-expressing cells, we cultured the above cell types in growth medium supplemented with 500 μM [2,4-$^{13}C_2$]citrate. Cells were rinsed 2X in NaCl prior to extraction to ensure accurate analysis of intracellular pools. In HepG2 and Huh7 cells, extracellular citrate contributed significantly to TCA labeling, with 4% enrichment of citrate and 1% enrichment of downstream intermediates in normoxic cells (Fig. 3A). Under hypoxia, enrichment of intracellular citrate and other TCA intermediates was significantly elevated (Fig. 3A). In Huh7 cells, net uptake of extracellular citrate was significantly lower than that of glucose or glutamine in both normoxia and hypoxia (Fig. S2A). However, though citrate uptake was not significantly increased in hypoxia, the ratio of net citrate uptake to anaplerotic glutamine usage (glutamine uptake versus glutamate efflux) flux was increased in hypoxia (3.0) compared to normoxia (1.3) (Fig. S2B), reflecting the increased dependence on exogenous citrate driven by reduced PDH flux in hypoxia. Intracellular citrate was also highly enriched by [2,4-$^{13}C_2$]citrate in neonatal rat cortical neurons, though detectable labeling was only observed on α-ketoglutarate (Fig. 3B). Furthermore, no changes in enrichment were observed when comparing normoxic to 3% oxygen. These differences are likely due to the reduced anaplerotic/biosynthetic needs of post-mitotic neurons. Our results confirm that extracellular citrate is transported into these *SLC13A5*-expressing cell types. Importantly, we were unable to detect significant isotope enrichment on TCA intermediates in other cell types tested that lack *SLC13A5* expression, suggesting this transporter is important for citrate import and metabolism (Fig. S2C).

Next, we examined whether extracellular citrate was metabolized to AcCoA by quantifying enrichment of fatty acids in cells cultured with the isotope tracers noted above. We detected significant enrichment of palmitate and stearate from [2,4-$^{13}C_2$]citrate, demonstrating that HCC

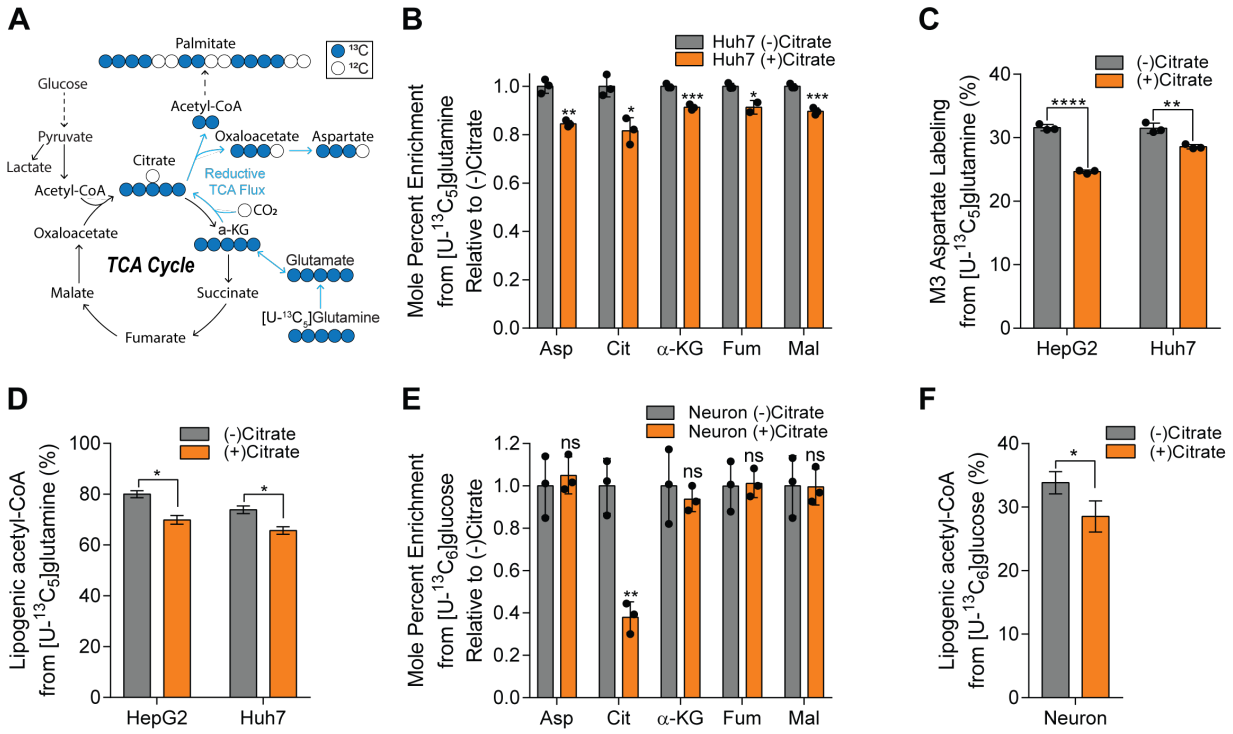

Figure 2.2: **Citrate dilutes central carbon pathway labeling in hepatocellular carcinoma and neuronal cells in hypoxia.** A) Atom transition map depicting catabolism of [U-$^{13}C_5$]glutamine. Closed circles indicate ^{13}C carbon, open circles indicate ^{12}C carbon. B) Mole percent enrichment of TCA intermediates from [U-$^{13}C_5$]glutamine in Huh7 cells grown in hypoxia $\pm$ 500 μM citrate for 48 hours, relative to (-) citrate (n=3). C) Percent labeling of M3 aspartate from [U-$^{13}C_5$]glutamine in HepG2 and Huh7 cells grown in hypoxia $\pm$ 500 μM citrate for 48 hours (n=3). D) Percent of lipogenic acetyl-CoA contributed by [U-$^{13}C_5$]glutamine in HepG2 and Huh7 cells grown in hypoxia $\pm$ 500 μM citrate for 48 hours (n=3).E) Mole percent enrichment of TCA intermediates from [U-$^{13}C_6$]glucose in primary rat neuron cells grown in 3% oxygen $\pm$ 500 μM citrate for 48 hours, relative to (-) citrate (n=3). F) Percent of lipogenic acetyl-CoA contributed by [U-$^{13}C_6$]glucose in primary rat neuron cells grown in 3% oxygen $\pm$ 500 μM citrate for 48 hours (n=3). Asp, aspartate; Cit, citrate; α-KG, α-ketoglutarate; Fum, fumarate; Mal, malate. In (B,C,E) data are plotted as mean $\pm$ SD. Statistical significance is relative to (-) citrate as determined by two-sided Student's t-test with *, P value < 0.05; **, P value < 0.01; ***, P value < 0.001, ****, P value < 0.0001. In (D,F) data are plotted as mean $\pm$ 95% confidence interval (CI). Statistical significance by non-overlapping confidence intervals, *. Unless indicated, all data represent biological triplicates. Data shown are from one of at least two separate experiments. See also Figure S1.

cell lines and neurons generate AcCoA from exogenous citrate (Figs. 3C, D). No enrichment of palmitate was observed in other cell types that lack *SLC13A5* expression (Fig. S2D). We then compared the relative contributions of [U-$^{13}C_6$]glucose, [U-$^{13}C_5$]glutamine, and [2,4-$^{13}C_2$]citrate to the lipogenic AcCoA fueling palmitate synthesis under hypoxia (Fig. 3E). As expected, glutamine is the primary source of lipogenic carbon under these conditions. However, when citrate was present in the medium, HCC cells actively metabolized this substrate and the contribution of exogenous citrate to palmitate was greater than that of glucose, though glutamine remained the major lipogenic substrate in these hypoxic conditions. Notably, addition of extracellular citrate did not alter the rate of *de novo* lipogenesis (Fig. S2E). Thus, exogenous citrate is taken up by *SLC13A5* expressing cell types and is metabolized to fuel TCA cycle metabolism and lipogenesis, thereby diluting the corresponding glutamine contribution in low oxygen conditions. These findings are reminiscent of the usage of acetate under hypoxia in cells expressing ACSS2 [44].

2.4.3 Extracellular citrate is primarily catabolized in the cytosol

The [2,4-$^{13}C_2$]citrate tracer enables more detailed insights into the compartment specific catabolism of extracellular citrate when considering isotopologue distributions in more detail. In hypoxic, proliferating cancer cells, TCA intermediates are predominantly obtained from glutaminolysis (M4 labeling from [U-$^{13}C_5$]glutamine) or reductive carboxylation (M3 labeling from [U-$^{13}C_5$]glutamine), with TCA (re)cycling contributing to a lesser degree [41, 45]. Therefore, TCA substrates in such cells are mostly present for one pass of the cycle. When [2,4-$^{13}C_2$]citrate is catabolized directly in the cytosol by ATP-citrate lyase (ACLY), M1 acetyl-CoA and M1 oxaloacetate are formed which further yielded M1 TCA intermediates via malate-aspartate shuttling and malic enzyme activity (Fig. 4A). Alternatively, if citrate is imported into the mitochondria directly by SLC25A1, as has been shown to occur in anchorage-independent cultures [46, 47], [2,4-$^{13}C_2$]citrate will generate M2 isotopologues of TCA intermediates (Fig.

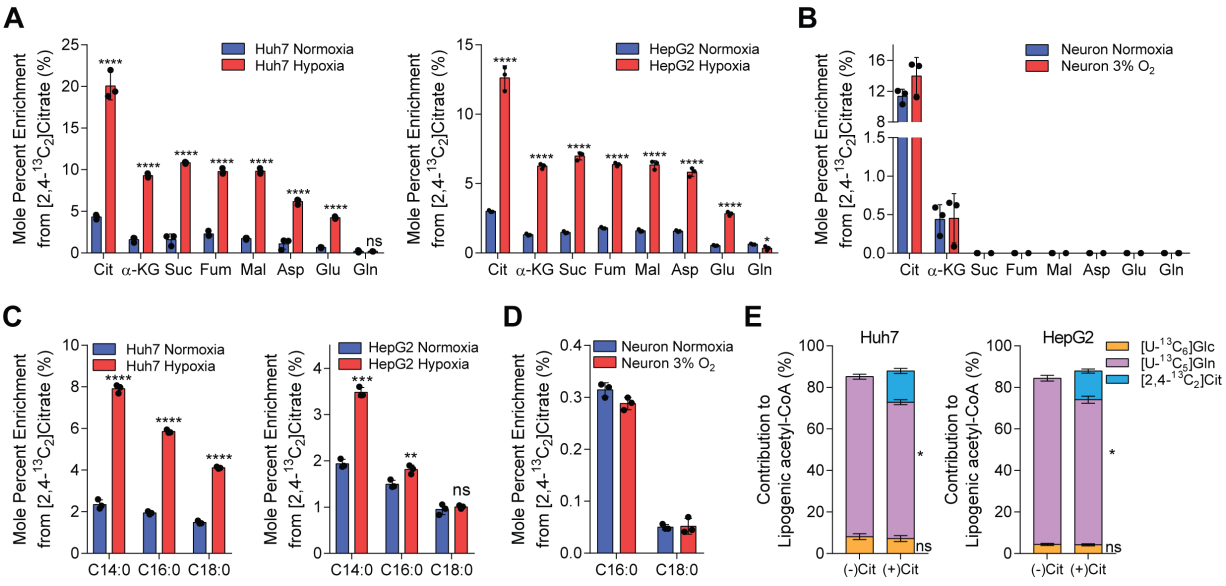

Figure 2.3: **Exogenous citrate is metabolized for TCA anaplerosis and fatty acid synthesis.** A) Mole percent enrichment of TCA intermediates from [2,4-$^{13}C_2$]citrate in Huh7 (left) and HepG2 (right) cells grown in normoxia or hypoxia for 48 hours (n=3). B) Mole percent enrichment of TCA intermediates from [2,4-$^{13}C_2$]citrate in primary rat neuron cells grown in normoxia or 3% oxygen for 48 hours (n=3). C) Mole percent enrichment of fatty acids from [2,4-$^{13}C_2$]citrate in Huh7 (left) and HepG2 (right) cells grown in normoxia or hypoxia for 48 hours (n=3). D) Mole percent enrichment of fatty acids from [2,4-$^{13}C_2$]citrate in primary rat neuron cells grown in normoxia or 3% oxygen for 48 hours (n=3). E) Percent of lipogenic acetyl-CoA contributed by [U-$^{13}C_6$]glucose, [U-$^{13}C_5$]glutamine and [2,4-$^{13}C_2$]citrate, in the presence or absence of 500 μM unlabeled citrate in Huh7 (left) and HepG2 (right) cells grown in hypoxia for 48 hours (n=3). Cit, citrate; α-KG, α-ketoglutarate; Suc, succinate; Fum, fumarate; Mal, malate; Asp, aspartate; Glu, glutamate; Gln, glutamine; Glc, glucose. In (A-D) data are plotted as mean $\pm$ SD. Statistical significance is relative to normoxia as determined by two-sided Student's t-test with *, P value < 0.05; **, P value < 0.01; ***, P value < 0.001, ****, P value < 0.0001. Unless indicated, all data represent biological triplicates. In (E) data are plotted as mean $\pm$ 95% confidence interval (CI). Statistical significance by non-overlapping confidence intervals, *. Data shown are from one of at least two separate experiments. See also Figure S2.

4B). When culturing HCC cell lines in the presence of 500 μM [2,4-$^{13}C_2$]citrate for 48 hours in either normoxia or hypoxia, we found that the M1 isotopologue of aspartate, malate and fumarate was more abundant than the M2 isotopologue, and the ratio of M1/M2 labeling increased for these metabolites in hypoxic conditions (Fig. 4C). On the other hand, relative abundance of M2 α-ketoglutarate was similar to or greater than M1 labeling, which indicates that a high exchange flux exists for the cytosolic aconitase (ACO1) and isocitrate dehydrogenase (IDH1) reactions (Figs. 4A, D). To resolve these intracellular fluxes in a more unbiased manner which allows for multiple turns of the TCA cycle, we generated a ^{13}C MFA model encompassing glycolysis, compartmentalized TCA and amino acid metabolism, pyruvate cycling, *de novo* lipogenesis, and citrate import/exchange (Supplementary Document S3) using the INCA software suite [32]. This model incorporated steady state labeling of Huh7 cells grown in hypoxia with citrate across three independent experiments using either [U-$^{13}C_6$]glucose, [U-$^{13}C_5$]glutamine, or [2,4-$^{13}C_2$]citrate. We also included direct flux measurements of glucose, lactate, glutamine, glutamate, and citrate uptake and/or secretion. The model output confirmed that extracellular citrate (cit.x) contributes appreciably to lipogenesis and TCA metabolism and is significantly catabolized in the cytosol by ACLY and ACO1/IDH1 (Fig. 4E). Importantly, the model estimated that reductive carboxylation exchange flux occurs primarily in the mitochondrial matrix via IDH2/ACO2 under these citrate-replete conditions, although cytosolic exchange cannot be entirely ruled out from this model (Tables S2 and S3). Glutamine to fatty acid flux was reconciled by high rates of pyruvate cycling and malic enzyme flux, consistent with the maintained activity of glutaminolysis that occurs in hypoxia [45, 48]. Collectively, these results suggest that exogenous citrate is primarily metabolized in the cytosol by ACLY and ACO1/IDH1 and predominantly enters TCA metabolism via α-ketoglutarate under the conditions tested (Figs. 4C, D).

Figure 2.4: **Extracellular citrate is primarily catabolized in the cytosol.** A) Schematic of extracellular [2,4-$^{13}C_2$]citrate catabolism in the cytosol. Closed circles indicate ^{13}C carbon, open circles indicate ^{12}C carbon. B) Schematic of extracellular [2,4-$^{13}C_2$]citrate catabolism in the mitochondria. Closed circles indicate ^{13}C carbon, open circles indicate ^{12}C carbon. C) Ratio of the relative abundance of M1/M2 TCA intermediates from 500 μM [2,4-$^{13}C_2$]citrate in Huh7 (left) and HepG2 (right) cells grown in normoxia or hypoxia for 48 hours (n=3). D) Mass isotopomer distribution of α-KG from 500 μM [2,4-$^{13}C_2$]citrate in Huh7 (left) and HepG2 (right) cells grown in hypoxia for 48 hours (n=3). E) Schematic of central carbon metabolism with net fluxes and selected confidence intervals estimated by 13C MFA for Huh7 cells grown in DMEM with 500 μM citrate in hypoxia for 48 hours. Net flux values are listed adjacent to reaction arrows, with 95% confidence intervals in square brackets. Dashed arrows represent grouped reactions. Some net or exchange fluxes for compartmentalized, parallel reactions were not resolvable. Cit, citrate; Oac, oxaloacetate; Fum, fumarate; Mal, malate; Asp, aspartate; α-KG, α-ketoglutarate; Glc, glucose; Gln, glutamine; Glu, glutamate; Lac, lactate; GAP, glyceraldehyde 3-phosphate; Palm, palmitate; FAO, fatty acid oxidation. In all graphs data are plotted as mean $\pm$ SD. Statistical significance is relative to normoxia as determined by two-sided Student's t-test with *, P value < 0.05; **, P value < 0.01; ***, P value < 0.001, ****, P value < 0.0001. Unless indicated, all data represent biological triplicates. Data shown are from one of at least two separate experiments.

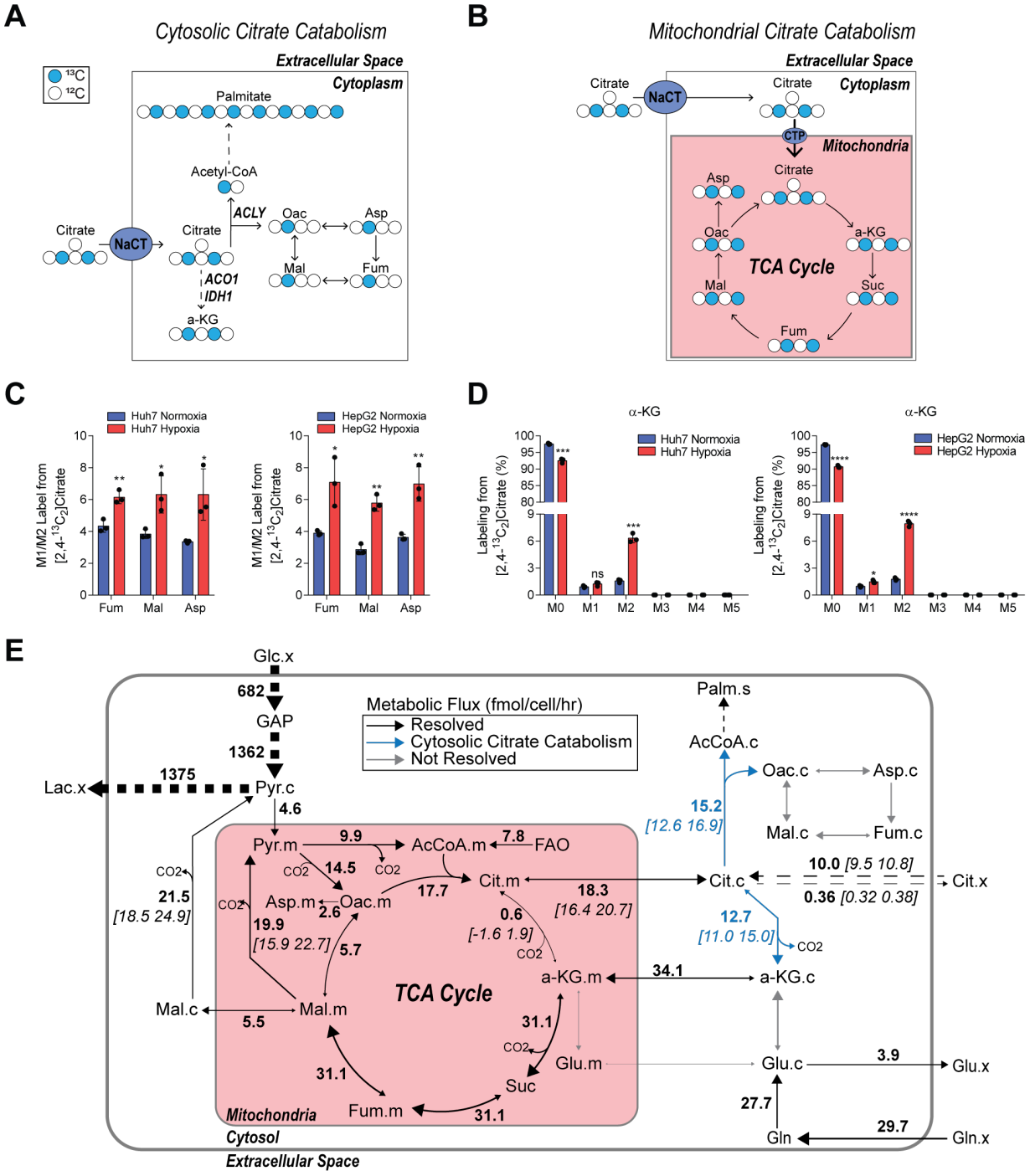
A
Cytosolic Citrate Catabolism
Extracellular Space
Cytoplasm
Palmitate
Acetyl-CoA
ACLY
Citrate
NaCT
Oac
Asp
Mal
Fum
ACO1
IDH1
a-KG
B
Mitochondrial Citrate Catabolism
Extracellular Space
Cytoplasm
Mitochondria
CTP
TCA Cycle
C
Huh7 Normoxia
Huh7 Hypoxia
HepG2 Normoxia
HepG2 Hypoxia
M1/M2 Label from [2,4-13C2]Citrate
Fum
Mal
Asp
D
α-KG
Labeling from [2,4-13C2]Citrate (%)
M0
M1
M2
M3
M4
M5
E
Glc.x
682
GAP
1362
1375
Lac.x
Pyr.c
4.6
Metabolic Flux (fmol/cell/hr)
Resolved
Cytosolic Citrate Catabolism
Not Resolved
Palm.s
AcCoA.c
Oac.c
Asp.c
15.2
[12.6 16.9]
Mal.c
Fum.c
Pyr.m
9.9
AcCoA.m
7.8
FAO
14.5
CO2
Cit.m
17.7
18.3
[16.4 20.7]
Cit.c
10.0 [9.5 10.8]
Cit.x
0.36 [0.32 0.38]
21.5
[18.5 24.9]
Asp.m
2.6
Oac.m
19.9
[15.9 22.7]
5.7
0.6
[-1.6 1.9]
12.7
[11.0 15.0]
a-KG.m
34.1
a-KG.c
Mal.m
5.5
TCA Cycle
31.1
Glu.m
Glu.c
3.9
Glu.x
Suc
Fum.m
31.1
27.7
Gln
29.7
Gln.x
Mitochondria
Cytosol
Extracellular Space

2.4.4 NaCT supports extracellular citrate import and metabolism in hepatocellular carcinoma cells

To directly interrogate the function of NaCT with respect to citrate metabolism, we engineered *SLC13A5*-deficient knockout (KO) HepG2 and Huh7 cells using CRISPR/Cas9 and compared their metabolic phenotype to cells expressing a non-targeting control (NTC) sgRNA. Two clones were tested for each KO cell line. *SLC13A5* KO clones were validated by sequencing the region of interest (Fig. S3). In both cell lines, knockout of *SLC13A5* resulted in reduced citrate uptake flux when the cells were cultured in growth medium supplemented with 500 μM exogenous citrate (Figs. 5A, S4A), suggesting these cells lacked NaCT activity. To further verify the functional impact of NaCT-deficiency we quantified citrate transport using [1,5-^{14}C]citrate [49]. Sodium induced citrate uptake was significantly reduced in the *SLC13A5* KO cells (Fig. 5B). Notably, NaCT-deficiency induced no significant metabolic phenotype in cells grown in the absence of extracellular citrate, as fatty acid synthesis rates were unchanged and alterations to metabolite abundances were either moderate or inconsistent in the knockout clones. (Figs. S4B, C). Additionally, although previous studies have found that *SLC13A5* knockdown alone induced a reduction in the expression of fatty acid synthesis gene expression in hepatocellular carcinoma cells [15], we observed no impact on ACLY expression in HepG2 or Huh7 *SLC13A5* KO cells (Fig. S4D). These data indicate that the citrate transporter induces a metabolic change that is selective to citrate uptake.

To elucidate how impaired NaCT activity influences citrate catabolism, we cultured each cell line for 48 hours in the presence of 500 μM [2,4-$^{13}C_2$]citrate under hypoxic conditions. Huh7 *SLC13A5* KO cells had no measurable enrichment from [2,4-$^{13}C_2$]citrate on TCA cycle intermediates or fatty acids (Figs. 5C, D). A reduction in enrichment was also observed with HepG2 *SLC13A5* KO cells (Fig. S4E, F). Our data confirms that NaCT is the primary importer of extracellular citrate in the tested HCC cell lines. Next, we cultured NaCT-deficient cells

in the presence or absence of exogenous ^{12}C citrate in [U-$^{13}C_5$]glutamine tracer medium and quantified enrichment on TCA cycle intermediates and fatty acids compared to control cells. When unlabeled citrate was present in the media, we only observed dilution of [U-$^{13}C_5$]glutamine on TCA cycle intermediates in *SLC13A5*-expressing cells (Figs. 5E, S4G). Furthermore, we observed no dilution in isotopologues downstream of reductive carboxylation (i.e. M3 aspartate) or glutamine-derived lipogenic acetyl-CoA with extracellular unlabeled citrate addition in the Huh7 *SLC13A5* KO cells (Figs. 5F, G). Thus, our results indicate that NaCT is required for the import and metabolism of extracellular citrate, in HCC cells.

2.4.5 NaCT facilitates growth under nutrient stress and resistance to zinc toxicity

Next we hypothesized that citrate import and catabolism could fulfill certain metabolic roles of glutamine, which serves as a key substrate for anaplerosis and acetyl-CoA synthesis under hypoxia. We cultured the above HCC cell lines in glutamine-deficient media containing [U-$^{13}C_6$]glucose supplemented with exogenous citrate. Notably, addition of citrate in the absence of glutamine significantly increased fatty acid synthesis in control cells (Fig. 6A). Furthermore, citrate supplementation generally decreased enrichment of TCA intermediates and associated amino acids from [U-$^{13}C_6$]glucose but increased the abundance of α-ketoglutarate in NTC cells (Fig. 6B, S5A), no change was observed in NaCT-deficient cell lines. Next, we cultured *SLC13A5* expressing Huh7 cells with [2,4-$^{13}C_2$]citrate and found that in the absence of glutamine, enrichment from ^{13}C citrate on metabolites associated with glutamine synthesis increased significantly (Fig. 6C). These data indicate that NaCT facilitates citrate-mediated anaplerosis under nutrient-limited conditions.

Since glutamine is critical for numerous biological processes, including anaplerosis and lipogenesis, we next tested whether NaCT-mediated citrate uptake impacted cell proliferation upon glutamine deprivation. We observed that exogenous citrate addition increased the growth

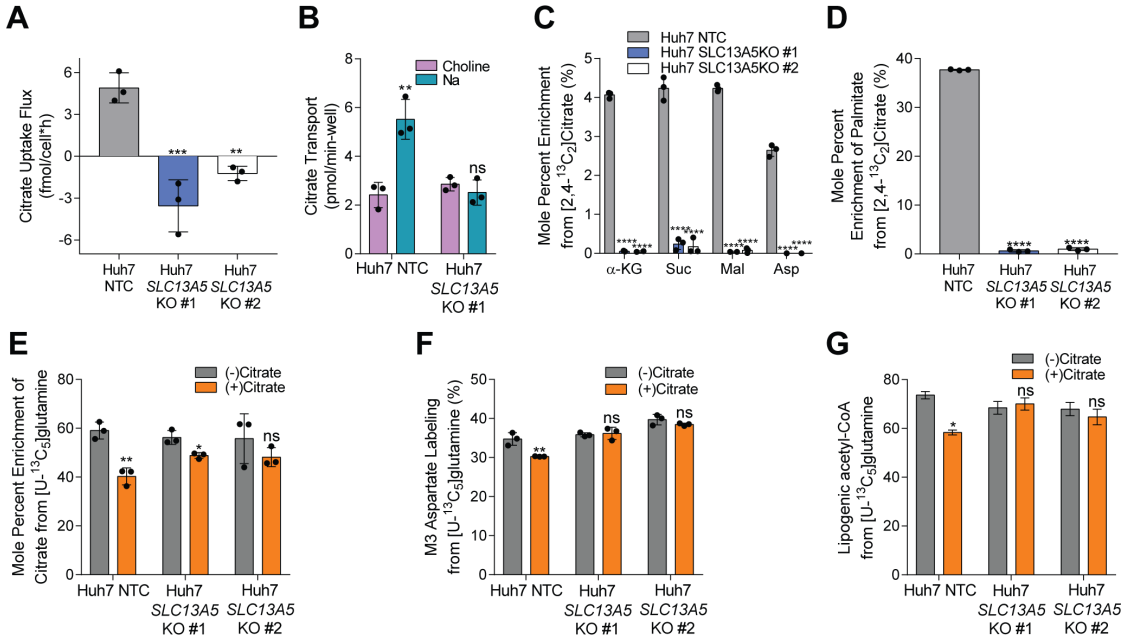

Figure 2.5: **NaCT supports extracellular citrate import and metabolism in hepatocellular carcinoma cells.** A) Citrate uptake flux in Huh7 NTC and *SLC13A5*-KO cells grown in hypoxia for 48 hours (n=3). B) Citrate transport in Huh7 NTC and *SLC13A5*-KO #1 cells (n=3). C) Mole percent enrichment of TCA intermediates from [2,4-$^{13}C_2$]citrate in Huh7 NTC and *SLC13A5*-KO cells grown in hypoxia for 48 hours (n=3). D) Mole percent enrichment of palmitate from [2,4-$^{13}C_2$]citrate in Huh7 NTC and *SLC13A5*-KO cells grown in hypoxia for 48 hours (n=3). E) Mole percent enrichment of citrate from [U-$^{13}C_5$]glutamine in Huh7 NTC and *SLC13A5*-KO cells $\pm$ 500 μM citrate grown in hypoxia for 48 hours (n=3).F) Percent labeling of M3 aspartate from [U-$^{13}C_5$]glutamine in Huh7 NTC and *SLC13A5*-KO cells $\pm$ 500 μM citrate grown in hypoxia for 48 hours (n=3). G) Percent of lipogenic acetyl-CoA contributed by [U-$^{13}C_5$]glutamine in Huh7 NTC and *SLC13A5*-KO cells $\pm$ 500 μM citrate grown in hypoxia for 48 hours (n=3). α-KG, α-ketoglutarate; Suc, succinate; Mal, malate; Asp, aspartate. In all graphs data are plotted as mean $\pm$ SD. Statistical significance is relative to NTC as determined by One-way ANOVA w/ Dunnet's method for multiple comparisons (A,C,D) or relative to (-) citrate as determined by two-sided Student's t-test (B,E,F) with *, P value < 0.05; **, P value < 0.01; ***, P value < 0.001, ****, P value < 0.0001. In (G) data are plotted as mean $\pm$ 95% confidence interval (CI). Statistical significance by non-overlapping confidence intervals, *. Unless indicated, all data represent biological triplicates. See also Figure S3 and S4. (C-G) Data shown are from one of at least two separate experiments.

rate of the Huh7 NTC cells by 80% in glutamine depleted media under hypoxic conditions (Fig. 6D). Notably, no growth alteration was observed with citrate addition in glutamine rich media (Fig. 6D) or normoxia (Fig. S5B). Importantly, citrate supplementation did not increase proliferation of NaCT-deficient cell lines (Figs. 6D, S5B). This data indicates that NaCT-mediated citrate transport supports metabolism under nutrient-limited conditions. We next tested whether NaCT-mediated citrate transport influences resistance to metal toxicity against ions such as zinc (Zn^{2+}). Regions of the brain including the hippocampus and cerebral cortex are Zn^{2+} enriched [50]. Under pathological conditions including epilepsy, ischemia, and traumatic brain injury, cerebral Zn^{2+} levels increase and may cause neuronal cell death [50–52]. Intracellular citrate has been suggested to be a protective chelator against Zn^{2+} in rat cortical neurons [53]; however, the role of NaCT in this process remains unclear. Given the established link between pediatric epilepsy and *SLC13A5* mutations, we hypothesized that NaCT-mediated citrate uptake could generally facilitate protection against Zn^{2+} toxicity. Hepatocytes can also exhibit sensitivity to Zn^{2+} [54, 55], so we employed the Huh7 NaCT-deficient cells described above to determine if NaCT function mediates protection against Zn^{2+} toxicity. We cultured hypoxic Huh7 NTC and NaCT-deficient cells in the presence or absence of citrate and ZnCl2 for 24 hours and quantified cell viability. While citrate supplementation protected Huh7 NTC against Zn^{2+} toxicity, cell lines lacking NaCT showed reduced viability (Fig 6E). Thus, our data highlights that extracellular citrate import via NaCT facilitates protection against nutrient deprivation as well as Zn^{2+} toxicity in human cells (Fig. 6F).

2.5 Discussion

Cells take up diverse nutrients from the extracellular microenvironment, and each metabolite may serve a distinct purpose or function. Nutrient transport is selective and regulated, in part, through cell-specific expression of transporters such as NaCT, which is restricted to liver and

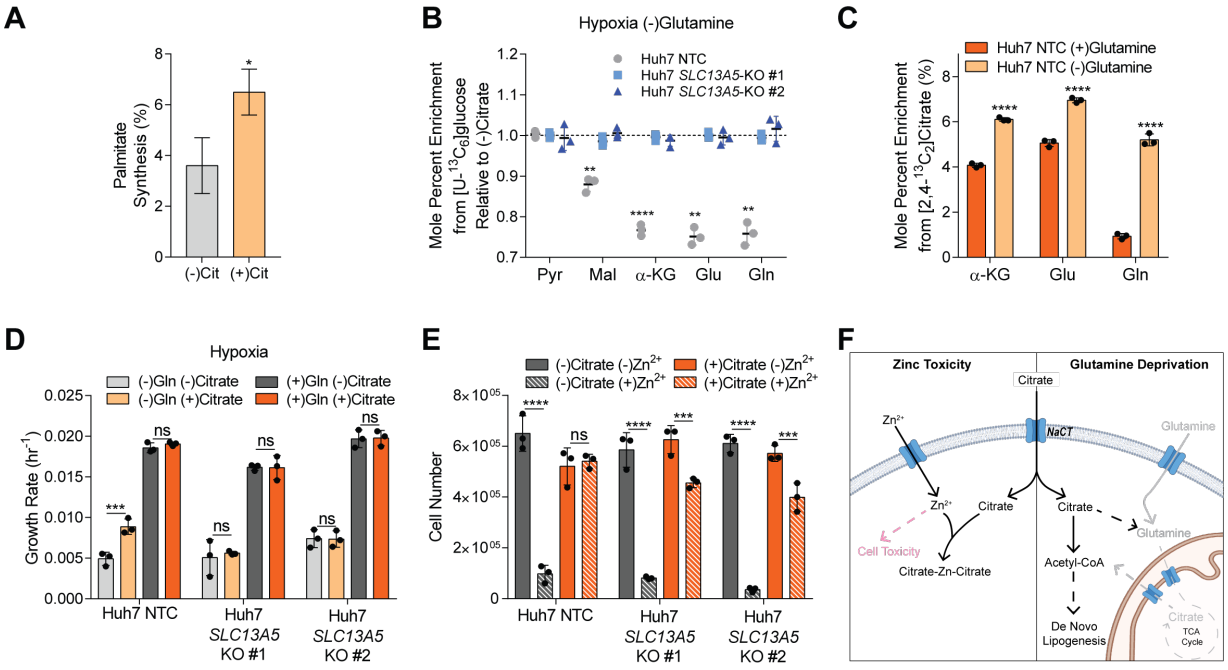

Figure 2.6: **NaCT facilitates growth under nutrient stress and resistance to zinc toxicity.** A) Palmitate synthesis in Huh7 NTC cells grown in high glucose DMEM without glutamine ± 500 μM citrate in hypoxia for 48 hours (n=3). B) Mole percent enrichment of metabolites from [U-$^{13}C_6$]glucose in Huh7 *SLC13A5*-KO cells grown without glutamine in hypoxia ± 500 μM citrate for 48 hours, relative to (-) citrate (n=3). C) Mole percent enrichment of TCA intermediates from [2,4-$^{13}C_2$]citrate in Huh7 NTC cells grown in hypoxia ± 4 mM glutamine for 48 hours (n=3). D) Growth rates of Huh7 NTC and *SLC13A5*-KO cells grown in high glucose DMEM ± 4 mM glutamine ± 500 μM citrate in hypoxia for 4 days. E) Cell numbers of Huh7 NTC and *SLC13A5*-KO cells grown in high glucose DMEM ± 5 mM citrate ± 300 μM ZnCl2 24 hours after zinc treatment in hypoxia. F) Schematic depicting extracellular citrate utilization during cellular stress. Gray indicates removed metabolites, pink indicates cytotoxic. Created with Biorender.com. Cit, citrate; Pyr, pyruvate; Mal, malate; α-KG, α-ketoglutarate; Glu, glutamate; Gln, glutamine. In (A) data are plotted as mean ± 95% confidence interval (CI). Statistical significance by non-overlapping confidence intervals, *. In (B-E) data are plotted as mean ± SD. Statistical significance is determined by two-sided Student's t-test relative to (-) citrate (B), (+) glutamine (C); or determined by Two-way ANOVA w/ Tukey's method for multiple comparisons relative to (-) citrate (D) or (-) Zn^{2+} conditions (E) with *, P value < 0.05; **, P value < 0.01; ***, P value < 0.001, ****, P value < 0.0001. Unless indicated, all data represent biological triplicates. See also Figure S5. Data shown are from one of at least two separate experiments.

neural tissue. Here we investigated how NaCT influences citrate metabolism in HCC cell lines and primary rat cortical neurons. We observed that NaCT-mediated citrate import contributes to cytosolic acetyl-CoA pools in HCC cells and neurons under distinct conditions. Hypoxic HCC cells metabolized extracellular citrate to fatty acids and TCA intermediates in a NaCT-dependent manner. When glutamine (and other nutrients) became limited, citrate supported the growth and lipid synthesis of HCC cell lines expressing NaCT. Furthermore, citrate supplementation enhanced the viability of HCC cell lines exposed to Zn^{2+} toxicity, but this protective effect was mitigated in *SLC13A5* KO cells that lacked NaCT expression.

Many cancer cell types increase glutamine utilization to support the TCA cycle and fatty acid biosynthesis *in vitro* [41, 42]; however reproducing this phenotype *in vivo* has generated mixed results [56–59]. One potential explanation for this discrepancy is the difference in nutrient profile of cell culture media compared to *in vivo* microenvironments [60–62]. Plasma and interstitial fluid contain metabolites that impact cellular metabolism but are routinely excluded from most cell culture medias. For instance, uric acid, a metabolite abundant in human plasma but absent in many cell culture medias, inhibited *de novo* pyrimidine synthesis in cancer cells *in vitro* [63]. Previous *in vitro* studies have observed that upregulated reductive glutamine catabolism supports fatty acid biosynthesis and defuses mitochondrial redox stress in hypoxia [41, 46]. In our study we found that reductive carboxylation was elevated in hypoxia in HepG2 and Huh7 cells but observed that extracellular citrate addition reduced flux through this pathway. Thus, uptake of extracellular citrate may provide an additional carbon source which is accessible to ACLY and downstream pathways, curtailing the need for other nutrients to support these processes. Similar observations of citrate import and metabolism were made in prostate cancer cells, which express the mitochondrial citrate carrier on their plasma membrane (pmCIC) [6]. On the other hand, we only observed appreciable citrate contributions to biosynthesis under selected conditions (hypoxia and glutamine restriction). These findings collectively suggest that citrate is not a major biosynthetic substrate but serves as a resource to cells when they experience distinct stresses (e.g.

ischemia, hypoxia, metal toxicity).

We also demonstrated that *SLC13A5* encoded NaCT is the primary mechanism for citrate import in HCC cells. No major changes in metabolism were observed beyond acetyl-CoA and TCA metabolism, and phenotypic responses were dependent upon expression of functional NaCT as well as citrate supplementation. Importantly, some prior studies observed signaling and growth phenotypes in cells upon knockdown or inhibition of NaCT in the absence of extracellular citrate [15–17], but our results indicate that citrate transport is a key function of the *SLC13A5* gene product. Indeed, we also found that citrate uptake by NaCT was protective against Zn^{2+} cytotoxicity in Huh7 cells. This finding mirrors those of previous studies which demonstrated that citrate or pyruvate administration were protective against Zn^{2+} cytotoxicity in neurons [53, 64]. Loss-of-function mutations in *SLC13A5* have been associated with early onset epilepsy, but the role of citrate metabolism in the pathophysiology of these patients is not well understood [18, 19, 22]. Various mechanisms have been proposed for this phenotype, including the susceptibility of NaCT-deficient neurons to increased synaptic Zn^{2+}concentrations induced upon neuronal activation [53]. Alternatively, others have hypothesized that improper NaCT function leads to increased synaptic citrate concentrations and excessive Zn^{2+} chelation which impairs NMDA receptor function and drives neuronal dysfunction [4]. Notably, we performed our study in HCC cells using supraphysiological concentrations of citrate and Zn^{2+} which might only occur transiently in the body. Furthermore, application of relatively severe metabolic stress (i.e. 1% oxygen and glutamine deprivation) to limit endogenous citrate was required to observe a growth phenotype in HCC cells. These findings suggest that biosynthetic defects may not be as relevant to the neurological phenotype of NaCT-deficient patients. As such, our results should motivate further investigation into the impact of *SLC13A5* mutations on homeostasis of potentially toxic metal cations such as Zn^{2+} and its relation to epilepsy. Ideally such studies would be performed in a more physiological model system such as NaCT knockout in brain organoids or animals which recapitulate the physiology of citrate better than 2D cell culture. Collectively, our results

demonstrate that NaCT mediates citrate transport and metabolism under conditions of metabolic stress. Our approach also highlights the utility of coordinated studies that involve targeting of disease-related metabolic genes in relevant cell types and deep metabolic profiling using flux analysis.

2.6 Acknowledgements

We thank all members of the Metallo laboratory for support and helpful discussions. This study was supported, in part, by US National Institutes of Health (NIH) grants R01CA234245 (C.M.M.), R21NS104513 (A.N.M., A.M.P.) and a TESS Research Foundation Grant (A.N.M., A.M.P.).

Chapter 2, in full, is a reprint of the material as it appears in "NaCT/SLC13A5 facilitates citrate import and metabolism under nutrient-limited conditions," *Cell Reports*, vol. 36, 2021. Avi Kumar is the primary author of this publication. Thekla Cordes, Anna E. Thalacker-Mercer, Ana M. Pajor, and Anne N. Murphy are co-authors on the paper. Christian M. Metallo is the corresponding author of this publication.

2.7 References

1. Wakil, S. J. & Abu-Elheiga, L. A. Fatty acid metabolism: Target for metabolic syndrome. *Journal of Lipid Research* **50,** S138–S143 (2009).

2. Costello, L. C. & Franklin, R. B. Plasma Citrate Homeostasis: How It Is Regulated; And Its Physiological and Clinical Implications. An Important, But Neglected, Relationship in Medicine. *HSOA Journal of Human Endocrinology* **1,** 1–8 (2016).

3. Zuckerman, J. M. & Assimos, D. G. Hypocitraturia: Pathophysiology and Medical Management. *Reviews in urology* **11,** 134–44 (2009).

4. Bhutia, Y. D., Kopel, J. J., Lawrence, J. J., Neugebauer, V. & Ganapathy, V. Plasma membrane Na+-coupled citrate transporter (SLC13A5) and neonatal epileptic encephalopathy. *Integrated Ocean Drilling Program: Preliminary Reports,* 1–69 (2017).

5. Costello, L. C. & Franklin, R. B. Concepts of citrate production and secretion by prostate 1. Metabolic relationships. *The Prostate* **18,** 25–46 (1991).

6. Mycielska, M. E., Dettmer, K., Rummele, P., Schmidt, K., Prehn, C., Milenkovic, V. M., Jagla, W., Madej, G. M., Lantow, M., Schladt, M., Cecil, A., Koehl, G. E., Eggenhofer, E., Wachsmuth, C. J., Ganapathy, V., Schlitt, H. J., Kunzelmann, K., Ziegler, C., Wetzel, C. H., Gaumann, A., Lang, S. A., Adamski, J., Oefner, P. J. & Geissler, E. K. Extracellular citrate affects critical elements of cancer cell metabolism and supports cancer development in vivo. *Cancer Research* **78,** 2513–2523 (2018).

7. Pajor, A. M. Molecular properties of the SLC13 family of dicarboxylate and sulfate transporters. *Pflügers Archiv - European Journal of Physiology* **451,** 597–605 (2006).

8. Pajor, A. M. Sodium-coupled dicarboxylate and citrate transporters from the SLC13 family. *Pflügers Archiv - European Journal of Physiology* **466,** 119–130 (2014).

9. Inoue, K., Zhuang, L., Maddox, D. M., Smith, S. B. & Ganapathy, V. Structure, function, and expression pattern of a novel sodium-coupled citrate transporter (NaCT) cloned from mammalian brain. *Journal of Biological Chemistry* **277,** 39469–39476 (2002).

10. Pajor, A. M. Molecular cloning and functional expression of a sodium-dicarboxylate cotransporter from human kidney. *American Journal of Physiology-Renal Physiology* **270,** F642–F648 (1996).

11. Huard, K., Brown, J., Jones, J. C., Cabral, S., Futatsugi, K., Gorgoglione, M., Lanba, A., Vera, N. B., Zhu, Y., Yan, Q., Zhou, Y., Vernochet, C., Riccardi, K., Wolford, A., Pirman, D., Niosi, M., Aspnes, G., Herr, M., Genung, N. E., Magee, V. T., Uccello, D. P., Loria, P., Di, L., Gosset, J. R., Hepworth, D., Rolph, T., Pfefferkorn, J. A. & Erion, D. M. Discovery and characterization of novel inhibitors of the sodium-coupled citrate transporter (NaCT or SLC13A5). *Scientific Reports* **5,** 1–13 (2015).

12. Sauer, D. B., Song, J., Wang, B., Hilton, J. K., Karpowich, N. K., Mindell, J. A., Rice, W. J. & Wang, D.-N. Structure and inhibition mechanism of the human citrate transporter NaCT. *Nature* **591,** 1–5 (2021).

13. Birkenfeld, A. L., Lee, H. Y., Guebre-Egziabher, F., Alves, T. C., Jurczak, M. J., Jornayvaz, F. R., Zhang, D., Hsiao, J. J., Martin-Montalvo, A., Fischer-Rosinsky, A., Spranger, J., Pfeiffer, A. F., Jordan, J., Fromm, M. F., König, J., Lieske, S., Carmean, C. M., Frederick, D. W., Weismann, D., Knauf, F., Irusta, P. M., De Cabo, R., Helfand, S. L., Samuel, V. T. & Shulman, G. I. Deletion of the mammalian INDY homolog mimics aspects of dietary restriction and protects against adiposity and insulin resistance in mice. *Cell Metabolism* **14,** 184–195 (2011).

14. Von Loeffelholz, C., Lieske, S., Neuschäfer-Rube, F., Willmes, D. M., Raschzok, N., Sauer, I. M., König, J., Fromm, M. F., Horn, P., Chatzigeorgiou, A., Pathe-Neuschäfer-Rube, A., Jordan, J., Pfeiffer, A. F., Mingrone, G., Bornstein, S. R., Stroehle, P., Harms, C., Wunderlich, F. T., Helfand, S. L., Bernier, M., de Cabo, R., Shulman, G. I., Chavakis, T., Püschel, G. P. & Birkenfeld, A. L. The human longevity gene homolog INDY and interleukin-6 interact in hepatic lipid metabolism. *Hepatology* **66,** 616–630 (2017).

15. Li, Z., Li, D., Choi, E. Y., Lapidus, R., Zhang, L., Huang, S.-m. & Shapiro, P. Silencing of solute carrier family 13 member 5 disrupts energy homeostasis and inhibits proliferation of human hepatocarcinoma cells. *Journal of Biological Chemistry* **292,** 13890–13901 (2017).

16. Phokrai, P., Poolsri, W.-a. & Suwankulanan, S. Suppressed de novo lipogenesis by plasma membrane citrate transporter inhibitor promotes apoptosis in HepG2 cells. *FEBS Open Bio* **8,** 986–1000 (2018).

17. Poolsri, W.-A., Phokrai, P., Suwankulanan, S., Phakdeeto, N., Phunsomboon, P., Pekthong, D., Richert, L., Pongcharoen, S. & Srisawang, P. Combination of Mitochondrial and Plasma Membrane Citrate Transporter Inhibitors Inhibits De Novo Lipogenesis Pathway and Triggers Apoptosis in Hepatocellular Carcinoma Cells. *Biomed Research International* **2018** (2018).

18. Hardies, K., Kovel, D. C. G. F., Weckhuysen, S., Asselbergh, B., Geuens, T., Deconinck, T., Azmi, A., May, P., Brilstra, E., Becker, F., Barisic, N., Craiu, D., Braun, K. P. J., Lal, D., Thiele, H., Schubert, J., Weber, Y. & Slot, V. R. Recessive mutations in SLC13A5 result in a loss of citrate transport and cause neonatal epilepsy, developmental delay and teeth hypoplasia. *Brain* **138,** 3238–3250 (2015).

19. Klotz, J., Porter, B. E., Colas, C., Schlessinger, A. & Pajor, A. M. Mutations in the Na+/citrate cotransporter NaCT (SLC13A5) in pediatric patients with epilepsy and developmental delay. *Molecular Medicine* **22,** 310–321 (2016).

20. Matricardi, S., De Liso, P., Freri, E., Costa, P., Castellotti, B., Magri, S., Gellera, C., Granata, T., Musante, L., Lesca, G., Oertel, J., Craiu, D., Hammer, T. B., Møller, R. S., Barisic, N., Abou Jamra, R., Polster, T., Vigevano, F. & Marini, C. Neonatal developmental and epileptic encephalopathy due to autosomal recessive variants in SLC13A5 gene. *Epilepsia* **61,** 2474–2485 (2020).

21. Schossig, A., Bloch-Zupan, A., Lussi, A., Wolf, N. I., Raskin, S., Cohen, M., Giuliano, F., Jurgens, J., Krabichler, B., Koolen, D. A., Sobreira, N. L. d. M., Maurer, E., Muller-Bolla, M., Penzien, J., Zschocke, J. & Kapferer-Seebacher, I. SLC13A5 is the second gene associated with Kohlschütter-Tönz syndrome. *Journal of Medical Genetics* **54,** 54–62 (2017).

22. Thevenon, J., Milh, M., Feillet, F., St-Onge, J., Duffourd, Y., Jugé, C., Roubertie, A., Héron, D., Mignot, C., Raffo, E., Isidor, B., Wahlen, S., Sanlaville, D., Villeneuve, N., Darmency-Stamboul, V., Toutain, A., Lefebvre, M., Chouchane, M., Huet, F., Lafon, A., De Saint Martin, A., Lesca, G., El Chehadeh, S., Thauvin-Robinet, C., Masurel-Paulet, A., Odent, S., Villard, L., Philippe, C., Faivre, L. & Rivière, J. B. Mutations in SLC13A5 cause autosomal-recessive epileptic encephalopathy with seizure onset in the first days of Life. *American Journal of Human Genetics* **95,** 113–120 (2014).

23. Bainbridge, M. N., Cooney, E., Miller, M., Kennedy, A. D., Wulff, J. E., Donti, T., Jhangiani, S. N., Gibbs, R. A., Elsea, S. H., Porter, B. E. & Graham, B. H. Analyses of SLC13A5-epilepsy patients reveal perturbations of TCA cycle. *Molecular Genetics and Metabolism* **121,** 314–319 (2017).

24. Henke, C., Töllner, K., van Dijk, R. M., Miljanovic, N., Cordes, T., Twele, F., Bröer, S., Ziesak, V., Rohde, M., Hauck, S. M., Vogel, C., Welzel, L., Schumann, T., Willmes, D. M., Kurzbach, A., El-Agroudy, N. N., Bornstein, S. R., Schneider, S. A., Jordan, J., Potschka, H., Metallo, C. M., Köhling, R., Birkenfeld, A. L. & Löscher, W. Disruption of the sodium-dependent citrate transporter SLC13A5 in mice causes alterations in brain citrate levels and neuronal network excitability in the hippocampus. *Neurobiology of Disease* **143,** 105018 (2020).

25. Glusker, J. P. Citrate Conformation and Chelation: Enzymatic Implications. *Accounts of Chemical Research* **13,** 345–352 (1980).

26. Gheller, B. J., Blum, J. E., Lim, E. W., Handzlik, M. K., Hannah Fong, E. H., Ko, A. C., Khanna, S., Gheller, M. E., Bender, E. L., Alexander, M. S., Stover, P. J., Field, M. S., Cosgrove, B. D., Metallo, C. M. & Thalacker-Mercer, A. E. Extracellular serine and glycine are required for mouse and human skeletal muscle stem and progenitor cell function. *Molecular Metabolism* **43,** 101106 (2021).

27. Gheller, B. J., Blum, J. E., Merritt, E. K., Cummings, B. P. & Thalacker-Mercer, A. E. Peptide YY (PYY) is expressed in human skeletal muscle tissue and expanding human muscle progenitor cells. *Frontiers in Physiology* **10,** 1–6 (2019).

28. Riddle, E. S., Bender, E. L. & Thalacker-Mercer, A. E. Expansion capacity of human muscle progenitor cells differs by age, sex, and metabolic fuel preference. *American Journal of Physiology - Cell Physiology* **315,** C643–C652 (2018).

29. Cordes, T., Lucas, A., Divakaruni, A. S., Murphy, A. N., Cabrales, P. & Metallo, C. M. Itaconate modulates tricarboxylic acid and redox metabolism to mitigate reperfusion injury. *Molecular Metabolism* **32,** 122–135 (2020).

30. Kumar, A., Mitchener, J., King, Z. A. & Metallo, C. M. Escher-Trace: A web application for pathway-based visualization of stable isotope tracing data. *BMC Bioinformatics* **21,** 1–10 (2020).

31. Cordes, T. & Metallo, C. M. in *High-Throughput Metabolomics: Methods and Protocols* (ed D'Alessandro, A.) 219–241 (Springer New York, New York, NY, 2019).

32. Young, J. D. INCA: a computational platform for isotopically non-stationary metabolic flux analysis. *Bioinformatics* (2014).

33. Ran, F. A., Hsu, P. D., Wright, J., Agarwala, V., Scott, D. A. & Zhang, F. Genome engineering using the CRISPR-Cas9 system. *Nature Protocols* **8,** 2281–2308 (2013).

34. Concordet, J. P. & Haeussler, M. CRISPOR: Intuitive guide selection for CRISPR/Cas9 genome editing experiments and screens. *Nucleic Acids Research* **46,** W242–W245 (2018).

35. Sanjana, N., Shalem, O. & Zhang, F. Improved vectors and genome-wide libraries for CRISPR screening. *Nat Methods* **11,** nmeth.3047 (2014).

36. Agarwala, R., Barrett, T., Beck, J., Benson, D. A., Bollin, C., Bolton, E., Bourexis, D., Brister, J. R., Bryant, S. H., Canese, K., Cavanaugh, M., Charowhas, C., Clark, K., Dondoshansky, I., Feolo, M., Fitzpatrick, L., Funk, K., Geer, L. Y., Gorelenkov, V., Graeff, A., Hlavina, W., Holmes, B., Johnson, M., Kattman, B., Khotomlianski, V., Kimchi, A., Kimelman, M., Kimura, M., Kitts, P., Klimke, W., Kotliarov, A., Krasnov, S., Kuznetsov, A., Landrum, M. J., Landsman, D., Lathrop, S., Lee, J. M., Leubsdorf, C., Lu, Z., Madden, T. L., Marchler-Bauer, A., Malheiro, A., Meric, P., Karsch-Mizrachi, I., Mnev, A., Murphy, T., Orris, R., Ostell, J., O'Sullivan, C., Palanigobu, V., Panchenko, A. R., Phan, L., Pierov, B., Pruitt, K. D., Rodarmer, K., Sayers, E. W., Schneider, V., Schoch, C. L., Schuler, G. D., Sherry, S. T., Siyan, K., Soboleva, A., Soussov, V., Starchenko, G., Tatusova, T. A., Thibaud-Nissen, F., Todorov, K., Trawick, B. W., Vakatov, D., Ward, M., Yaschenko, E., Zasypkin, A. & Zbicz, K. Database resources of the National Center for Biotechnology Information. *Nucleic Acids Research* **46,** D8–D13 (2018).

37. Grassian, A., Parker, S., Davidson, S., Divakaruni, A., Green, C., Zhang, X., Slocum, K., Pu, M., Lin, F., Vickers, C., C, J., Chung, F., Yin, H., Handly, E., Straub, C., Growney, J., Heiden, V. M., Murphy, A., Pagliarini, R. & Metallo, C. IDH1 Mutations Alter Citric Acid Cycle Metabolism and Increase Dependence on Oxidative Mitochondrial Metabolism (2014).

38. Pajor, A. M. & Sun, N. N. Single nucleotide polymorphisms in the human Na+-dicarboxylate cotransporter affect transport activity and protein expression. *American Journal of Physiology - Renal Physiology* **299,** 704–711 (2010).

39. Mills, E., Pierce, K., Jedrychowski, M., Garrity, R., Winther, S., Vidoni, S., Yoneshiro, T., Spinelli, J., Lu, G., Kazak, L., Banks, A., Haigis, M., Kajimura, S., Murphy, M., Gygi, S., Clish, C. & Chouchani, E. Accumulation of succinate controls activation of adipose tissue thermogenesis. *Nature* **560,** 102–106 (2018).

40. Ardlie, K. G. *et al.* The Genotype-Tissue Expression (GTEx) pilot analysis: Multitissue gene regulation in humans. *Science* **348,** 648–660 (2015).

41. Metallo, C. M., Gameiro, P. A., Bell, E. L., Mattaini, K. R., Yang, J., Hiller, K., Jewell, C. M., Johnson, Z. R., Irvine, D. J., Guarente, L., Kelleher, J. K., Vander Heiden, M. G., Iliopoulos, O. & Stephanopoulos, G. Reductive glutamine metabolism by IDH1 mediates lipogenesis under hypoxia. *Nature* **481,** 380–4 (2012).

42. Mullen, A. R., Wheaton, W. W., Jin, E. S., Chen, P. H., Sullivan, L. B., Cheng, T., Yang, Y., Linehan, W. M., Chandel, N. S. & Deberardinis, R. J. Reductive carboxylation supports growth in tumour cells with defective mitochondria. *Nature* **481,** 385–388 (2012).

43. Wise, D. R., Ward, P. S., Shay, J. E. S., Cross, J. R., Gruber, J. J. & Sachdeva, U. M. Hypoxia promotes isocitrate dehydrogenase-dependent carboxylation of α-ketoglutarate to citrate to support cell growth and viability. *Proc. Natl. Acad. Sci. U.S.A* **108,** 19611–19616 (2011).

44. Kamphorst, J. J., Chung, M. K., Fan, J. & Rabinowitz, J. D. Quantitative analysis of acetyl-CoA production in hypoxic cancer cells reveals substantial contribution from acetate. *Cancer & Metabolism* **2,** 23 (2014).

45. Fan, J., Kamphorst, J. J., Mathew, R., Chung, M. K., White, E., Shlomi, T. & Rabinowitz, J. D. Glutamine-driven oxidative phosphorylation is a major ATP source in transformed mammalian cells in both normoxia and hypoxia. *Molecular Systems Biology* **9,** 1–11 (2013).

46. Jiang, L., Shestov, A. A., Swain, P., Yang, C., Parker, S. J., Wang, Q. A., Terada, L. S., Adams, N. D., Mccabe, M. T., Pietrak, B., Schmidt, S., Metallo, C. M., Dranka, B. P., Schwartz, B. & Deberardinis, R. J. Reductive carboxylation supports redox homeostasis during anchorage-independent growth. *Nature* **532,** 255–258 (2016).

47. Jiang, L., Boufersaoui, A., Yang, C., Ko, B., Rakheja, D., Guevara, G., Hu, Z. & DeBerardinis, R. J. Quantitative metabolic flux analysis reveals an unconventional pathway of fatty acid synthesis in cancer cells deficient for the mitochondrial citrate transport protein. *Metabolic Engineering* **43,** 198–207 (2017).

48. Vacanti, N. M., Divakaruni, A. S., Green, C. R., Parker, S. J., Henry, R. R., Ciaraldi, T. P., Murphy, A. N. & Metallo, C. M. Regulation of substrate utilization by the mitochondrial pyruvate carrier. *Mol. Cell* **56,** 425–35 (2014).

49. Pajor, A. M., de Oliveira, C. A., Song, K., Huard, K., Shanmugasundaram, V. & Erion, D. M. Molecular Basis for Inhibition of the Na+/Citrate Transporter NaCT (SLC13A5) by Dicarboxylate Inhibitors. *Molecular Pharmacology* **90,** 755–765 (2016).

50. Assaf, S. Y. & Chung, S. H. Release of endogenous Zn2+ from brain tissue during activity. *Nature* **308,** 734–736 (1984).

51. Frederickson, C. J., Klitenick, M. A., Manton, W. I. & Kirkpatrick, J. B. Cytoarchitectonic distribution of zinc in the hippocampus of man and the rat. *Brain Research* **273,** 335–339 (1983).

52. Weiss, J. H., Sensi, S. L. & Koh, J. Y. Zn2+: A novel ionic mediator of neural injury in brain disease. *Trends in Pharmacological Sciences* **21,** 395–401 (2000).

53. Sul, J. W., Kim, T. Y., Yoo, H. J., Kim, J., Suh, Y. A., Hwang, J. J. & Koh, J. Y. A novel mechanism for the pyruvate protection against zinc-induced cytotoxicity: mediation by the chelating effect of citrate and isocitrate. *Archives of Pharmacal Research* **39,** 1151–1159 (2016).

54. Lemire, J., Mailloux, R. & Appanna, V. D. Zinc toxicity alters mitochondrial metabolism and leads to decreased ATP production in hepatocytes. *Journal of Applied Toxicology* **28,** 175–182 (2007).

55. Steinbach, O. M. & Wolterbeek, H. T. Effects of Zinc on Rat Hepatoma HTC Cells and Primary Cultured Rat Hepatocytes. *Toxicology and Applied Pharmacology* **118,** 245–254 (1993).

56. Davidson, S. M., Papagiannakopoulos, T., Olenchock, B. A., Heyman, J. E., Keibler, M. A., Luengo, A., Bauer, M. R., Jha, A. K., O'Brien, J. P., Pierce, K. A., Gui, D. Y., Sullivan, L. B., Wasylenko, T. M., Subbaraj, L., Chin, C. R., Stephanopolous, G., Mott, B. T., Jacks, T., Clish, C. B. & Van Der Heiden, M. G. Environment impacts the metabolic dependencies of ras-driven non-small cell lung cancer. *Cell Metabolism* **23,** 517–528 (2016).

57. Le, A., Lane, A. N., Hamaker, M., Bose, S., Gouw, A., Barbi, J., Tsukamoto, T., Rojas, C. J., Slusher, B. S., Zhang, H., Zimmerman, L. J., Liebler, D. C., Slebos, R. J., Lorkiewicz, P. K., Higashi, R. M., Fan, T. W. & Dang, V. C. Glucose-independent glutamine metabolism via TCA cycling for proliferation and survival in b cells. *Cell Metabolism* **15,** 110–121 (2012).

58. Son, J., Lyssiotis, C. A., Ying, H., Wang, X., Hua, S., Ligorio, M., Perera, R. M., Ferrone, C. R., Mullarky, E., Shyh-Chang, N., Kang, Y., Fleming, J. B., Bardeesy, N., Asara, J. M., Haigis, M. C., Depinho, R. A., Cantley, L. C. & Kimmelman, A. C. Glutamine supports pancreatic cancer growth through a KRAS-regulated metabolic pathway. *Nature* **496,** 101–105 (2013).

59. Tardito, S., Oudin, A., Ahmed, S. U., Fack, F., Keunen, O., Zheng, L., Miletic, H., Sakariassen, P. Ø., Weinstock, A., Wagner, A., Lindsay, S. L., Hock, A. K., Barnett, S. C., Ruppin, E., Harald MØrkve, S., Lund-Johansen, M., Chalmers, A. J., Bjerkvig, R., Niclou, S. P. & Gottlieb, E. Glutamine synthetase activity fuels nucleotide biosynthesis and supports growth of glutamine-restricted glioblastoma. *Nature Cell Biology* **17,** 1556–1568 (2015).

60. Ackermann, T. & Tardito, S. Cell Culture Medium Formulation and Its Implications in Cancer Metabolism. *Trends in Cancer* **5,** 329–332 (2019).

61. Rossiter, N. J., Huggler, K. S., Adelmann, C. H., Keys, H. R., Soens, R. W., Sabatini, D. M. & Cantor, J. R. CRISPR screens in physiologic medium reveal conditionally essential genes in human cells. *Cell Metabolism* (2021).

62. Voorde, V. J., Ackermann, T., Pfetzer, N., Sumpton, D., Mackay, G., Kalna, G., Nixon, C., Blyth, K., Gottlieb, E. & Tardito, S. Improving the metabolic fidelity of cancer models with a physiological cell culture medium. *Science Advances* **5** (2019).

63. Cantor, J. R., Monther, A., Kanarek, N., Freinkman, E., Gao, X., Louissaint, A., Lewis, C. A. & Sabatini, D. M. Physiologic Medium Rewires Cellular Metabolism and Reveals Uric Acid as an Endogenous Inhibitor of UMP Synthase. *Cell* **169,** 258–272.e17 (2017).

64. Yoo, M. H., Lee, J. Y., Lee, S. E., Koh, J. Y. & Yoon, Y. H. Protection by pyruvate of rat retinal cells against zinc toxicity in vitro, and pressure-induced ischemia in vivo. *Investigative Ophthalmology and Visual Science* **45,** 1523–1530 (2004).

Chapter 3

ATP-citrate lyase deficiency highlights critical sources of lipogenic acetyl-CoA in cancer cells

3.1 Abstract

Cancer cells constitutively upregulate fatty acid biosynthesis to support their rapid proliferation. By fully profiling the redundancies in this pathway, more effective therapeutic strategies can be developed to target cancer cell growth. To analyze the metabolic rewiring that occurs when lipogenic acetyl-CoA synthesis is disrupted in cancer cells, we apply ^{13}C isotope tracing to non-small cell lung cancer (NSCLC) and hepatoma cell lines deficient in ATP-Citrate Lyase (ACLY) and/or the cytosolic isoform of Acetyl-CoA Synthetase (ACSS2). Knockout of ACLY in multiple cell lines reduced *de novo* lipogenesis (DNL), increased reliance on extracellular lipids, and upregulated ACSS2 expression with acetate becoming the primary lipogenic substrate when available. Knockout of both ACLY and ACSS2 (DKO) eliminated acetate utilization for DNL. ACLY-deficient cells were shown to rely on non-canonical sources of acetyl-CoA including *de*

novo acetate production as well as peroxisomal β-oxidation. Collectively, our results highlight the critical roles of biosynthetic and catabolic lipid metabolism in maintaining acetyl-CoA levels in cancer cells, particularly in the context of targeting ACLY.

3.2 Introduction

Cancer cells constitutively upregulate biosynthetic pathways to support their proliferation. Fatty acid synthesis is particularly essential for providing fatty acyl-CoAs for lipid synthesis associated with membrane biogenesis, energy storage, and protein modification [1]. While tumors and many healthy tissues readily take up and metabolize lipids from the diet [1], *de novo* lipogenesis (DNL) is required for some tumors and cell types to proliferate [2, 3]. Fatty acids are synthesized from two carbon acyl-units provided by cytosolic acetyl-CoA (AcCoA). Canonically, mitochondrial citrate is exported to the cytosol and catabolized by ATP-Citrate Lyase (ACLY) to generate acetyl-CoA and oxaloacetate. This cytosolic acetyl-CoA is elongated by acetyl-CoA Carboxylase (ACC) and fatty acid synthase (FASN) to generate fatty acids. The fatty acids can be further modified and incorporated into lipids in the endoplasmic reticulum (ER). Initial studies focused on the action of FASN and found that its inhibition reduced body weight of mice [4] as well as oncogene expression [5] and *in vivo* growth [6] of human breast cancer cell lines. Further, knockout and pharmacological inhibition of acetyl-CoA carboxylase have both been linked to decreased fatty acid synthesis and reduced tumor proliferation [7].

Because of its role in the synthesis of lipogenic acetyl-CoA as well as its function linking metabolism and epigenetic regulation as well as DNA repair via histone acetylation [8–10], ACLY has garnered interest as a target for cancer therapeutics. Upregulation of ACLY expression has been identified in a number of cancers including breast, liver, bladder, stomach, colorectal, glioblastoma, and lung cancers when compared to surrounding healthy tissues [11–17]. Additionally, in patients with gastric adenocarcinoma [18] and lung adenocarcinomas [12],

overexpression and activation of ACLY is significantly associated with poor prognosis. Further, both pharmacological inhibition and genetic knockdown of ACLY have been demonstrated to reduce lipogenesis and cancer cell proliferation [19–26], supporting the link between ACLY activity and tumor growth.

Acetyl-CoA synthetase isoform 2 (ACSS2) synthesizes cytosolic acetyl-CoA utilizing acetate rather than citrate [27]. The acetyl-CoA synthetase family of enzymes (ACSS1, ACSS2, and ACSS3) are the rate limiting enzymes involved in acetate catabolism in mammalian cells [28]. ACSS1 is mitochondrially expressed, while ACSS2 is primarily expressed in the cytosol [29]. ACSS2 has garnered interest as a cancer target as high expression of ACSS2 is associated with poor prognosis in breast, glioblastoma, ovarian, and lung cancers [30–32]. Nutrient deprivation, including hypoxia and lipid depletion, were shown to upregulate ACSS2 expression and acetate catabolism for *de novo* lipogenesis in cancer cells, suggesting that ACSS2 provides a mode of metabolic plasticity to cancer cells under stress [33]. Furthermore, mouse embryonic fibroblasts (MEFs) deficient in ACLY upregulate ACSS2 protein expression and increase utilization of acetate for cytosolic acetyl-CoA generation [34], highlighting the essentiality of lipogenic acetyl-CoA synthesis in proliferative cells. However, the ability of cancer cells to rely on acetate rather than citrate for cytosolic acetyl-CoA generation and DNL is unclear.

Peroxisomal acetyl-CoA, derived from β-oxidation of very long chain (VLCFA) and branched chain fatty acids (BCFA), contributes to DNL malonyl-CoA pools in heart and liver tissue [35–37]. Additionally, peroxisomal enzymes involved in oxidation of branched chain fatty acids (HSD17B4, ACOX3) are overexpressed in cancerous prostate tissue compared to paired healthy tissue [38]. However, the extent to which peroxisomal β-oxidation of fatty acids serves as a source of lipogenic acetyl-CoA in cancer cells has not been extensively studied.

Here we apply mass spectrometry, stable isotope tracing and isotopomer spectral analysis (ISA) to analyze the metabolic rewiring that occurs when acetyl-CoA synthesis is systematically compromised in cancer cells. We genetically engineered cancer cell lines deficient in ACLY

and/or ACSS2 using CRISPR/Cas9. While knockout of ACLY decreased DNL under basal conditions, cells were able to sustain FASN flux and/or growth through use of exogenous acetate or serum lipids. On the other hand, knockout of both ACLY and ACSS2 induced a growth limiting stress regardless of media nutrient status. Finally, we found that with ACLY deficiency, peroxisomal β-oxidation becomes a significant source of lipogenic acetyl-CoA and cells are sensitized to inhibition of peroxisomal β-oxidation. Collectively, our study highlights the rewiring of fatty acid metabolism that occurs when the cytosolic acetyl-CoA generating enzymes, ACLY and ACSS2, are compromised and identifies ACLY as a potent metabolic vulnerability that can be targeted therapeutically to influence cancer growth.

3.3 Materials and Methods

3.3.1 Cell Lines

A549 and HepG2 cells were obtained from HDBiosciences, HAP1 cells were obtained from Horizon Discovery, and 634T cells were obtained from the Shaw Lab at the Salk Institute for Biological Sciences. All cell lines were incubated at 37C with 5% CO2 and cultured using Dulbecco's Modified Eagle Media (DMEM) with 10% Fetal Bovine Serum and 1% Penicillin-Streptomycin. Cells tested negative for mycoplasma contamination. All media were adjusted to pH = 7.3.

3.3.2 Cell Proliferation and ^{13}C Tracing

Proliferation studies were performed on 12 well plates with an initial cell number of 50,000/well for A549s and 100,000/well for HepG2s. Cells were plated in growth media and allowed to adhere for 24 hours before changing to the specified growth media. Cell counts were performed at days 0 and 4 using a hemocytometer.

^{13}C isotope tracing media was formulated using glucose and glutamine free DMEM 5030 supplemented with either 20 mM [U-$^{13}C_6$]glucose, 4 mM [U-$^{13}C_5$]glutamine, 1 mM [1,2-$^{13}C_2$]acetate, 5 mM [3-$^{13}C_1$]pyruvate, 500 μM [U-$^{13}C_8$] octanoate or 500 μM [2,4-$^{13}C_2$]citrate (Cambridge Isotopes) and 10% dialyzed FBS. ^{13}C palmitate studies were performed with 200 μM albumin conjugated [U-$^{13}C_{16}$] palmitate and 10% dialyzed delipidated FBS. All studies were performed with a final concentration of 20 mM glucose and 4 mM glutamine. Cultured cells were washed with 1 mL PBS prior to applying tracing media for 6-72 hours as indicated in figure legends.

3.3.3 Drug Dose Response

Drug dose response studies were performed on 96 well plates with an initial cell number of 2,500/well. Cells were plated in growth media and allowed to adhere for 24 hours before changing to the specified growth media with the indicated concentration of thioridazine. After 4 days wells were washed 2x with tap water, 50uL of 0.5% crystal violet staining solution were added to each well for 20 minutes. Crystal violet stain was removed and wells were washed 3x with tap water and air dried overnight. Next, 200 uL methanol was added to each well and plates were incubated at room temperature for 20 minutes. Optical density of wells were measured at 570 nm on a TECAN plate reader.

3.3.4 Ferroptosis Assay

Wildtype and ACLY/ACSS2-DKO cells were plated in 96 well plates with an initial cell number of 5,000/well. Cells were plated in growth media and allowed to adhere for 24 hours before changing to the specified growth media with 2μM ML210 and/or 6μM Ferrostatin. After 48 hours, cell viability was quantified using the PrestoBlue^{TM} Cell Viability Kit (Thermo, A13261) and a TECAN plate reader.

3.3.5 CRISPR/Cas9 engineering knockout lines

ACLY, ACSS2, and ACLY/ACSS2 knockout clones were generated using the strategy described previously [39]. Briefly, tandem guide RNAs (gRNAs) were designed to target human ACLY (gRNA sequences: gaccagctgatcaaacgtcg, ggggtcaggatgaacgtgtg) and ACSS2 (gRNA sequences: ctcgcggtagcgctgcagcg, aatggaaaagggattccggg) using the online CRISPR guide tool provided by the Zhang Lab at MIT (http://tools.genome-engineering.org). The gRNA duplex were cloned into lentiCRISPRv2 (Addgene #52961) [40]. A549 and HepG2 cells were transfected with the ACLY and/or ACSS2 specific gRNA to generate pooled knockouts. After puromycin selection, single-cell clones were isolated by diluting the pooled knockout lines at 1 cell/100 μL and plating 100 μL into each well of a 96 well plate. Clones were maintained by exchanging media every 3-5 days. Clones were validated by PCR and western blot.

3.3.6 Isotopomer Spectral Analysis (ISA)

Isotopomer spectral analysis (ISA) was performed to estimate the percent of newly synthesized palmitate as well as the contribution of a tracer of interest to the lipogenic acetyl-CoA pool (Cordes and Metallo, 2019; Young, 2014). Parameters for contribution of ^{13}C tracers to lipogenic acetyl-CoA (D value) and percentage of newly synthesized fatty acid (g(t) value) and their 95% confidence intervals are then calculated using a best-fit model from the INCA MFA software package. Experimental fatty acid labeling from [U-$^{13}C_6$]glucose, [U-$^{13}C_5$]glutamine, [1,2-$^{13}C_2$]acetate, [U-$^{13}C_8$] octanoate or [2,4-$^{13}C_2$]citrate after a 24-72 hour trace, as indicated in figure legends, was compared to simulated labeling using a reaction network where C16:0 is formed from the condensation of 8 AcCoA. ISA data is plotted as mean $\pm$ 95% CI. $*$ indicates statistical significance by non-overlapping confidence intervals.

3.3.7 Metabolic Flux Analysis

Metabolic fluxes for citrate were calculated by collecting media at time 0 and spent media after 72 hours. Spent media was centrifuged at 300g for 5 min, to remove cell debris. Cell counts were performed at time 0 and after 72 hours as well. To calculate glucose, lactate, glutamine, and glutamate uptake fluxes media metabolites were quantified using a Yellow Springs Instruments (YSI) Biochemistry Analyzer 2950.

3.3.8 Metabolite Extraction and GC-MS Analysis

At the conclusion of the tracer experiment, media was aspirated. Then, cells were rinsed twice with 0.9% saline solution and lysed with 250 μL ice-cold methanol. After 1 minute, 100 μL water containing 1 μg/ml norvaline was added to each sample and vortexed for one minute. 250 μL chloroform was added to each sample, and all were vortexed again for 1 minute. After centrifugation at 21,130 g for 10 minutes at 4°C, 250 μL of the upper aqueous layer was collected and evaporated under vacuum at 4°C. Then, 250 μL of the upper aqueous layer was collected and evaporated under air at room temperature.

Dried polar and nonpolar metabolites were processed for gas chromatography (GC) mass spectrometry (MS) as described previously in Cordes and Metallo (Cordes and Metallo, 2019). Briefly, polar metabolites were derivatized using a Gerstel MultiPurpose Sampler (MPS 2XL). Methoxime-tBDMS derivatives were formed by addition of 15 μL 2% (w/v) methoxylamine hydrochloride (MP Biomedicals, Solon, OH) in pyridine and incubated at 45°C for 60 minutes. Samples were then silylated by addition of 15 μL of N-tert-butyldimethylsily-N-methyltrifluoroacetamide (MTBSTFA) with 1% tert-butyldimethylchlorosilane (tBDMS) (Regis Technologies, Morton Grove, IL) and incubated at 45°C for 30 minutes. Nonpolar metabolites were saponified and transesterified to fatty acid methyl esters (FAMEs) by adding 500 μL of 2% H2SO4 in methanol to the dried nonpolar layer and heating at 50°C for 1 hour. FAMEs were then

extracted by adding 100 μL of a saturated salt solution and 500 μL hexane and vortexing for 1 minute. The hexane layer was removed, evaporated, and resuspended with 60μL hexane for injection.

Derivatized polar samples were injected into a GC-MS using a DB-35MS column (30m x 0.25mm i.d. x 0.25μm, Agilent J&W Scientific, Santa Clara, CA) installed in an Agilent 7890B GC system integrated with an Agilent 5977a MS. Samples were injected at a GC oven temperature of 100°C which was held for 1 minute before ramping to 255°C at 3.5°C/min then to 320°C at 15°C/min and held for 3 minutes. Electron impact ionization was performed with the MS scanning over the range of 100-650 m/z for polar metabolites.

Derivatized nonpolar samples were injected into a GC-MS using a Fame Select column (100m x 0.25mm i.d. x 0.25μm, Agilent J&W Scientific, Santa Clara, CA) installed in an Agilent 7890A GC system integrated with an Agilent 5977A MS. Samples were injected at a GC oven temperature of 80°C which was held for 1 minute before ramping to 170°C at 20°C/min then to 188°C at 1°C/min then to 250°C at 20°C/min and held for 10 minutes. Electron impact ionization was performed with the MS scanning over the range of 54-400 m/z for nonpolar metabolites.

Metabolite levels and mass isotopomer distributions were analyzed with an in house Matlab script which integrated the metabolite fragment ions and corrected for natural isotope abundances. Mole percent enrichment calculations were performed using Escher-Trace [41].

3.3.9 LC-MS/MS analysis

Lipids were extracted from confluent 6 well plates after growth in DMEM with 10% FBS and 1% penicillin streptomycin for 48 hours. At the conclusion of the experiment, media was aspirated, and the cells were rinsed twice with saline solution. Cells were lysed with 750 μL of ice cold 1:1 methanol/water solution for 5 minutes on ice and scraped into Eppendorf tubes. Next, 500 μL of ice cold chloroform and 50 uL butylated hydroxytoluene (1mg/mL in methanol) were added to the tube, along with EquiSLASH (Avanti, Croda International Plc, 330731) internal

standard. The tubes were vortexed for 5 min and centrifuged at 21,230g at 4°C for 5 min. The lower organic phase was collected and 2 μL of formic acid was added to the remaining polar phase which was re-extracted with 500uL of chloroform. Combined organic phases were dried under nitrogen and the pellet was resuspended in 50 μL isopropyl alcohol.

A Q Exactive orbitrap mass spectrometer with a Vanquish Flex Binary UHPLC system (Thermo Scientific) was used with an Accucore C30, 150 x 2.1mm, 2.6 μm particle (Thermo) column at 40°C to quantify lipids. 5 μL of sample was injected. Chromatography was performed using a gradient of 40:60 v/v water: acetonitrile with 10 mM ammonium formate and 0.1% formic acid (mobile phase A) and 10:90 v/v acetonitrile: 2-propanol with 10 mM ammonium formate and 0.1% formic acid (mobile phase B), both at a flow rate of 0.2 mL/min. The LC gradient ran from 30% to 43% B from 3-8 min, then from 43% to 50% B from 8-9min, then 50-90% B from 9-18min, then 90-99% B from 18-26 min, then held at 99% B from 26-30min, before returning to 30% B in 6 min and held for a further 4 min.

Lipids were analyzed in positive mode using spray voltage 3.2 kV. Sweep gas flow was 1 arbitrary units, auxiliary gas flow 2 arbitrary units and sheath gas flow 40 arbitrary units, with a capillary temperature of 325°C. Full MS (scan range 200-2000 m/z) was used at 70,000 resolution with 1e6 automatic gain control and a maximum injection time of 100 ms. Data dependent MS2 (Top 6) mode at 17,500 resolution with automatic gain control set at 1e5 with a maximum injection time of 50 ms was used. Data was analyzed using El-Maven and Escher-Trace software, and peaks were normalized to the Avanti EquiSPLASH internal standard.

3.3.10 Western Blot

A549, HepG2, HAP1, and 634T wildtype, ACLY and/or ACSS2-KO cell lines were lysed in M-PER buffer (Thermo Scientific, 78501) with 1x protease inhibitor (Sigma-Aldrich). Protein concentrations were determined using the Pierce^{TM} BCA protein assay kit (Thermo Scientific, 23225). 15 μg protein were loaded and separated using 4–15% Mini-PROTEAN TGX^{TM}

Precast SDS-PAGE Gels (Bio-rad, #4561086). Samples were then transferred to nitrocellulose membranes for immunoblotting. Total acetylated-lysine (Cell Signaling Technology, 9441), β-Actin (Sigma, A5441), ACLY (Cell Signaling Technology, 13390), and ACSS2 (Cell Signaling Technology, 3658) antibodies were used to probe their respective targets. Anti-Rabbit horseradish peroxidase-conjugated secondary antibody (Millipore, AP132P) was used for imaging.

3.3.11 RNA isolation and quantitative RT-PCR

Total RNA was purified from cultured cells using Trizol Reagent (Life Technologies) per manufacturer's instructions. First-strand cDNA was synthesized from 1 μg of total RNA using iScript Reverse Transcription Supermix for RT-PCR (Bio-Rad Laboratories) according to the manufacturer's instructions. Individual 20 μl SYBR Green real-time PCR reactions consisted of 1 μl of diluted cDNA, 10 μl of SYBR Green Supermix (Bio-Rad), and 1 μl of each 5 μM forward and reverse primers. For standardization of quantification, 18S was amplified simultaneously. The PCR was carried out on 96-well plates on a CFX Connect Real time System (Bio-Rad), using a three-stage program provided by the manufacturer: 95°C for 3 min, 40 cycles of 95°C for 10 s and 60°C for 30 s.

3.3.12 Quantification and Statistical Analysis

Statistical analyses were performed using Graphpad PRISM. Unless indicated, all results shown as mean $\pm$ SD of cellular triplicates obtained from one representative experiment as specified in each figure legend. P values were calculated using a Student's two-tailed t test, One-way ANOVA w/ Dunnet's method for multiple comparisons, or Two-way ANOVA w/ Tukey's method for multiple comparisons; *, P value < 0.05; **, P value < 0.01; ***, P value < 0.001, ****, P value < 0.0001. Unless indicated, all normalization and statistical tests compared to wildtype cells.

3.4 Results

3.4.1 *ACLY*-knockout rewires central carbon metabolism and leads to a reduction of palmitate synthesis in cancer cells

ACLY-knockout (*ACLY*-KO) clones were generated using CRISPR/Cas9 in A549 human NSCLC cells, 634T murine NSCLC cells, HepG2 hepatocarcinoma cells, and HAP1 cells (Fig. 1B, S1A). We observed increased protein expression of ACSS2 in the A549 and HepG2 *ACLY*-KO cell lines (Fig. 1B, S1A), consistent with previous results in MEFs [34]. The growth rate of the *ACLY*-KO A549, 634T, and HAP1 cells was marginally lower compared to the wildtype cells, while HepG2 *ACLY*-KO cells showed an over 50% reduction in growth rate compared to the wildtype cells (Fig.1C, S1B). In A549 cells, *ACLY*-KO resulted in decreased glucose uptake and increased glutamine uptake (Fig. 1D). To better understand how ACLY-deficiency alters intracellular metabolism, we cultured A549 clones in the presence of [U-$^{13}C_6$]glucose, and [U-$^{13}C_5$]glutamine in DMEM and quantified isotope enrichment in downstream metabolite pools. Enrichment of TCA cycle intermediates from glutamine in A549 *ACLY*-KO cells was elevated, consistent with extracellular flux results (Fig.1E). This may indicate that *ACLY*-KO induces oxidative stress, as increased glutamine catabolism has been found to be integral to maintaining redox homeostasis in cancer cells through multiple mechanisms [42, 43]. On the other hand, changes in TCA enrichment from glucose were inconsistent (Fig. S1C).

Next, we utilized [2,4-$^{13}C_2$]citrate to investigate intracellular citrate dynamics in HepG2 *ACLY*-KO cells, as HCC cells are capable of extracellular citrate uptake. Catabolism of [2,4-$^{13}C_2$]citrate provides insight into compartment specific metabolism of extracellular citrate as M2 labeling of TCA intermediates will result from direct mitochondrial catabolism of labeled citrate, while M1 isotopologues will be formed if the tracer is first catabolized in the cytosol by ACLY (Fig. S1D). When culturing HepG2 wildtype and *ACLY*-KO cells in the presence of 500 μM [2,4-$^{13}C_2$]citrate, we found that the ratio of M1/M2 labeling on malate, aspartate, succinate, and

fumarate was significantly decreased in the *ACLY*-KO cells (Fig. S1E). Furthermore, the relative abundance of M2 alpha-ketoglutarate was comparable to M1 labeling in wildtype cells but was significantly greater in the *ACLY*-KO cells (Fig. S1F). Additionally, enrichment of palmitate was minimal in the *ACLY*-KO cells compared to WT (Fig. S1G). These labeling patterns indicate that upon *ACLY*-KO, cytosolic citrate is shuttled back into the mitochondria, as has been observed in anchorage independent conditions [44, 45], and also shuttled to cytosolic alpha-ketoglutarate by cytosolic aconitase (ACO1) and isocitrate dehydrogenase (IDH1) reactions.

Next, we applied ISA to quantify palmitate synthesis and the contribution of [U-$^{13}C_6$]glucose to the lipogenic acetyl-CoA pool. *ACLY*-deficiency profoundly decreased palmitate synthesis compared to control cells (Fig. 1F, S1H, I). Notably, *ACLY*-KO cells maintained some flux from [U-$^{13}C_6$]glucose to lipogenic acetyl-CoA such that 20% of palmitate carbon was derived from glucose in A549 and HepG2 cells, while the smaller decrease was detected in 634T cells (Fig 1G, S1J). Collectively, these results indicate that ACLY deficiency effectively decreases FASN flux and alters cytosolic citrate shuttling under normal culture conditions while reducing growth slightly.

3.4.2 *ACLY*-knockout *de novo* lipogenesis flux and growth in delipidated media is rescued by extracellular acetate

Under conditions where glucose-derived citrate is limiting, such as hypoxia, acetate can be "activated" by acetyl-CoA synthetase enzymes. As protein expression of ACSS2 was markedly increased in *ACLY*-KO cells (Fig. 1B, S1A), we hypothesized that acetate utilization may compensate for loss of ACLY. Supplementation of 1 mM [1,2-$^{13}C_2$]acetate to cultures significantly increased palmitate synthesis in cells lacking ACLY (Fig. 2A, S2A). Acetate became the primary lipogenic substrate in all tested *ACLY*-KO cell lines (Fig. 2B, S2B) but only contributed between 5-40% of lipogenic acetyl-CoA pools in control cells. De novo palmitate synthesis was significantly rescued in the *ACLY*-KO cells grown with acetate (Fig. 2A, S2A)

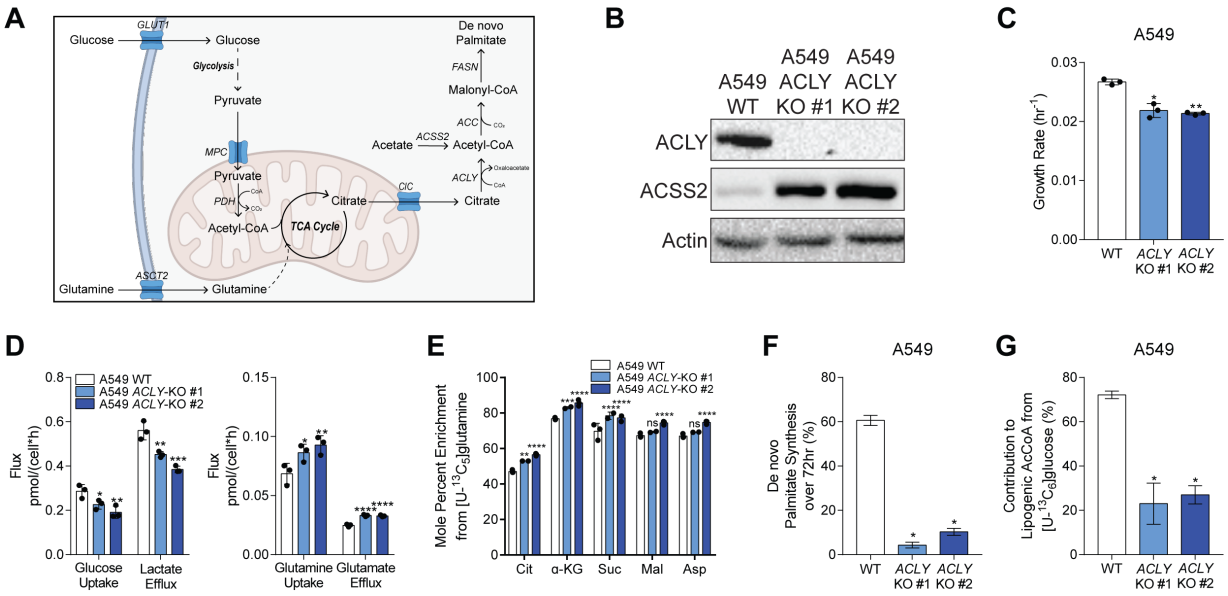

Figure 3.1: ***ACLY*-KO rewires central carbon metabolism and leads to a reduction of palmitate synthesis in cancer cells.** A) Canonical *de novo* lipogenesis pathway. B) Western Blots of ACLY, ACSS2, and actin in A549 WT and *ACLY*-KO cells. C) Growth rates of A549 WT and *ACLY*-KO cells grown in high glucose DMEM +10% FBS for 4 days. D) Glucose uptake, lactate efflux (left) and glutamine uptake, glutamate efflux (right) in A549 WT and *ACLY*-KO cells cultured in high glucose DMEM +10% dFBS for 72 hours (n=3). E) Mole percent enrichment of TCA intermediates from [U-$^{13}C_5$]glutamine in A549 *ACLY*-KO clones cultured in high glucose DMEM +10% dFBS for 72 hours (n=3). F) De novo synthesis of palmitate in A549 *ACLY*-KO cells cultured in high glucose DMEM +10% dFBS for 72 hours (n=3). G) Percent of lipogenic acetyl-CoA contributed by [U-$^{13}C_6$]glucose in A549 *ACLY*-KO cells cultured in high glucose DMEM +10% dFBS 72 hours (n=3). In (C-G) data are plotted as mean $\pm$ SD. Statistical significance is relative to WT as determined by One-way ANOVA w/ Dunnet's method for multiple comparisons (C-E) with *, P value < 0.05; **, P value < 0.01; ***, P value < 0.001, ****, P value < 0.0001. In (F,G) data are plotted as mean $\pm$ 95% confidence interval (CI). Statistical significance by non-overlapping confidence intervals, *. Unless indicated, all data represent biological triplicates. Data shown are from one of at least two separate experiments. See also Figure S1.

compared to those grown in the absence of acetate (Fig. 1F, S1F,G) in all cell lines.

To explore if the suppression of fatty acid synthesis observed with *ACLY*-KO had proliferative consequences, we measured the growth rate of control and *ACLY*-deficient cell lines in various culture media. In DMEM + 10% dialyzed FBS (dFBS), *ACLY*-KO cells grew comparably to control cells (Fig 2C, S2C). However, when we removed serum lipids growth of all *ACLY*-KO cells was severely compromised (Fig 2C, S2C). Addition of 1 mM exogenous acetate enhanced the growth of all *ACLY*-KO cells while having no impact on growth rates of control cells (Fig 2C, S2C). The most dramatic growth impact of acetate was observed in cultures grown in delipidated serum (Fig 2C, S2C). As shown earlier, HepG2 *ACLY*-KO cells grew slower than wildtype cells in all conditions, however their growth was further reduced in delipidated serum and was significantly rescued with acetate supplementation (Fig S2C). These results suggest that rescue of fatty acid synthesis by provision of acetate salvages the proliferative capacity of *ACLY*-deficient cells (Fig. 2D).

3.4.3 *ACSS2*-attenuates catabolism of exogenous acetate with minimal effect on growth

To directly address the role of ACSS2 in facilitating acetate to lipid biosynthesis, we examined the growth and metabolism of A549 and HepG2 cells lacking ACSS2 (Fig. 3A, S3A). No upregulation of ACLY expression was observable in *ACSS2*-knockout (*ACSS2*-KO) cells (Fig. 3A, S3A). While the conversion of [1,2-$^{13}C_2$]acetate to palmitate was significantly decreased upon ACSS2 knockout (Fig. 3B, S3B), there was no impact on palmitate synthesis rates in cells lacking ACSS2 (Fig. 3C, S3C). Consistent with these findings, the growth rates of both A549 and HepG2 cell lines were minimally impacted by *ACSS2*-KO in lipid-replete medium (Fig. 3D, S3D). However, HepG2 *ACSS2*-KO cells observed a significant growth defect compared to wildtype in lipid-depleted media, matching previous studies which found *ACSS2*-KO was detrimental to cancer cell growth in conditions of metabolic stress [31, 33]. A549 *ACSS2*-KO cell growth

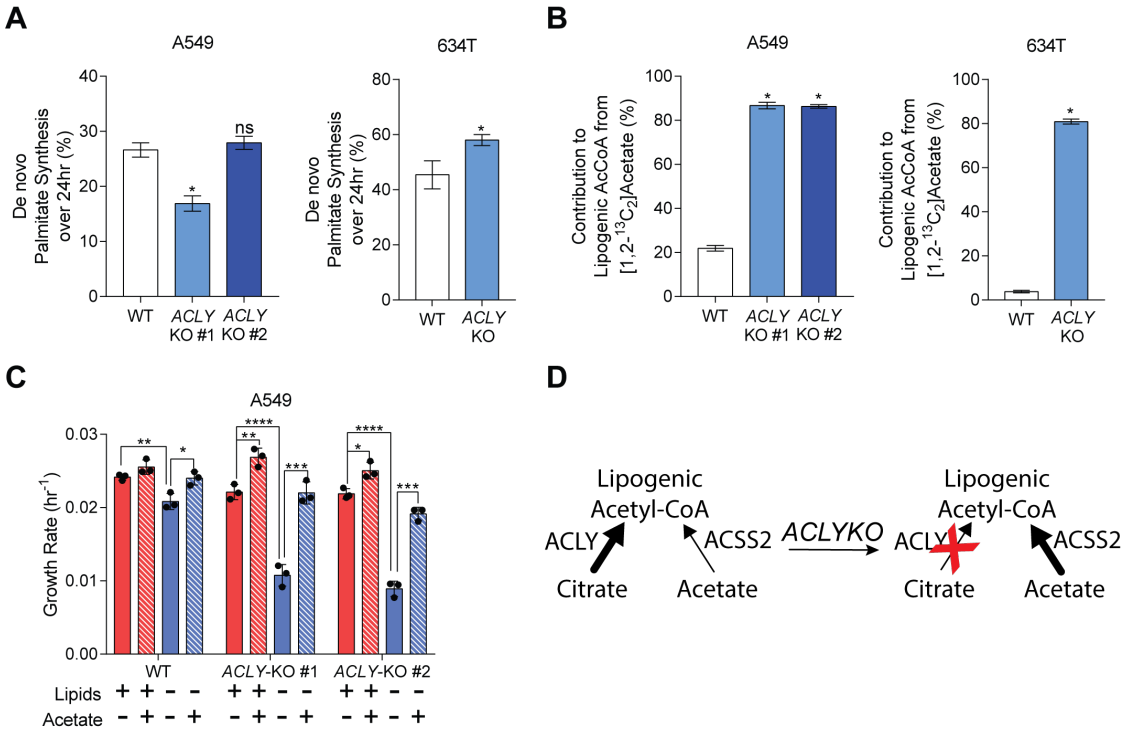

Figure 3.2: ***ACLY*-knockout *de novo* lipogenesis flux and growth in delipidated media is rescued by extracellular acetate.** A) De novo synthesis of palmitate in A549 (left) and 634T (right) WT and *ACLY*-KO cells cultured in high glucose DMEM +10% dFBS + 1 mM acetate for 24 hours (n=3). B) Percent of lipogenic acetyl-CoA contributed by [1,2-$^{13}C_2$]acetate in A549 (left) and 634T (right) and *ACLY*-KO cells cultured in high glucose DMEM +10% dFBS + 1 mM acetate for 24 hours (n=3). C) Growth rates of A549 WT and *ACLY*-KO cells grown in high glucose DMEM +10% dFBS or delipidated dFBS $\pm$ 1 mM acetate for 4 days (n=3). D) Schematic of lipogenic acetyl-CoA synthesis in *ACLY*-KO cells. In (A,B) data are plotted as mean $\pm$ 95% confidence interval (CI). Statistical significance by non-overlapping confidence intervals, *. In (C) data are plotted as mean $\pm$ SD. Statistical significance is determined by Two-way ANOVA w/ Tukey's method for multiple comparisons with *, P value < 0.05; **, P value < 0.01; ***, P value < 0.001, ****, P value < 0.0001. Unless indicated, all data represent biological triplicates. Data shown are from one of at least two separate experiments. See also Figure S2.

remained unaffected by media delipidation (Fig. 3D, S3D). A similar phenotype bifurcation between the cell lines was observed previously, as HepG2 cells exhibited a greater growth rate reduction upon loss of ACLY compared to A549 cells (Fig. 1C, S1B). Interestingly, mRNA expression of ACSS1 and ACSS3, both mitochondrial isozymes of ACSS2, were significantly elevated in HepG2 hepatoma cells compared to A549 NSCLC cells (Fig. 3E). Furthermore, [1,2-$^{13}C_2$]acetate enrichment of TCA intermediates was significantly higher in HepG2 cells compared to A549 cells (Fig. 3F,G), suggesting that mitochondrial ACSS1 and/or ACSS3 compete with cytosolic ACSS2 for utilization of acetate. This competition may influence acetate shuttling acetate to mitochondrial TCA metabolism, lipogenesis, and epigenetic regulation via histone acetylation which has previously been shown to be altered by ACSS1/2 knockdown [46].

3.4.4 *ACLY/ACSS2* double knockout inhibits palmitate synthesis from glucose and acetate

Next we quantified the growth and metabolism of A549 *ACLY/ACSS2* double knockout (*ACLY/ACSS2*-DKO) cells, in order to explore how cancer cells bear extreme restriction of lipogenic acetyl-CoA synthesis (Fig. 4A). Growth of A549 *ACLY/ACSS2*-DKO cells was significantly impaired relative to wildtype in all conditions tested. Serum delipidation further decreased growth of *ACLY/ACSS2*-DKO cells (Fig. 4B) and there was no growth rescue with acetate supplementation (Fig 4B). Consistent with these results, palmitate enrichment from [U-$^{13}C_6$]glucose and [1,2-$^{13}C_2$]acetate was minimal in *ACLY/ACSS2*-DKO cells, indicating that neither metabolite is able to support lipogenesis when both ACLY and ACSS2 are inactive (Fig. 4C, D).

Incorporation of polyunsaturated fatty acids (PUFA) into phosphatidylcholine (PC) lipids and triacyl glycerides (TAG) was elevated in *ACLY*-KO and *ACLY/ACSS2*-DKO cells, indicating increased reliance on media fatty acids for membrane lipid synthesis in ACLY deficient cells (Fig. 4E, S4A,B). PUFA containing lipids have been shown to be susceptible to lipid peroxidation

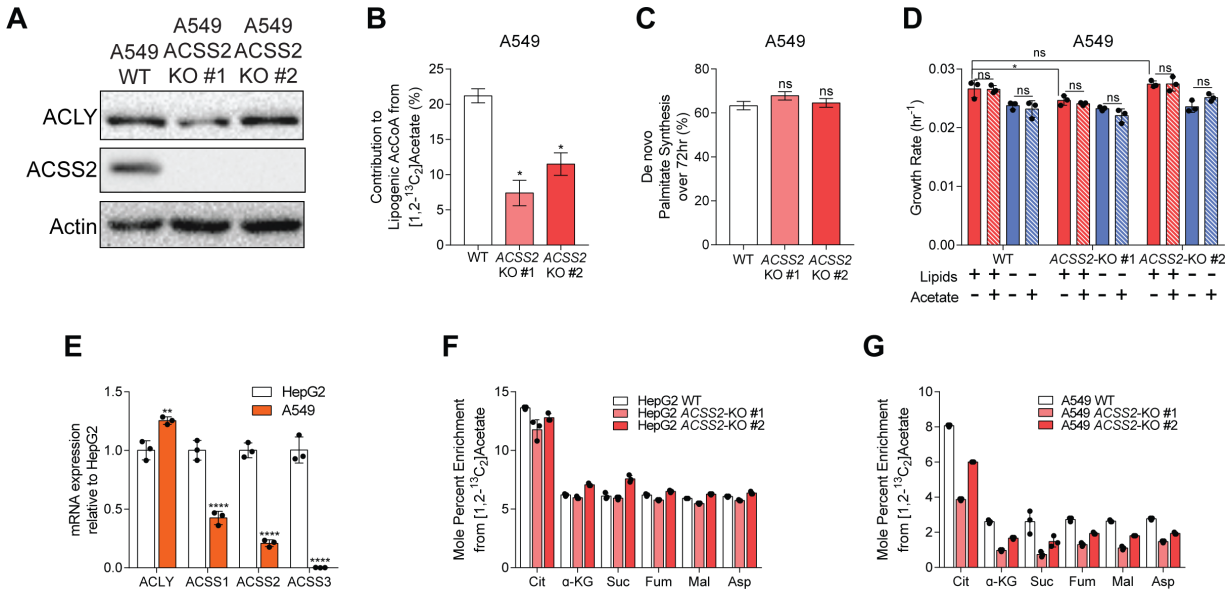

Figure 3.3: ***ACSS2*-KO attenuates catabolism of exogenous acetate with minimal effect on glucose catabolism** A) Western Blots of ACLY, ACSS2, and actin in A549 WT and *ACSS2*-KO cells. B) Percent of lipogenic acetyl-CoA contributed by [1,2-$^{13}C_2$] acetate in A549 *ACSS2*-KO cells cultured in high glucose DMEM +10% dFBS + 1 mM acetate for 24 hours (n=3). C) De novo synthesis of palmitate in A549 *ACSS2*-KO cells cultured in high glucose DMEM +10% dFBS for 72 hours (n=3). D) Growth rates of A549 WT and *ACSS2*-KO cells grown in high glucose DMEM +10% dFBS or delipidated dFBS $\pm$ 1 mM acetate for 4 days (n=3). E) mRNA expression of acetyl-CoA generating enzymes in HepG2 and A549 cells (n=3). F) Mole percent enrichment of TCA intermediates from [1,2-$^{13}C_2$] acetate in HepG2 *ACSS2*-KO cells cultured in high glucose DMEM +10% dFBS + 1 mM acetate for 24 hours (n=3). G) Mole percent enrichment of TCA intermediates from [1,2-$^{13}C_2$] acetate in A549 *ACSS2*-KO cells cultured in high glucose DMEM +10% dFBS + 1 mM acetate for 24 hours (n=3). In (B, C) data are plotted as mean $\pm$ 95% confidence interval (CI). Statistical significance by non-overlapping confidence intervals, *. In (D-G) data are plotted as mean $\pm$ SD. Statistical significance is determined by Two-way ANOVA w/ Tukey's method for multiple comparisons (D); or relative to HepG2 as determined by two-sided Student's t-test (G) with *, P value < 0.05; **, P value < 0.01; ***, P value < 0.001, ****, P value < 0.0001. Unless indicated, all data represent biological triplicates. Data shown are from one of at least two separate experiments. See also Figure S3.

(ref), and we found that the PUFA enriched *ACLY/ACSS2*-DKO cells were more susceptible to ferroptosis induced by application of the glutathione peroxidase 4 (GPX4) inhibitor, ML210, than wildtype cells (Fig. 4F). Despite these alterations in lipid metabolism, whole cell protein acetylation was maintained in *ACLY*-KO and *ACLY/ACSS2*-DKO cells (Fig 4G,H), suggesting that NSCLC cells are able to sustain acetyl-CoA availability through pathways independent of ACLY and ACSS2.

3.4.5 Disruption of canonical acetyl-CoA synthesis induces alternative synthesis pathways.

The continued availability of acetyl-CoA for histone acetylation suggests the existence of non-canonical mechanisms of acetyl-CoA generation in ACLY deficient cells. To resolve these mechanisms, we cultured A549 *ACLY*-KO and *ACLY/ACSS2*-DKO cells with ^{13}C-labeled glucose, glutamine, and pyruvate for 72 hours and quantified isotope enrichment in palmitate. In theory, knockout of ACLY will eliminate glucose to palmitate carbon transfer (Fig. 5A); however, A549 *ACLY*-KO cells traced with [U-$^{13}C_6$]glucose continued to sustain labeling on newly synthesized palmitate (Fig. 5B). We observed similar results using [3-$^{13}C_1$]pyruvate (Fig. 5C). Culture of the *ACLY*-KO and *ACLY/ACSS2*-DKO cells with [U-$^{13}C_5$]glutamine yielded insignificant enrichment of palmitate (Fig. 5D), suggesting the existence of an citrate/ACLY-independent lipogenic pathway which utilizes glucose and/or pyruvate, but not glutamine, for acetyl-CoA synthesis. In order to enrich palmitate, glutamine carbon first enters the mitochondria and is catabolized either oxidatively or reductively to citrate. Thus lack of palmitate enrichment from glutamine indicates a mitochondrial citrate independent mechanism of carbon transfer from pyruvate to DNL in the ACLY-KO cells. Previous studies have found that carnitine acetyl-transferase (CRAT) actively exports mitochondrial CoA intermediates supporting fatty acid synthesis in adipose tissue [47], however, we see no evidence of direct export of mitochondrial acetyl-CoA for fatty acid synthesis in our system as we observed minimal labeling of palmitate from [U-$^{13}C_6$]glucose in the A549

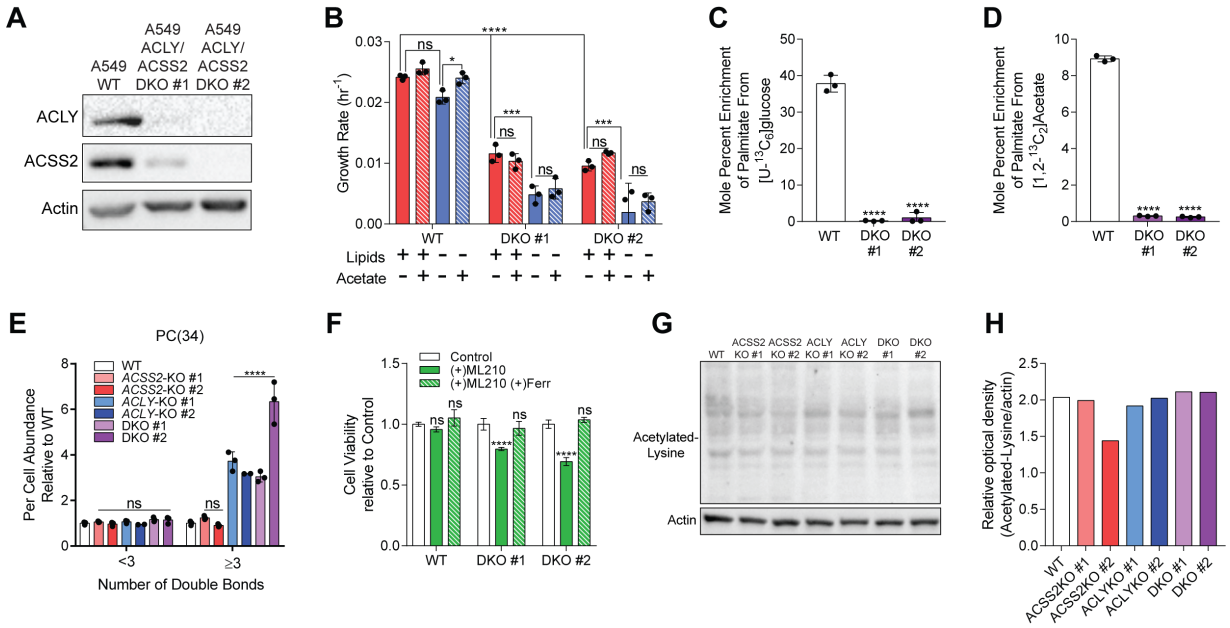

Figure 3.4: ***ACLY/ACSS2*-DKO cells are reliant on extracellular lipids, with minimal change in protein acetylation.** A) Western Blots of ACLY, ACSS2, and actin in A549 WT and *ACLY/ACSS2*-DKO cells. B) Growth rates of A549 WT and *ACLY/ACSS2*-DKO cells grown in high glucose DMEM +10% dFBS or delipidated dFBS ± 1 mM acetate for 4 days (n=3). C) Mole percent enrichment of palmitate from [U-$^{13}C_6$] glucose in A549 *ACLY/ACSS2*-DKO cells cultured in high glucose DMEM +10% dFBS for 72 hours (n=3). D) Mole percent enrichment of palmitate from [1,2-$^{13}C_2$] acetate in A549 *ACLY/ACSS2*-DKO cells cultured in high glucose DMEM +10% dFBS + 1 mM acetate for 24 hours (n=3). E) PC(34) abundance of A549 WT, *ACSS2*-KO, *ACLY*-KO, *ACLY/ACSS2*-DKO cells cultured in high glucose DMEM +10% FBS for 2 days (n=3). F) Cell viability of A549 WT and *ACLY/ACSS2*-DKO cells cultured in DMEM+10% dFBS ± 2 μM ML210 and/or 2 μM Ferrostatin for 48 hours (n=4). G) Western Blots of acetylated-lysine and actin in A549 WT, *ACSS2*-KO, *ACLY*-KO, *ACLY/ACSS2* DKO whole cell lysates. H) Relative optical density of acetylated-lysine/actin in A549 WT, *ACSS2*-KO, *ACLY*-KO, *ACLY/ACSS2*-DKO whole cell lysates (n=1). In (B-F) data are plotted as mean ± SD. Statistical significance is determined by Two-way ANOVA w/ Tukey's method for multiple comparisons (B); or relative to WT as determined by One-way ANOVA w/ Dunnet's method for multiple comparisons (C-F) with *, P value < 0.05; **, P value < 0.01; ***, P value < 0.001, ****, P value < 0.0001. Unless indicated, all data represent biological triplicates. Data shown are from one of at least two separate experiments. See also Figure S4.

ACLY/ACSS2-DKO (Fig. 5A) despite significant enrichment of pyruvate and citrate, implying enrichment of mitochondrial acetyl-CoA (Fig. S5A,B).

Notably, ^{13}C pyruvate, and glutamine also yielded negligible label on palmitate in A549 *ACLY/ACSS2*-DKO cells (Fig. 5B, C, D), suggesting that ACSS2 is involved in the aforementioned conversion of pyruvate to acetyl-CoA (Fig. 5A). Such a reaction mechanism has been demonstrated in a previous study which found that reactive oxygen species were able to facilitate oxidative decarboxylation of pyruvate to acetate [48]. However, the extracellular acetate/ACSS2 and lipid dependency of *ACLY*-KO cell growth suggests this *de novo* acetate flux is not significant enough to sustain the biosynthetic needs of the ACLY deficient cells tested here (Fig. 2C, S2C).

To further investigate non-canonical lipogenic acetyl-CoA sources in the *ACLY*-KO cells, we traced the A549 cell panel with 200 μM albumin conjugated [U-$^{13}C_{16}$] palmitate for 6 hours. Citrate enrichment from [U-$^{13}C_{16}$] palmitate was elevated in the *ACLY/ACSS2*-DKO cells (Fig. S5C) but intracellular palmitate labeling was minimally impacted compared to wildtype (Fig. 5E). Intracellular palmitate enrichment was slightly elevated in the *ACLY*-KO cells (Fig. 5E). These labeling distributions imply increased mitochondrial fatty acid oxidation flux in *ACLY/ACSS2*-DKO cells compared to wildtype. Interestingly, when observing stearate labeling, the ratio of M18 stearate (formed from M16 palmitate and ^{13}C palmitate β-oxidation derived M2 acetyl-CoA) to M16 stearate (formed from M16 palmitate and unlabeled acetyl-CoA) was over 4-fold higher in *ACLY*-KO cells and 15-fold higher in *ACLY/ACSS2*-DKO cells compared to wildtype cells (Fig. 5F), suggesting that *ACLY*-deficient cells utilize fatty acid carbon for non-mitochondrial lipogenic acetyl-CoA generation (Fig 5G).

Figure 3.5: **Disruption of canonical acetyl-CoA synthesis induces alternative synthesis pathways.** A) Schematic showing *de novo* acetate synthesis in *ACLY*-KO cells. Dashed lines represent multiple reactions. B) Enrichment (1-M0) of palmitate from [U-$^{13}C_6$] glucose in A549 WT, *ACLY*-KO, *ACLY/ACSS2*-DKO cells cultured in high glucose DMEM +10% dFBS for 72 hours (n=3). C) Enrichment (1-M0) of palmitate from [3-$^{13}C_1$] pyruvate in A549 WT, *ACLY*-KO, *ACLY/ACSS2*-DKO cells cultured in high glucose DMEM +10% dFBS + 5mM pyruvate for 72 hours (n=3). D) Enrichment (1-M0) of palmitate from [U-$^{13}C_5$] glutamine in A549 WT, *ACLY*-KO, *ACLY/ACSS2*-DKO cells cultured in high glucose DMEM +10% dFBS for 72 hours (n=3). E) Percent labeling of M16 palmitate from [U-$^{13}C_{16}$] palmitate in A549 WT, *ACSS2*-KO, *ACLY*-KO, *ACLY/ACSS2*-DKO cells cultured in high glucose DMEM +10% delipidated dFBS for 6 hours (n=3). F) Fraction of M18/M16 stearate from [U-$^{13}C_{16}$] palmitate in A549 WT, *ACSS2*-KO, *ACLY*-KO, *ACLY/ACSS2*-DKO cells cultured in high glucose DMEM +10% delipidated dFBS for 6 hours (n=3). G) Schematic of [U-$^{13}C_{16}$]palmitate elongation to stearate. In (B-F) data are plotted as mean $\pm$ SD. Statistical significance relative to WT as determined by One-way ANOVA w/ Dunnet's method for multiple comparisons (B-F) with *, P value < 0.05; **, P value < 0.01; ***, P value < 0.001, ****, P value < 0.0001. Unless indicated, all data represent biological triplicates. Data shown are from one of at least two separate experiments. See also Figure S5.

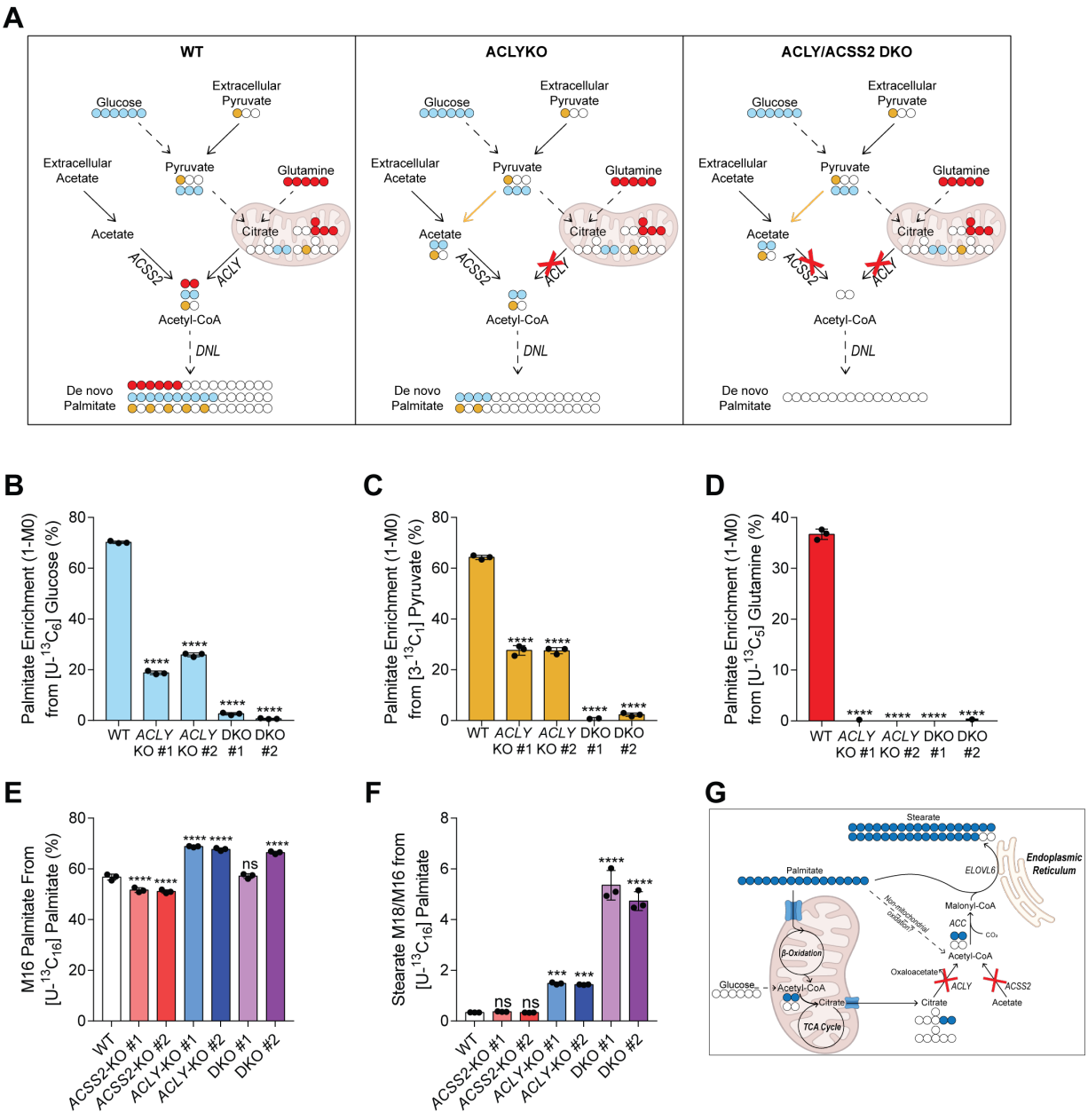
A
WT
ACLYKO
ACLY/ACSS2 DKO
Glucose
Extracellular Pyruvate
Extracellular Acetate
Pyruvate
Glutamine
Acetate
Citrate
ACSS2
ACLY
Acetyl-CoA
DNL
De novo Palmitate
B
Palmitate Enrichment (1-M0) from [U-13C6] Glucose (%)
C
Palmitate Enrichment (1-M0) from [3-13C1] Pyruvate (%)
D
Palmitate Enrichment (1-M0) from [U-13C5] Glutamine (%)
WT
ACLY KO #1
ACLY KO #2
DKO #1
DKO #2
E
M16 Palmitate From [U-13C16] Palmitate (%)
F
Stearate M18/M16 from [U-13C16] Palmitate
ns
G
Stearate
Palmitate
ELOVL6
Endoplasmic Reticulum
Malonyl-CoA
ACC
Acetyl-CoA
β-Oxidation
Oxaloacetate
Glucose
Citrate
TCA Cycle
Acetate

3.4.6 Peroxisomal β-oxidation is a major source of lipogenic acetyl-CoA in the absence of ACLY

Given our previous results, suggesting fatty acid oxidation is an active lipogenic acetyl-CoA source in *ACLY*-deficient cells, we hypothesized that peroxisomes serve as an alternate source of acetyl-CoA, as they are the site of β-oxidation for very long chain fatty acids (VLCFAs) and branched chain fatty acids (BCFAs) [49]. We cultured the A549 cell panel in media supplemented with 500 μM [U-$^{13}C_8$]octanoate, which passively diffuses across the mitochondrial as well as peroxisomal membranes [36]. Notably, octanoate contributed significantly to fatty acid biosynthesis in *ACLY/ACSS2*-DKO cells (Fig. 6A,B, S6A), in contrast to the glucose, acetate, or glutamine tracers (Fig 4C, D, 5D). The *ACLY*-KO and *ACLY/ACSS2*-DKO cells had a 2.5-fold and 4-fold increase, respectively, in enrichment of the lipogenic acetyl-CoA pool from octanoate compared to the wildtype or *ACSS2*-KO cells (Fig. 6A). A similar increase in lipogenic acetyl-CoA labeling from [U-$^{13}C_8$]octanoate was observed in HepG2 and 634T *ACLY*-KO clones (Fig. S6A). Indeed, supplementation of octanoate enabled detection of newly synthesized fatty acids in *ACLY/ACSS2*-DKO cells for the first time (Fig. 6B). Citrate enrichment from octanoate was also increased in the *ACLY*-KO and *ACLY/ACSS2*-DKO cells (Fig. S6B); however, based on the previous [U-$^{13}C_5$]glutamine tracing results (Fig. 5D), mitochondrial citrate minimally contributes to fatty acid synthesis in the *ACLY*-KO or *ACLY/ACSS2*-DKO cells.

Next, we profiled whole lipid abundances in the A549 cell panel. When observing at the summed total abundance of TAG and PC lipids, changes with ACLY and/or ACSS2 knockout were insignificant. However, there were significant alterations in the acyl-chain composition of the lipids, specifically there was a significant depletion of VLCFA containing TAGs and PCs in *ACLY*-KO and *ACLY/ACSS2*-DKO cells. This depletion is complete for nearly all measurable VLCFA containing saturated, mono-, and di-unsaturated TAG species (Fig. S6C) as well as saturated, and mono-unsaturated PC species (Fig S6D). Depletion of VLCFAs in lipids suggests

that these fatty acids are instead diverted for oxidation in the peroxisome. Additionally, per cell abundances of peroxisome derived phosphatidylethanolamine ether lipids were significantly elevated in A549 *ACLY/ACSS2*-DKO and 634T *ACLY*-KO cells (Fig 6F), further supporting the theory that peroxisomal activity is upregulated upon *ACLY*-KO.

Multiple mechanisms have been suggested for shuttling peroxisomal acetyl-CoA to the cytosol in mammalian cells. One mechanism involves conversion of peroxisomal acetyl-CoA to acetate by a thioesterase and subsequent export and conversion back to acetyl-CoA by ACSS2 in the cytosol. Alternatively, export of peroxisomal acetyl-CoA by a carnitine shuttle mechanism, similar to that utilized for shuttling fatty acids into the mitochondria, has been proposed previously [50–52]. The elevated palmitate enrichment from [U-$^{13}C_8$]octanoate observed in *ACLY/ACSS2*-DKO cells suggests that these cells employ an acetate-independent acetyl-CoA export mechanism, potentially via activity of peroxisomal CRAT (Fig. 6G).

To elucidate how impairing peroxisomal β-oxidation affects proliferation of the A549 KO panel, we quantified the growth of each cell line in response to increasing concentrations of the peroxisomal β-oxidation inhibitor, Thioridazine (Thio) [53, 54]. Strikingly, *ACLY*-KO and *ACLY/ACSS2*-DKO cells were significantly more sensitive to Thio treatment than wildtyoe or *ACSS2*-KO cells (Fig. 6H). Application of 2.5 μM Thio had no appreciable impact on growth of wildtype and *ACSS2*-KO cells, but significantly decreased proliferation of *ACLY*-KO and *ACLY/ACSS2*-DKO cells (Fig. 6I). Notably, the growth impairment of *ACLY*-KO cells in response to Thio treatment was completely ameliorated with acetate supplementation (Fig. 6J, S6E), suggesting that ACSS2 and acetate provide a more significant acetyl-CoA synthesis flux than peroxisomal β-oxidation in ACLY deficient cells. Together, these results suggest that peroxisomal β-oxidation provides a significant growth sustaining level of acetyl-CoA in the absence of functional ACLY.

Figure 3.6: **Peroxisomal β-oxidation becomes a major source of lipogenic acetyl-CoA with ACLYKO and *ACLY/ACSS2* DKO.** A) Percent of lipogenic acetyl-CoA contributed by [U-$^{13}C_8$] octanoate in A549 WT, *ACSS2*-KO, *ACLY*-KO, *ACLY/ACSS2*-DKO cells cultured in high glucose DMEM +10% dFBS + 500 μM octanoate for 24 hours (n=3). B) De novo synthesis of palmitate in A549 WT, *ACSS2*-KO, *ACLY*-KO, *ACLY/ACSS2*-DKO cells cultured in high glucose DMEM +10% dFBS + 500 μM octanoate for 24 hours (n=3). C) Total abundance of TAGs and PCs in A549 WT, *ACSS2*-KO, *ACLY*-KO, *ACLY/ACSS2*-DKO cells cultured in high glucose DMEM +10% FBS for 2 days (n=3). D) Total abundance of saturated, mono- and di-unsaturated TAGs per cell of A549 WT, *ACSS2*-KO, *ACLY*-KO, *ACLY/ACSS2*-DKO cells cultured in high glucose DMEM +10% FBS for 2 days (n=3). E) Total abundance of saturated and monounsaturated PCs per cell of A549 WT, *ACSS2*-KO, *ACLY*-KO, *ACLY/ACSS2*-DKO cells cultured in high glucose DMEM +10% FBS for 2 days (n=3). F) Total abundance abundances of PE ether lipids per cell of A549 (left) and 634T (right) WT, *ACSS2*-KO, *ACLY*-KO, and/or *ACLY/ACSS2*-DKO cells cultured in high glucose DMEM +10% FBS for 2 days (n=3). G) Schematic of peroxisomal acetyl-CoA synthesis from [U-$^{13}C_8$] octanoate in *ACLY/ACSS2*-DKO cells. Filled circles are ^{13}C, empty circles are 12C. H) Dose response of A549 WT, *ACSS2*-KO, *ACLY*-KO, *ACLY/ACSS2*-DKO cells cultured in high glucose DMEM +10% dFBS to Thioridazine over 4 days (n=3). I) Growth rates of A549 WT and *ACLY/ACSS2*-DKO cells grown in high glucose DMEM +10% dFBS $\pm$ 2.5 μM thioridazine relative to DMSO for 4 days (n=3). J) Growth rates of A549(left) and 634T (right) WT and *ACLY*-KO cells grown in high glucose DMEM +10% dFBS $\pm$ 2.5 μM thioridazine $\pm$ 1 mM acetate for 4 days (n=3). In (A, B) data are plotted as mean $\pm$ 95% confidence interval (CI). Statistical significance by non-overlapping confidence intervals, *. In (C-F, H-J) data are plotted as mean $\pm$ SD. Statistical significance as determined by One-way ANOVA w/ Dunnet's method for multiple comparisons relative to WT(C-F), DMSO (I,J) with *, P value < 0.05; **, P value < 0.01; ***, P value < 0.001, ****, P value < 0.0001. Unless indicated, all data represent biological triplicates. Data shown are from one of at least two separate experiments. See also Figure S6.

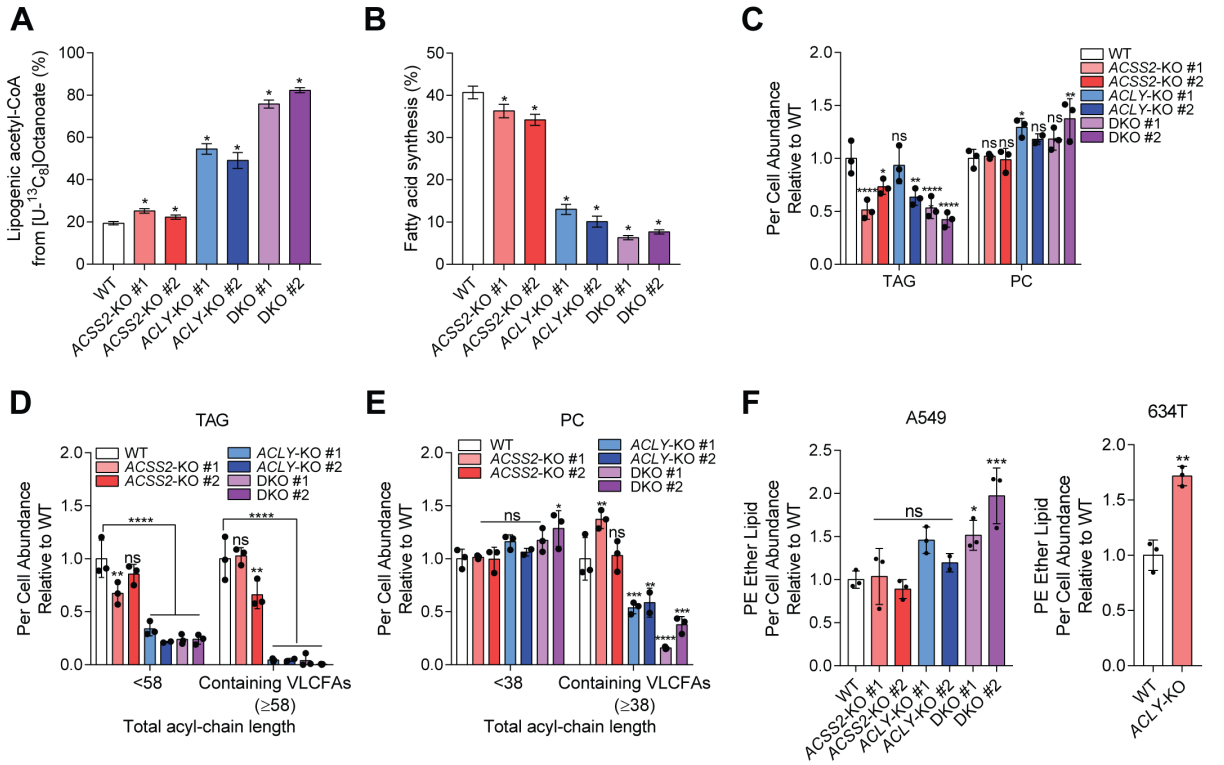
A
Lipogenic acetyl-CoA from [U-13C8]Octanoate (%)
WT
ACSS2-KO #1
ACSS2-KO #2
ACLY-KO #1
ACLY-KO #2
DKO #1
DKO #2
B
Fatty acid synthesis (%)
C
Per Cell Abundance Relative to WT
TAG
PC
D
TAG
<58
Containing VLCFAs (≥58)
Total acyl-chain length
E
PC
<38
Containing VLCFAs (≥38)
F
A549
634T
PE Ether Lipid Per Cell Abundance Relative to WT
WT
ACLY-KO

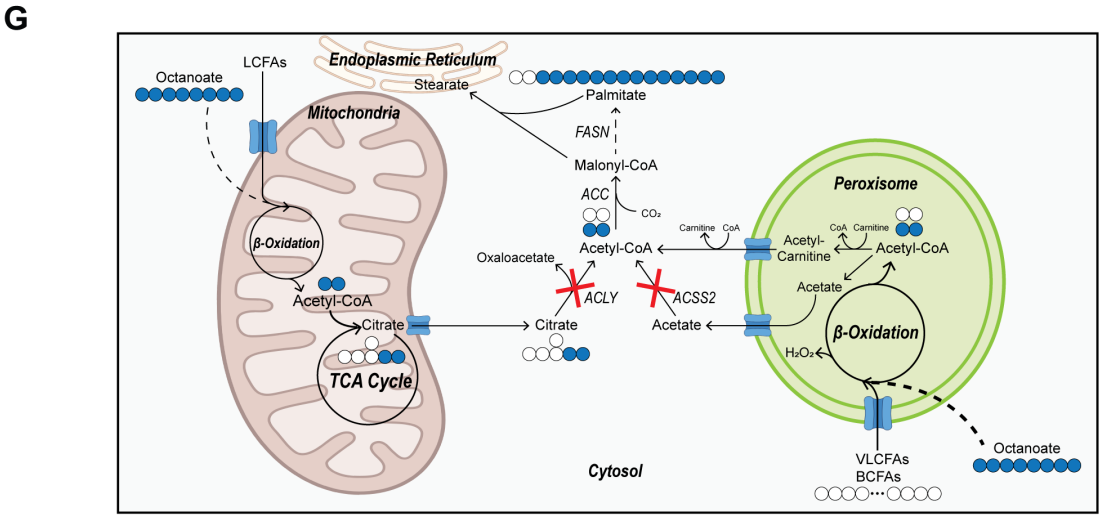
G
Octanoate
LCFAs
Endoplasmic Reticulum
Stearate
Palmitate
FASN
Malonyl-CoA
ACC
CO2
Mitochondria
β-Oxidation
Acetyl-CoA
Citrate
TCA Cycle
Oxaloacetate
ACLY
ACSS2
Acetate
Peroxisome
Carnitine
CoA
Acetyl-Carnitine
H2O2
Cytosol
VLCFAs
BCFAs

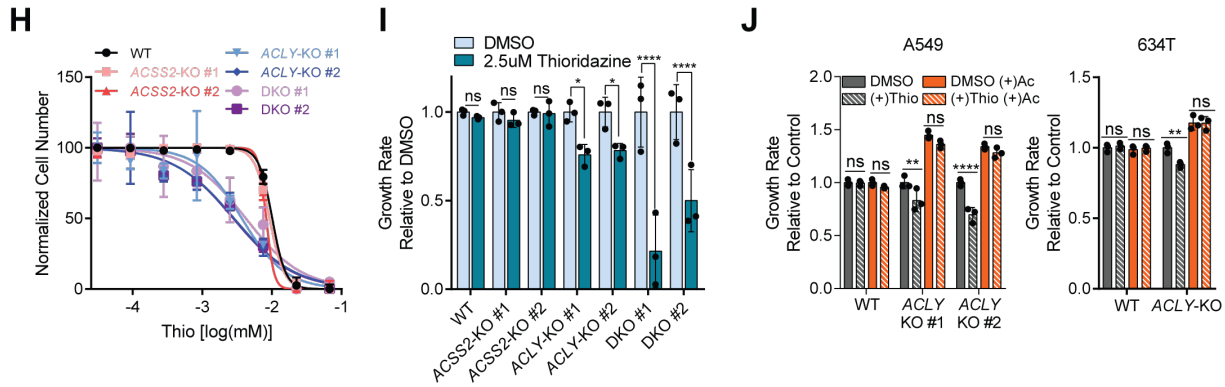
H
Normalized Cell Number
Thio [log(mM)]
I
DMSO
2.5uM Thioridazine
Growth Rate Relative to DMSO
J
A549
634T
DMSO
DMSO (+)Ac
(+)Thio
(+)Thio (+)Ac
Growth Rate Relative to Control
WT
ACLY KO #1
ACLY KO #2
ACLY-KO

3.5 Discussion

Fatty acid biosynthesis is central to the proliferation of cancer cells. Elongation of fatty acid acyl-chains requires provision of two carbon units by cytosolic acetyl-CoA. Here, using metabolic tracing, we elucidate the metabolic reprogramming resulting from inhibition of cytosolic acetyl-CoA synthesis by targeting ACLY and/or ACSS2 in cancer cells with CRISPR/Cas9. Specifically, our study establishes that cancer cells have the capacity to rely on acetate catabolism and ACSS2 for fatty acid synthesis when ACLY is inhibited. Further, cytosolic acetyl-CoA generation and fatty acid biosynthesis were found to be essential to cancer cell proliferation, as knocking out both ACLY and ACSS2 stunted proliferation and *ACLY*-deficiency induced increased reliance on alternative acetyl-CoA generation pathways including *de novo* acetate production and peroxisomal β-oxidation of fatty acids.

Our tracing and proliferation studies confirmed that targeting ACLY with CRISPR/Cas9 reduced *de novo* lipogenesis, reduced cancer cell viability, and increased reliance on extracellular lipids, analogous to the results of previous studies targeting ACLY [20, 25, 26, 55]. ACSS2 expression and acetate utilization were upregulated upon knockout of ACLY, with supplemented acetate becoming the primary lipogenic substrate in multiple *ACLY*-KO cancer cell lines. This finding supports the existence of an ACLY-ACSS2 axis maintaining cytosolic acetyl-CoA synthesis in cancer cells, as previously exhibited in mouse embryonic fibroblast cells [34]. Furthermore, recovery of fatty acid synthesis flux, by acetate addition, rescued growth of *ACLY*-KO cells grown in delipidated media, reinforcing that fatty acid availability, either by synthesis or uptake, is essential to proliferation of cancer cells [7]. These phenotypes were robust across cell types and p53 status (p53-wt: A549, HepG2, p53-null: 634T). ACSS2 knockout reduced acetate catabolism and the magnitude of reduction correlated with expression of other ACSS family enzymes. Fatty acid synthesis was not disrupted with *ACSS2*-deficiency in the tested cells, however growth in delipidated media was reduced in HepG2 *ACSS2*-KO cells. This could be due to altered acetate

shuttling as a result of ACSS1/3 activity which may modify histone acetylation, as has been observed in *ACSS2*-KO cells grown in metabolically stressful conditions previously [46]. The impact of ACSS isozyme expression on acetate shuttling, fatty acid synthesis and epigenetic regulation warrants further study as it may provide insight into how therapeutic interventions targeting acetate catabolism impact whole body physiology.

To date, the only lipogenic acetyl-CoA synthesis mechanisms active in cancer cells were thought to exclusively involve ACLY and ACSS2. We provide evidence that cancer cells utilize alternative acetyl-CoA synthesis pathways when canonical sources are obstructed. Our results suggest that *ACLY*-KO cells produce *de novo* acetate for lipogenic acetyl-CoA synthesis, potentially utilizing a mechanism described previously [48]. However, flux through this pathway was insufficient to sustain DNL and proliferation of *ACLY*-KO cells in the absence of media lipids. When both ACLY and ACSS2 were compromised, palmitate synthesis from canonical lipogenic sources as well as acetate ceased. *ACLY/ACSS2*-DKO cells grew poorly compared to the single *ACLY*-KO cells regardless of media composition, however their continued proliferation suggested additional acetyl-CoA synthesis modalities. We found that peroxisomal fatty acid oxidation provides a significant source of lipogenic acetyl-CoA in *ACLY*-deficient cancer cells. Additionally, *ACLY*-deficiency altered acyl-chain composition of lipids, with depletion of VLCFAs across multiple lipids classes and accumulation of peroxisome derived ether lipids. Furthermore, inhibition of peroxisomal β-oxidation selectively reduced proliferation of ACLY and ACLY/ACSS2 deficient cells. Presumably, this peroxisomal β-oxidation derived acetyl-CoA may also provide acyl units for histone acetylation as well as impact intracellular signaling cascades, as has been observed previously [56]. Thus, disruption of cytosolic acetyl-CoA synthesis rewires *de novo* lipogenesis and makes cancer cells vulnerable to therapeutic intervention.

Notably, our studies were performed exclusively *in vitro* and utilized engineered cell lines with complete genetic ablation of acetyl-CoA synthesis enzymes, while therapeutic intervention is likely to only partially restrain enzyme activity. Additionally, resistance to metabolic therapies

due to redundancies in pathway architecture has reduced efficacy of drugs targeting metabolic enzymes in the past. As such, our results should motivate further investigation into the impacts of inhibition of DNL and DNL feeding enzymes on tumor biology. Ideally such studies would be performed in a more physiological model system which could provide greater context in terms of the impacts on whole body lipid physiology as well as DNL adjacent processes including cholesterol metabolism and epigenetic regulation via histone acetylation. Collectively, our study demonstrates that cytosolic acetyl-CoA synthesis and *de novo* lipogenesis have multiple layers of redundancy and are essential for cancer cell proliferation.

3.6 Acknowledgements

We thank all members of the Metallo laboratory for support and helpful discussions. This study was supported, in part, by US National Institutes of Health (NIH) grants R01CA234245 (C.M.M.).

Chapter 3, in full, is currently being prepared for submission for publication. Avi Kumar is the primary author of this publication. Ramya Kuna, Hector Galvez, Grace H. McGregor, Courtney R. Green, Thekla Cordes, Reuben J. Shaw, Robert U. Svensson are co-authors on the paper. Christian M. Metallo is the corresponding author of this publication.

3.7 References

1. Menendez, J. A. & Lupu, R. Fatty acid synthase and the lipogenic phenotype in cancer pathogenesis. *Nature Reviews Cancer* **7** (2007).

2. Cai, Y., Crowther, J., Pastor, T., Dehairs, J., Swinnen, V. J. & Sablina, A. A. Loss of Chromosome 8p Governs Tumor Progression and Drug Response by Altering Lipid Metabolism Article Loss of Chromosome 8p Governs Tumor Progression and Drug Response by Altering Lipid Metabolism. *Cancer Cell* **29,** 751–766 (2016).

3. Knobloch, M., Braun, S. M. G., Zurkirchen, L., Schoultz, V. C., Zamboni, N., Arauzo-bravo, M. J., Kovacs, W. J., Karalay, Ö., Machado, R. A. C., Roccio, M., Lutolf, M. P., Semenkovich, C. F. & Jessberger, S. Metabolic control of adult neural stem cell activity by Fasn-dependent lipogenesis. *Nature* **493,** 226–230 (2014).

4. Loftus, T. M., Jaworsky, D. E., Frehywot, G. L., Townsend, C. A., Ronnett, V. G., Lane, M. D. & Kuhajda, F. P. Reduced Food Intake and Body Weight in Mice Treated with Fatty Acid Synthase Inhibitors. *Science* **288,** 2379–2382 (2000).

5. Menendez, J. A., Vellon, L., Mehmi, I., Oza, B. P., Ropero, S., Colomer, R. & Lupu, R. Inhibition of fatty acid synthase (FAS) suppresses HER2/neu (erbB-2) oncogene overexpression in cancer cells. *Proceedings of the National Academy of Sciences* **101,** 10715–10720 (2004).

6. Pizer, E. S., Thupari, J., Han, W. F., Pinn, M. L., Chrest, F. J., Frehywot, G. L., Townsend, C. A. & Kuhajda, F. P. Malonyl-Coenzyme-A Is a Potential Mediator of Cytotoxicity Induced by Fatty-Acid Synthase Inhibition in Human Breast Cancer Cells and Xenografts 1. *Cancer Research* **60,** 213–218 (2000).

7. Svensson, R., Parker, S., Eichner, L., Kolar, M., Wallace, M., Brun, S., Lombardo, P., Nostrand, J., Hutchins, A., Vera, L., Gerken, L., Greenwood, J., Bhat, S., Harriman, G., Westlin, W., Jr, H., Saghatelian, A., Kapeller, R., Metallo, C. & Shaw, R. Inhibition of acetyl-CoA carboxylase suppresses fatty acid synthesis and tumor growth of non-small-cell lung cancer in preclinical models. *Nat Med* (2016).

8. Lee, V. J., Carrer, A., Shah, S., Snyder, N. W., Wei, S., Venneti, S., Worth, A. J., Yuan, Z. F., Lim, H. W., Liu, S., Jackson, E., Aiello, N. M., Haas, N. B., Rebbeck, T. R., Judkins, A., Won, K. J., Chodosh, L. A., Garcia, B. A., Stanger, B. Z., Feldman, M. D., Blair, I. A. & Wellen, K. E. Akt-dependent metabolic reprogramming regulates tumor cell Histone acetylation. *Cell Metabolism* **20,** 306–319 (2014).

9. Sivanand, S., Rhoades, S., Jiang, Q., Lee, V. J., Benci, J., Zhang, J., Yuan, S., Viney, I., Zhao, S., Carrer, A., Bennett, M. J., Minn, A. J., Weljie, A. M., Greenberg, R. A. & Wellen, K. E. Nuclear Acetyl-CoA Production by ACLY Promotes Homologous Recombination. *Molecular Cell* **67,** 252–265.e6 (2017).

10. Wellen, K. E., Hatzivassiliou, G., Sachdeva, U. M., Bui, V. T., Cross, J. R. & Thompson, C. B. ATP-Citrate Lyase Links Cellular Metabolism to Histone Acetylation. *Science* **324,** 1076–1080 (2009).

11. Beckner, M. E., Fellows-Mayle, W., Zhang, Z., Agostino, N. R., Kant, J. A., Day, B. W. & Pollack, I. F. Identification of ATP Citrate Lyase as a Positive Regulator of Glycolytic Function in Glioblastomas. *International Journal of Cancer* **126,** 2282–2295 (2011).

12. Migita, T., Narita, T., Nomura, K., Miyagi, E., Inazuka, F., Matsuura, M., Ushijima, M., Mashima, T., Seimiya, H., Satoh, Y., Okumura, S., Nakagawa, K. & Ishikawa, Y. ATP Citrate Lyase : Activation and Therapeutic Implications in Non – Small Cell Lung Cancer. *Cancer Research* **68,** 8547–8555 (2008).

13. Pope, E. D., Kimbrough, E. O., Vemireddy, L. P., Surapaneni, P. K., Copland, J. A. & Mody, K. Aberrant lipid metabolism as a therapeutic target in liver cancer. *Expert Opinion on Therapeutic Targets* **23,** 473–483 (2019).

14. Turyn, J., Schlichtholz, B., Dettlaff-Pokora, A., Presler, M., Goyke, E., Matuszewski, M., Kmieć, Z., Krajka, K. & Swierczynski, J. Increased Activity of Glycerol 3-phosphate Dehydrogenase and Other Lipogenic Enzymes in Human Bladder Cancer. *Hormone and Metabolic Research* **35,** 565–569 (2003).

15. Varis, A., Wolf, M., Monni, O., Vakkari, M.-l., Kokkola, A., Moskaluk, C., Frierson, H., Powell, S. M., Knuutila, S., Kallioniemi, A. & El-rifai, W. Targets of Gene Amplification and Overexpression at 17q in Gastric Cancer 1. *Cancer Research* **62,** 2625–2629 (2002).

16. Yancy, H. F., Mason, J. A., Peters, S., Iii, C. E. T., Littleton, G. K., Jett, M. & Day, A. A. Metastatic progression and gene expression between breast cancer cell lines from African American and Caucasian women. *Journal of Carcinogenesis* **6** (2007).

17. Zhou, Y., Bollu, L. R., Tozzi, F., Ye, X., Bhattacharya, R., Gao, G., Dupre, E., Xia, L., Lu, J., Fan, F., Bellister, S., Ellis, L. M. & Weihua, Z. ATP citrate lyase mediates resistance of colorectal cancer cells to SN38. *Molecular Cancer Therapeutics* **12,** 2782–2791 (2013).

18. Qian, X., Hu, J., Zhao, J. & Chen, H. ATP citrate lyase expression is associated with advanced stage and prognosis in gastric adenocarcinoma. *International Journal of Clinical and Experimental Medicine* **8,** 7855–7860 (2015).

19. Bauer, D. E., Hatzivassiliou, G., Zhao, F., Andreadis, C. & Thompson, C. B. ATP citrate lyase is an important component of cell growth and transformation. *Oncogene* **24,** 6314–6322 (2005).

20. Hatzivassiliou, G., Zhao, F., Bauer, D. E., Andreadis, C., Shaw, A. N., Dhanak, D., Hingorani, S. R., Tuveson, D. A. & Thompson, C. B. ATP citrate lyase inhibition can suppress tumor cell growth. *Cancer Cell* **8,** 311–321 (2005).

21. Lowenstein, J. M. Effect of (-)Hydroxycitrate on Fatty Acid Synthesis by Rat Liver in Vivo. *Journal of Biological Chemistry* **246,** 629–632 (1971).

22. Lucenay, K. S., Doostan, I., Karakas, C., Bui, T., Ding, Z., Mills, G. B., Hunt, K. K. & Keyomarsi, K. Cyclin E Associates with the Lipogenic Enzyme ATP-Citrate Lyase to Enable Malignant Growth of Breast Cancer Cells. *Cancer Research* **76,** 2406–2419 (2016).

23. Pinkosky, S. L., Filippov, S., Srivastava, R. A. K., Hanselman, J. C., Bradshaw, C. D., Hurley, T. R., Cramer, C. T., Spahr, M. A., Brant, A. F., Houghton, J. L., Baker, C., Naples, M., Adeli, K. & Newton, R. S. AMP-activated protein kinase and ATP-citrate lyase are two distinct molecular targets for ETC-1002 , a novel small molecule regulator of lipid and carbohydrate metabolism. *Journal of Lipid Research* **54** (2013).

24. Sullivan, C., Hamilton, J. G., Wheatley, R., River, C. & Laboratories, B. Inhibition of Lipogenesis in Rat Liver by (-)Hydroxycitrate. *Archives of Biochemistry and Biophysics* **150,** 183–190 (1972).

25. Wang, D., Yin, L., Wei, J. & Yang, Z. ATP citrate lyase is increased in human breast cancer , depletion of which promotes apoptosis. *Tumor Biology* (2017).

26. Zaidi, N., Royaux, I., Swinnen, V. J. & Smans, K. ATP Citrate Lyase Knockdown Induces Growth Arrest and Apoptosis through Different Cell- and Environment- Dependent Mechanisms. *Molecular Cancer Therapeutics* **11,** 1925–1936 (2012).

27. Luong, A., Hannah, V. C., Brown, M. S. & Goldstein, J. L. Molecular characterization of human acetyl-CoA synthetase, an enzyme regulated by sterol regulatory element-binding proteins. *Journal of Biological Chemistry* **275,** 26458–26466 (2000).

28. Schug, Z. T., Voorde, V. J. & Gottlieb, E. The metabolic fate of acetate in cancer. *Nature Publishing Group* **16,** 708–717 (2016).

29. Fujino, T., Kondo, J., Ishikawa, M., Morikawa, K. & Yamamoto, T. T. Acetyl-CoA Synthetase 2, a Mitochondrial Matrix Enzyme Involved in the Oxidation of Acetate. *Journal of Biological Chemistry* **276,** 11420–11426 (2001).

30. Comerford, S. A., Huang, Z., Du, X., Wang, Y., Cai, L., Witkiewicz, A. K., Walters, H., Tantawy, M. N., Fu, A., Manning, H. C., Horton, J. D., Hammer, R. E., Mcknight, S. L. & Tu, B. P. Acetate dependence of tumors. *Cell* **159,** 1591–1602 (2014).

31. Schug, Z. T., Peck, B., Jones, D. T., Zhang, Q., Grosskurth, S., Alam, I. S., Goodwin, L. M., Smethurst, E., Mason, S., Blyth, K., McGarry, L., James, D., Shanks, E., Kalna, G., Saunders, R. E., Jiang, M., Howell, M., Lassailly, F., Thin, M. Z., Spencer-Dene, B., Stamp, G., van den Broek, N. J., Mackay, G., Bulusu, V., Kamphorst, J. J., Tardito, S., Strachan, D., Harris, A. L., Aboagye, E. O., Critchlow, S. E., Wakelam, M. J., Schulze, A. & Gottlieb, E. Acetyl-CoA synthetase 2 promotes acetate utilization and maintains cancer cell growth under metabolic stress. *Cancer Cell* **27,** 57–71 (2015).

32. Xu, M., Nagati, J. S., Xie, J., Li, J., Walters, H., Moon, Y.-a., Gerard, R. D., Huang, C.-l., Comerford, S. A., Hammer, R. E., Horton, J. D., Chen, R. & Garcia, J. A. An acetate switch regulates stress erythropoiesis. *Nature Medicine* **20** (2014).

33. Kamphorst, J. J., Chung, M. K., Fan, J. & Rabinowitz, J. D. Quantitative analysis of acetyl-CoA production in hypoxic cancer cells reveals substantial contribution from acetate. *Cancer & Metabolism* **2,** 23 (2014).

34. Zhao, S., Torres, A. M., Henry, R. A., Trefely, S., Wallace, M., Lee, V. J., Carrer, A., Sengupta, A., Campbell, S. L., Kuo, Y. M., Frey, A. J., Meurs, N., Viola, J. M., Blair, I. A., Weljie, A. M., Metallo, C. M., Snyder, N. W., Andrews, A. J. & Wellen, K. E. ATP-Citrate Lyase Controls a Glucose-to-Acetate Metabolic Switch. *Cell Reports* **17,** 1037–1052 (2016).

35. Bian, F., Kasumov, T., Thomas, K. K., Jobbins, K. A., David, F., Minkler, P. E., Hoppel, C. L. & Brunengraber, H. Peroxisomal and mitochondrial oxidation of fatty acids in the heart, assessed from the 13C labeling of malonyl-CoA and the acetyl moiety of citrate. *Journal of Biological Chemistry* **280,** 9265–9271 (2005).

36. Kasumov, T., Adams, J. E., Bian, F., David, F., Thomas, K. R., Jobbins, K. A., Minkler, P. E., Hoppel, C. L. & Brunengraber, H. Probing peroxisomal β-oxidation and the labelling of acetyl-CoA proxies with [1-13C]octanoate and [3-13C]octanoate in the perfused rat liver. *Biochemical Journal* **389,** 397–401 (2005).

37. Reszko, A. E., Kasumov, T., David, F., Jobbins, K. A., Thomas, K. R., Hoppel, C. L., Brunengraber, H. & Des Rosiers, C. Peroxisomal Fatty Acid Oxidation Is a Substantial Source of the Acetyl Moiety of Malonyl-CoA in Rat Heart. *Journal of Biological Chemistry* **279,** 19574–19579 (2004).

38. Zha, S., Ferdinandusse, S., Hicks, J. L., Denis, S., Dunn, T. A., Wanders, R. J., Luo, J., De Marzo, A. M. & Isaacs, W. B. Peroxisomal branched chain fatty acid β-oxidation pathway is upregulated in prostate cancer. *Prostate* **63,** 316–323 (2005).

39. Ran, F. A., Hsu, P. D., Wright, J., Agarwala, V., Scott, D. A. & Zhang, F. Genome engineering using the CRISPR-Cas9 system. *Nature Protocols* **8,** 2281–2308 (2013).

40. Sanjana, N., Shalem, O. & Zhang, F. Improved vectors and genome-wide libraries for CRISPR screening. *Nat Methods* **11,** nmeth.3047 (2014).

41. Kumar, A., Mitchener, J., King, Z. A. & Metallo, C. M. Escher-Trace: A web application for pathway-based visualization of stable isotope tracing data. *BMC Bioinformatics* **21,** 1–10 (2020).

42. Jiang, L., Shestov, A. A., Swain, P., Yang, C., Parker, S. J., Wang, Q. A., Terada, L. S., Adams, N. D., Mccabe, M. T., Pietrak, B., Schmidt, S., Metallo, C. M., Dranka, B. P., Schwartz, B. & Deberardinis, R. J. Reductive carboxylation supports redox homeostasis during anchorage-independent growth. *Nature* **532,** 255–258 (2016).

43. Son, J., Lyssiotis, C. A., Ying, H., Wang, X., Hua, S., Ligorio, M., Perera, R. M., Ferrone, C. R., Mullarky, E., Shyh-Chang, N., Kang, Y., Fleming, J. B., Bardeesy, N., Asara, J. M., Haigis, M. C., Depinho, R. A., Cantley, L. C. & Kimmelman, A. C. Glutamine supports pancreatic cancer growth through a KRAS-regulated metabolic pathway. *Nature* **496,** 101–105 (2013).

44. Jiang, L., Boufersaoui, A., Yang, C., Ko, B., Rakheja, D., Guevara, G., Hu, Z. & DeBerardinis, R. J. Quantitative metabolic flux analysis reveals an unconventional pathway of fatty acid synthesis in cancer cells deficient for the mitochondrial citrate transport protein. *Metabolic Engineering* **43,** 198–207 (2016).

45. Jiang, L., Boufersaoui, A., Yang, C., Ko, B., Rakheja, D., Guevara, G., Hu, Z. & DeBerardinis, R. J. Quantitative metabolic flux analysis reveals an unconventional pathway of fatty acid synthesis in cancer cells deficient for the mitochondrial citrate transport protein. *Metabolic Engineering* **43,** 198–207 (2017).

46. Gao, X., Lin, S.-h., Ren, F., Li, J.-t., Chen, J.-j., Yao, C.-b., Yang, H.-b., Jiang, S.-x., Yan, G.-q., Wang, D., Wang, Y., Liu, Y., Cai, Z., Xu, Y.-y., Chen, J., Yu, W., Yang, P.-y. & Lei, Q.-y. Acetate functions as an epigenetic metabolite to promote lipid synthesis under hypoxia. *Nature Communications* **7,** 1–14 (2016).

47. Wallace, M., Green, C., Roberts, L., Lee, Y., Justin, M., Joan, S., Meurs, N., Gengatharan, J., Hover, J., Phillips, S., Ciaraldi, T., Guertin, D., Cabrales, P., Ayres, J., Nomura, D., Loomba, R. & Metallo, C. Enzyme promiscuity drives branched-chain fatty acid synthesis in adipose tissues. *Nat Chem Biol* **14,** 1021 (2018).

48. Liu, X., Cooper, D. E., Cluntun, A. A., Warmoes, M. O., Zhao, S., Reid, M. A., Liu, J., Lund, P. J., Lopes, M., Garcia, B. A., Wellen, K. E., Kirsch, D. G. & Locasale, J. W. Acetate Production from Glucose and Coupling to Mitochondrial Metabolism in Mammals. *Cell* **175,** 502–513.e13 (2018).

49. Lodhi, I. J. & Semenkovich, C. F. Peroxisomes: a nexus for lipid metabolism and cellular signaling. *Cell Metab.* **19,** 380–92 (2014).

50. Jakobs, B. S. & Wanders, R. J. Fatty acid β-oxidation in peroxisomes and mitochondria: The first, unequivocal evidence for the involvement of carnitine in shuttling propionyl-CoA from peroxisomes to mitochondria. *Biochemical and Biophysical Research Communications* **213,** 1035–1041 (1995).

51. Leighton, F., Bergseth, S., Rortveit, T., Christiansen, E. N. & Bremer, J. Free acetate production by rat hepatocytes during peroxisomal fatty acid and dicarboxylic acid oxidation. *Journal of Biological Chemistry* **264,** 10347–10350 (1989).

52. Wanders, R., Waterham, H. & Ferdinandusse, S. Metabolic Interplay between Peroxisomes and Other Subcellular Organelles Including Mitochondria and the Endoplasmic Reticulum. *Frontiers Cell Dev Biology* **3,** 83 (2016).

53. Van den Branden, C. & Roels, F. Thioridazine: a selective inhibitor of peroxisomal β-oxidation in vivo. *FEBS Letters* **187,** 331–333 (1985).

54. Shi, R., Zhang, Y., Shi, Y., Shi, S. & Jiang, L. Inhibition of peroxisomal β-oxidation by thioridazine increases the amount of VLCFAs and Aβ generation in the rat brain. *Neuroscience Letters* **528,** 6–10 (2012).

55. Carrer, A., Trefely, S., Zhao, S., Campbell, S. L., Norgard, R. J., Schultz, K. C., Sidoli, S., Parris, J. L., Affronti, H. C., Sivanand, S., Egolf, S., Sela, Y., Trizzino, M., Gardini, A., Garcia, B. A., Snyder, N. W., Stanger, B. Z. & Wellen, K. E. Acetyl-CoA metabolism supports multistep pancreatic tumorigenesis. *Cancer Discovery* **9,** 416–435 (2019).

56. He, A., Chen, X., Tan, M., Chen, Y., Lu, D., Zhang, X., Dean, J. M., Razani, B. & Lodhi, I. J. Acetyl-CoA Derived from Hepatic Peroxisomal β-Oxidation Inhibits Autophagy and Promotes Steatosis via mTORC1 Activation. *Molecular Cell* **79,** 30–42.e4 (2020).

Chapter 4

Escher-Trace: a web application for pathway-based visualization of stable isotope tracing data

4.1 Abstract

Background: Stable isotope tracing has become an invaluable tool for probing the metabolism of biological systems. However, data analysis and visualization from metabolic tracing studies often involve multiple software packages and lack pathway architecture. A deep understanding of the metabolic contexts from such datasets is required for biological interpretation. Currently, there is no single software package that allows researchers to analyze and integrate stable isotope tracing data into annotated or custom-built metabolic networks. Results: We built a standalone web-based software, Escher-Trace, for analyzing tracing data and communicating results. Escher-Trace allows users to upload baseline corrected mass spectrometer (MS) tracing data and correct for natural isotope abundance, generate publication quality graphs of metabolite labeling, and present data in the context of annotated metabolic pathways. Here we provide a

detailed walk-through of how to incorporate and visualize 13C metabolic tracing data into the Escher-Trace platform. Conclusions: Escher-Trace is an open-source software for analysis and interpretation of stable isotope tracing data and is available at https://escher-trace.github.io/.

4.2 Background

Metabolism plays a central role in all areas of biology. Metabolic reprogramming at the cellular level has been implicated in numerous diseases ranging from diabetes[1, 2] to cancer[3, 4]. Understanding metabolic phenotypes involves not only analyzing metabolite abundances (i.e., metabolomics) but also changes in metabolic pathway activity or flux. Stable isotope tracing studies are an effective method for investigating intracellular metabolic fluxes[5, 6] that have been increasingly used in the last decade[7]. Insight into pathway activity can be gleaned by applying a stable isotope labeled metabolite to a cell or in vivo system and evaluating where the heavy isotopes are transferred. In recent years, tracing studies have been critical for identifying alterations in tricarboxylic acid[8, 9], serine[10], branched chain amino acids[11, 12], and NAD(P)H metabolism[13–15] in a variety of cell and organ systems. Stable isotope tracing experiments utilizing a single tracer and nominal resolution GC-MS analytics in particular have become widely adopted due to their reliability, low cost, and the wealth of information they can provide.

Tracing data sets are initially presented in large data tables which contain the labeling patterns (i.e. isotopologue or mass isotopomer distributions) of all measured compounds in each sample. Interpreting such datasets is best accomplished in the context of metabolic networks and each metabolite's location within metabolic pathways. Additionally, proper reporting of data requires extensive plotting of results, which can be normalized and presented in various ways. The discovery process, which is typically iterative, can be extremely time consuming when dealing with many metabolites or samples. As such, a data visualization platform where isotopologue

distributions and related data can be presented graphically in the context of metabolic networks would be very beneficial to the research community. Such a platform would contextualize the data and remove tedious intermediary steps allowing researchers to better focus on validating and interpreting the meaning of their results.

Although numerous software packages are available to analyze metabolomics data, few include capabilities for interpreting stable isotope labeling. XCMS[16], OPENMS[17], as well as vendor-specific software packages allow for integration of mass spectrometry data to quantify metabolite abundances but do not provide options for analyzing metabolite labeling. IsoMetlin[18] allows for identification of isotopically labeled compounds from MS and MS/MS spectra, while software packages such as IsoCor[19]. ICT [20], ElemCor[21], and IsoCorrectoR[22] allow users to correct isotopic labeling for natural isotope abundance. MAVEN allows for quantitation of high-resolution metabolite labeling as well as natural isotope correction but is not designed for widely available GC-MS systems [23]. Metaboanalyst[24] and Omix[25] allow for visualization of metabolomic and fluxomic datasets in the context of a network but do not provide options for processing or overlaying tracing data. As a result, scientists running tracing studies are required to use multiple software packages to correct their data for natural isotope abundance, perform analysis, prepare figures, and communicate their results.

The most effective way to understand data from tracing experiments is to view metabolite labeling patterns, enrichments, and abundances together on top of a metabolic map. Escher-Trace fills this need by allowing users to overlay multiple types of tracing data on top of Escher metabolic network maps. The software has an interactive, user-friendly, graphical user interface, has a low entry level (i.e. is accessible to users with little tracing experience), and is specifically catered toward users running single tracer studies with GC-MS analytics. Escher-Trace enables users to correct for natural isotope abundance, generate publication quality graphs of metabolite labeling, and present data in the context of pathways. Escher is compatible with BiGG Models[26], providing access to a set of metabolic maps, and the Escher platform provides a comprehensive

library of metabolites and metabolic reactions that can be used to seamlessly generate new maps. The ability to generate graphs of multiple data types and compatibility with Escher make Escher-Trace a powerful tool for analyzing and visualizing tracing datasets. We walk through a specific use case of how one can employ Escher-Trace to analyze a stable isotope traced data set and generate a figure summarizing the primary findings of the experiment.

4.3 Implementation

Escher-Trace is built on top of the Escher[27] interface, a web based metabolic pathway visualization platform, using javascript and the D3.js library. Escher-Trace allows users to upload stable isotope labeled metabolomic data sets into Escher by clicking the "Import Tracing Data" button in the bottom right hand corner of the screen. Data files can be uploaded in CSV format as either baseline corrected (Additional File 1) or both baseline and natural isotope abundance corrected mass spectrometer counts (Additional File 2) or alternatively in JSON format if reloading a prior Escher-Trace workspace. The required format of uploaded data is specified in the user documentation (https://escher-trace.readthedocs.io/). If uploading data that is not corrected for natural isotope abundance, the user will be asked to indicate which type of tracer was used in their data set (e.g. 13C, 15N, 2H). When uploading data for the first time, the user will be instructed to organize their samples into groups based on experimental conditions. Sample data within the same group will be averaged together and presented with standard deviation in graphs. Data sets with over one hundred samples organized into over forty groups have successfully been uploaded to the tool. However, the largest default color scheme in Escher-Trace contains fifteen color entries, if more groups are included, the user can create and utilize larger color schemes by selecting **Graph Attribute** $\rightarrow$ **Color Scheme** from the Escher-Trace menu, additional instruction can be found in the user documentation. After organizing sample data files into groups, isotopologue distributions which correspond

to metabolites included in the Escher map will be displayed next to the corresponding Escher metabolite node. Data is mapped by connecting the BiGG IDs of metabolites entered by the user to the corresponding Escher nodes. BiGG IDs are standardized identifiers of metabolites included in the BiGG Models database[26], which allows for the connection of Escher map nodes to genome scale metabolic models and external databases such as KEGG[28] and BioCyc[29]. All unmapped metabolite data is displayed on the left-hand side of the map. Data that is uncorrected for natural isotope abundance is corrected using the user selected tracer type, metabolite formula, actual measurements, natural stable isotope enrichment information, and the algorithm presented by Fernandez et. al[30]. Matrix calculations are performed using functions from the math.js library. The correction algorithm used by Escher-Trace is best suited to correct small molecule metabolite data generated by a nominal resolution mass spectrometer. Data which does not fit these conditions can still be visualized in Escher-Trace, but must be corrected first using a separate correction software and uploaded as a corrected csv data file (the format for which can be found in the user documentation). A comparison of results obtained from the correction algorithms of Escher-Trace and IsoCor can be found in Additional File 3. Escher-Trace can visualize metabolite isotope labeling, enrichment, and abundance as single bar or stacked bar plots for steady state labeling studies or as line graphs for time-course/kinetic studies (Fig. 1). Isotopologue distributions are calculated by dividing the abundance of each isotopologue by the sum total of all isotopologues of the metabolite.

The user can interact with their data by two means (1) using the Escher-Trace Menu located on the right-hand side of the screen or (2) right-clicking individual graphs. With the Escher-Trace menu, the user can make changes which affect graphs across the network such as altering data types or metabolites that are visualized, normalizing abundances of metabolites, and saving the Escher-Trace workspace in JSON format. By right-clicking individual graphs, the user can download the selected graph in SVG or PNG format, remove the graph from the map, view the data used to generate the graph, or generate additional graphs relating to the specific

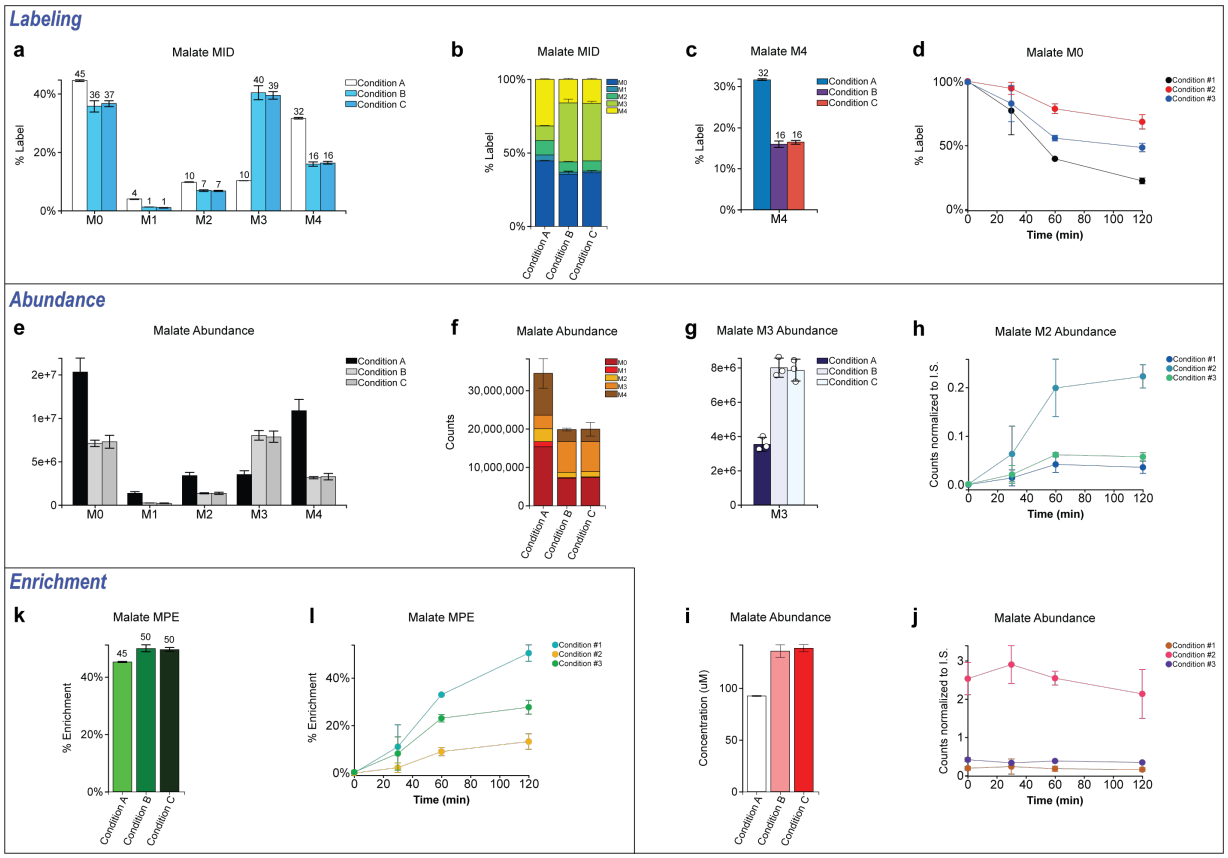

Figure 4.1: **Graph types available in Escher-Trace.** A) Mass isotopomer distribution. B) Stacked mass isotopomer distribution. C) Single isotopologue label. D) Kinetic single isotopologue label*. E) Abundance. F) Stacked abundance. G) Single isotopologue abundance**. H) Kinetic single isotopologue abundance*. I) Quantitative abundance***. J) Kinetic total abundance*. K) Enrichment****. L) Kinetic enrichment* ****. (*) Requires time point information to be input using **Analysis → Enter Time Points** in the Escher-Trace Menu. (**) Shown with individual data points plotted, accessed by setting **Graph Attributes → Plot Individual Values to ON**. (***) Requires quantitative standard information to be input using **Analysis → Enter Quantitative Standards** in the Escher-Trace Menu. (****) Requires element count of tracer of interest to be input using **Data Displayed → Isotopologues to Display** in the Escher-Trace Menu. Note: All data used to make the graphs in this figure was fabricated

metabolite including data for additional fragments.

4.4 Results and Discussion

To demonstrate a typical use case of Escher-Trace, we will analyze data from the Huh7 hepatocellular carcinoma cell line grown with [U-$^{13}C_5$]glutamine in normoxic (21 % oxygen) and hypoxic (1 % oxygen) conditions. Hypoxia induces a classical metabolic reprogramming phenotype in highly proliferative cells[31]. We will walk through how a user might identify reprogramming induced by hypoxia and generate a figure that communicates this phenotype with Escher-Trace.

First, we must upload our raw mass spectrometer counts CSV file (available as Additional file 1) which were analyzed via nominal resolution gas chromatography-mass spectrometry (GC-MS) and integrated with an available MS integration software package. The data is baseline corrected but remains uncorrected for natural isotope abundance, so we upload the CSV file to Escher-Trace as an uncorrected CSV file and select the tracer type as "13C". We organize the sample data files into two distinct groups which are named "Normoxia" and "Hypoxia" to represent each experimental condition. After submitting the sample order, isotopologue distributions of our data appear on top of the Escher map (Fig. 2). At first glance, one can identify that our experimental conditions produce distinct labeling patterns in TCA cycle intermediates.

Upon closer observation of the isotopologue distributions for TCA intermediates, we can identify a unique labeling distribution on citrate. Specifically, we observe increased relative abundance of M5 citrate label (over 6x increased) in hypoxia compared to normoxia (Fig. 3a). The number of isotopologues visualized in Escher-Trace graphs can be adjusted for clarity by selecting **Data Displayed → Isotopologues to Display** from the Escher-Trace menu and reducing the isotopologue limit for the metabolite of interest. Using the metabolic map, we can identify that M5 citrate can only be generated reductively (in the counter-clockwise direction) from

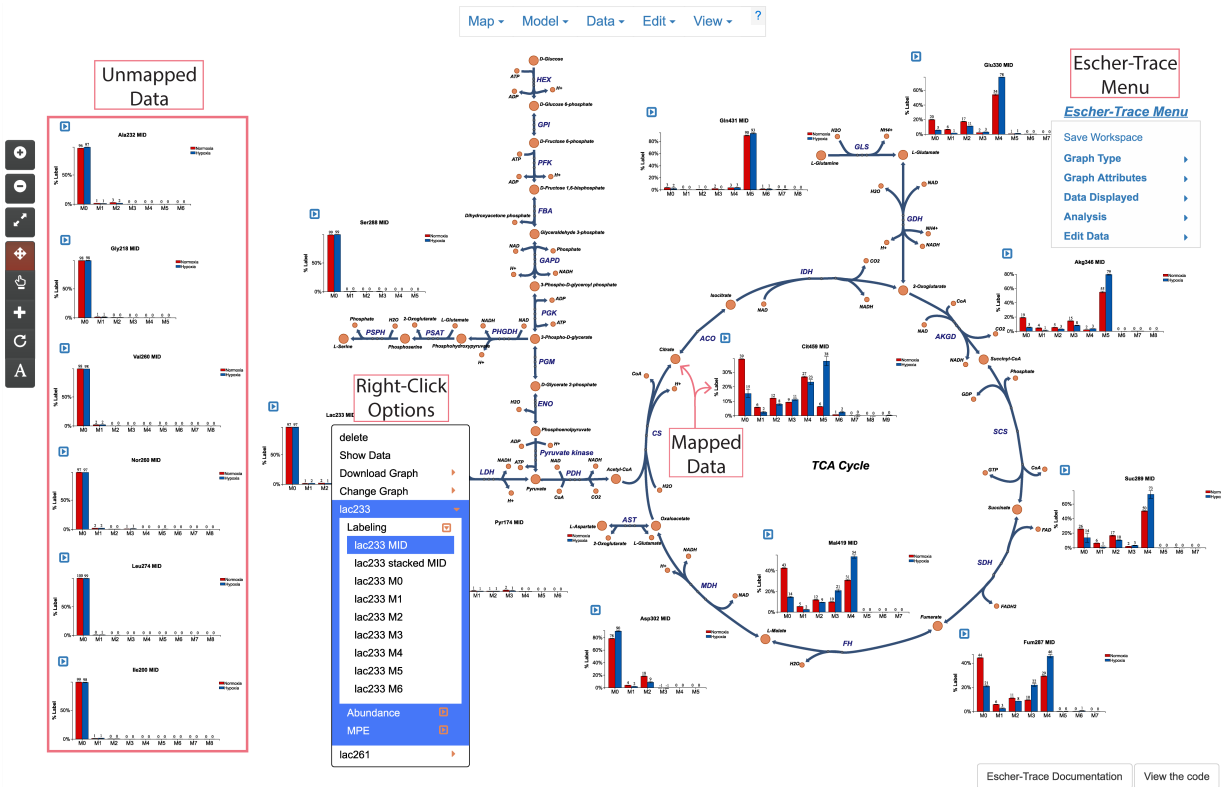

Figure 4.2: **Escher-Trace Interface.** The Escher-Trace menu can be used to cycle through graphs of labeling, abundance, and enrichment, alter graph aesthetics, normalize abundances, reorganize data and data files, save the Escher-Trace workspace and more. Data is mapped to Escher metabolite nodes by BiGG ID. Graphs of unmapped metabolites are included on the left-hand side of the Escher canvas. All graphs can be right-clicked to access additional graph types for the selected metabolite as well as graph specific functions. The Escher menu and all of its functionality related to map editing and data overlay is accessible when using Escher-Trace.

alpha-ketoglutarate (aKG). If aKG is oxidized in the clockwise direction of the TCA cycle, M4 isotopologues of the remaining TCA intermediates will form. This includes M4 citrate which is generated from M4 oxaloacetate and unlabeled mitochondrial acetyl-CoA derived predominantly from unlabeled glucose-derived pyruvate. Increased M5 citrate formation is now known to be demonstrative of upregulated reductive carboxylation flux which has been observed in highly proliferative cells cultured in hypoxia[32].

To get a broader overview of how metabolite abundances are altered between the experimental conditions we select on the Escher-Trace menu **Graph Type → Total Abundance**. This causes all metabolite data to switch from isotopologue distributions to abundances (Fig. 3b). We see that there appears to be a distinct decrease in the raw counts of TCA intermediates in cells under hypoxia. However, to properly analyze how intracellular abundances are impacted by hypoxia, we need to normalize our data based on our experimental workflow. Metabolite abundance normalization is performed by selecting **Analysis → Normalize Abundances** on the Escher-Trace menu. Here a norvaline internal standard was spiked into all samples, so we select nor260, one of the two norvaline fragments we detect with our GC-MS method, for normalization of all metabolites. Additionally, cell count data can be entered to obtain per cell quantitation of metabolites (normoxia: 638333 cells, hypoxia: 668750 cells). We can also optionally select an experimental condition to normalize our data to simplify data presentation; in our case we present data relative to normoxia. After submitting our selections, total abundance graphs are rescaled (Fig. 3c). One can see that the per cell abundances of TCA intermediates are decreased in hypoxic conditions, as previously noted[32].

We can streamline data communication by producing graphs of data across metabolites. These types of graphs can by generated in Escher-Trace by selecting **Analysis → Compare Metabolites** in the Escher-Trace menu. This option allows the user to select metabolites, experimental conditions, and data types (metabolite abundance, enrichment, or individual isotopologue labeling) to include in a bar graph. Using this feature, we generated a summary figure highlighting

increased TCA intermediate enrichment from [U-$^{13}C_5$]glutamine in hypoxia (Fig. 3d).

Finally, to simplify the data presented on the metabolic map, we can select to only display data for metabolites of interest, glycolytic and TCA intermediates in this case, by using **Data Displayed → Metabolites to Display** in the Escher-Trace menu. Figures of additional data types, including individual isotopologue labeling, metabolite abundance, and mole percent enrichment, as well as additional plot types (single or stacked bar plots) can be accessed using the context menu, by **right-clicking** any Escher-Trace graph, selecting a **metabolite fragment**, and then selecting the **data and plot type**. The title and y-axis labels of all graphs can be edited by clicking on them and entering in new text as needed for clarity. Finally, labeling diagrams can be introduced using **Data Displayed → Create Carbon Diagram**, to generate the final figure (Fig. 4) This publication-quality figure can be downloaded as an SVG or PNG file using the Escher menu selecting **Map → Export as SVG or PNG**. Individual graphs can be independently downloaded by **right-clicking** them and selecting **Download → SVG or PNG**. The Escher-Trace workspace itself can be downloaded by selecting **Save Workspace** from the Escher-Trace menu. This workspace file can be sent to collaborators and reloaded in Escher-Trace to communicate findings or perform further analyses.

4.5 Conclusions

Escher-Trace is a web-based software for visualizing and interpreting stable isotope tracing data in the context of a metabolic network. We have shown that Escher-Trace can facilitate calculation and presentation of labeling patterns resulting from alterations in pathway activity (i.e. hypoxia) and overlay results on an Escher pathway map. By providing a tool which allows users to correct for natural isotope abundance, visualize labeling patterns, and generate scientific figures all through a simple graphical user interface, we believe Escher-Trace is a significant addition to the software available to metabolic researchers.

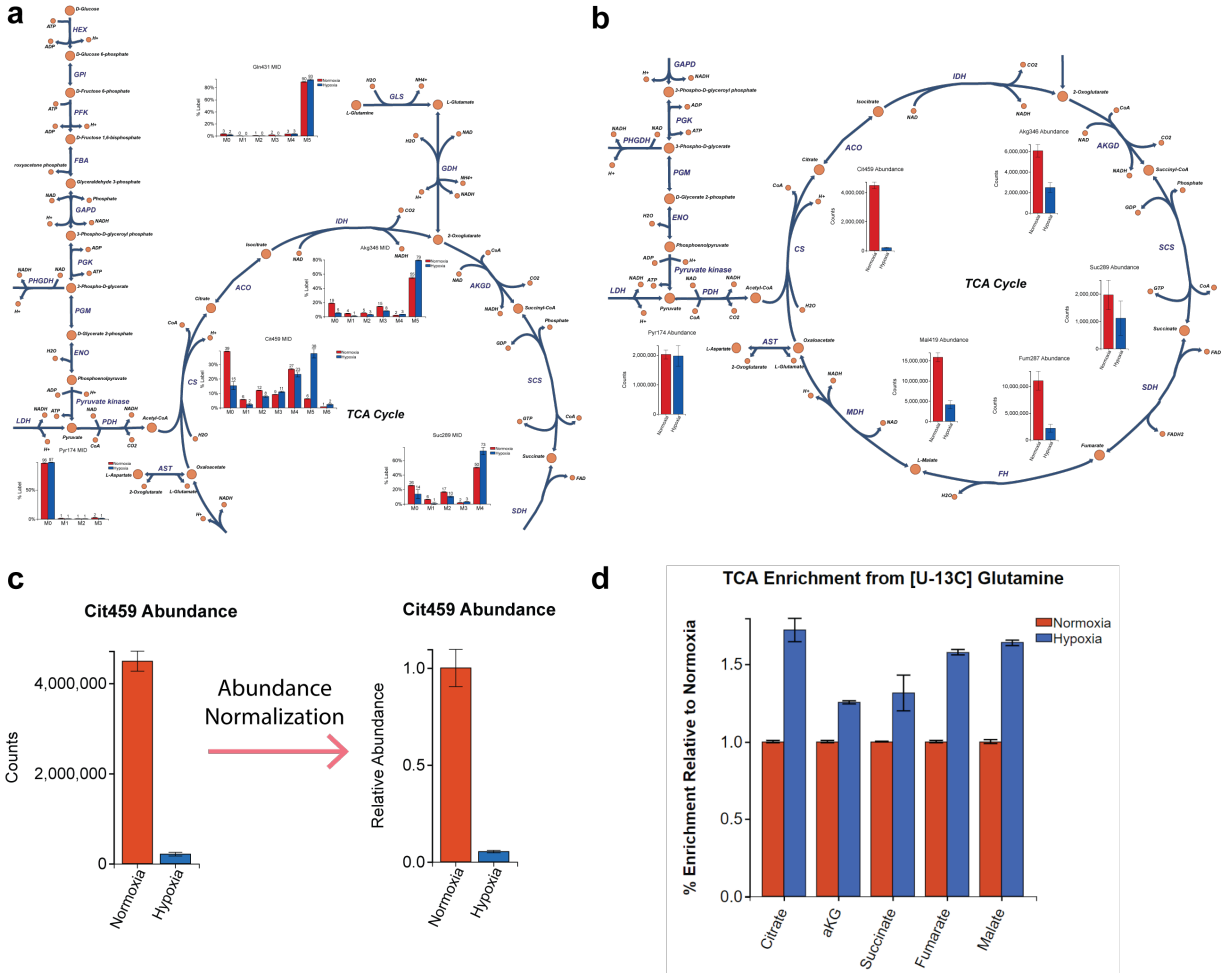

Figure 4.3: **Data Analysis.** A) TCA intermediates labeling from a [U-$^{13}C_5$]Glutamine tracer, generated after the initial submission of data to Escher-Trace. B) TCA intermediate abundance generated by selecting **Graph Type** → **Total Abundance** from the Escher-Trace menu. C) Citrate abundance before and after entry of abundance normalization information via **Analysis** → **Normalize Abundance** from the Escher-Trace menu. D) TCA enrichment from a [U-$^{13}C_5$]Glutamine, generated by selecting **Analysis** → **Compare Metabolites** from the Escher-Trace menu.

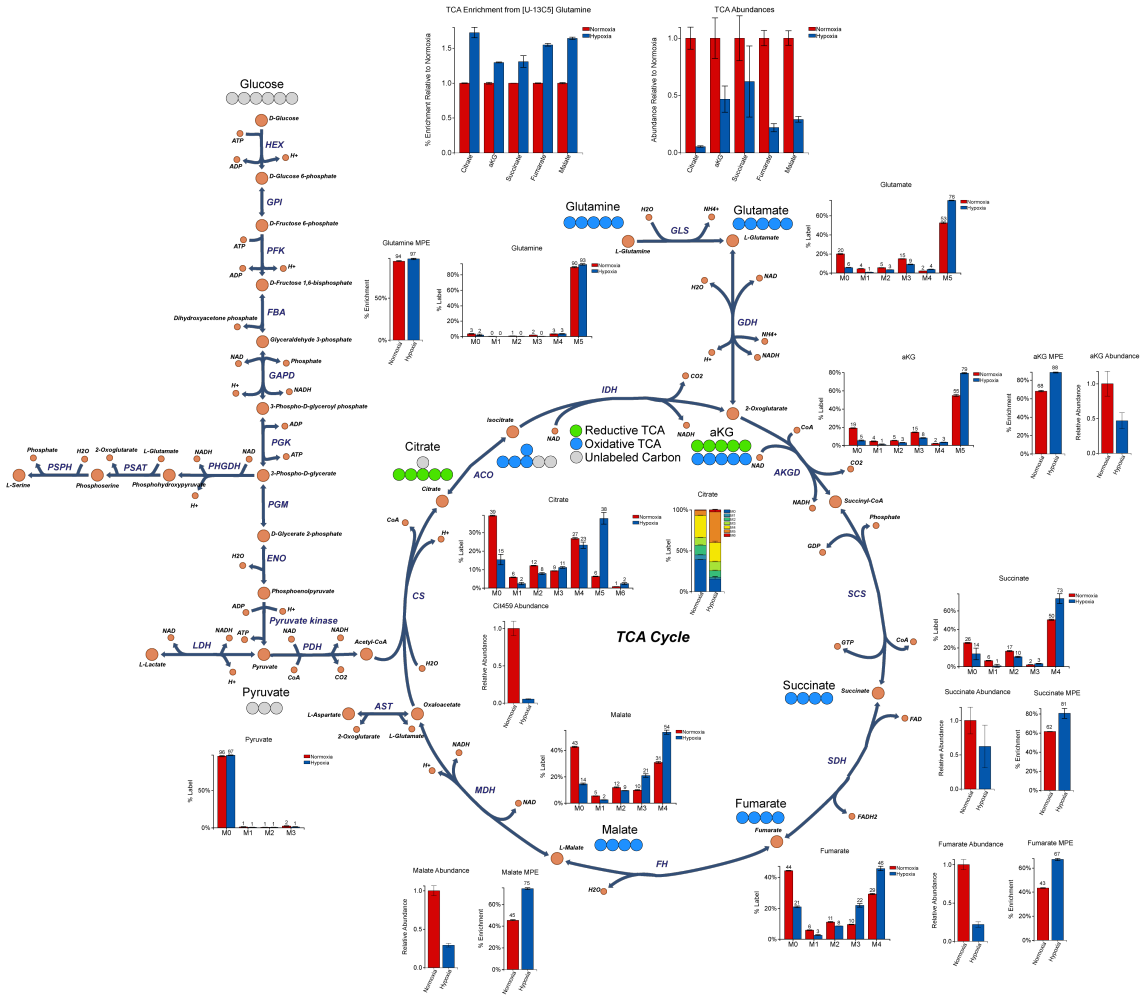

Figure 4.4: **Complete ^{13}C Figure.** A complete ^{13}C data figure showcasing the reprogramming of glutamine catabolism in Huh7 hepatocellular carcinoma cells grown in hypoxia compared to normoxia. Carbon circle diagrams were added by selecting **Data Displayed → Create Carbon Diagram** from the Escher-Trace menu.

4.6 Acknowledgements

We thank all members of the Metallo laboratory for their support and helpful discussions. Support for AK and C.M.M. was provided by NSF CAREER Award #1454425 (C.M.M.). Support for Z.K was provided by the Novo Nordisk Foundation through the Center for Biosustainability at the Technical University of Denmark #NNF10CC1016517 (Z.K.). The funding bodies did not play any roles in the design of the study and collection, analysis, and interpretation of data and in writing the manuscript.

Chapter 4, in full, is a reprint of the material as it appears in "Escher-Trace: a web application for pathway-based visualization of stable isotope tracing data," *BMC Bioinformatics*, vol. 21, 2020. Jack Mitchener and Zachary A. King were co-authors of this publication. Avi Kumar is the primary author of this publication. Christian M. Metallo is the corresponding author of this publication.

4.7 References

1. Wang, T. J., Larson, M. G., Vasan, R. S., Cheng, S., Rhee, E. P., Mccabe, E., Lewis, G. D., Fox, C. S., Jacques, P. F., Fernandez, C., Donnell, C. J. O., Carr, S. A., Mootha, V. K., Florez, J. C., Souza, A., Melander, O., Clish, C. B. & Gerszten, R. E. Metabolite profiles and the risk of developing diabetes. *Nature Medicine* **17,** 448–454 (2011).

2. Wellen, K. E. & Hotamisligil, G. S. Inflammation, stress, and diabetes. *The Journal of Clinical Investigation* **115,** 1111–1119 (2005).

3. Deberardinis, R. J., Lum, J. J., Hatzivassiliou, G. & Thompson, C. B. The Biology of Cancer : Metabolic Reprogramming Fuels Cell Growth and Proliferation. *Cell Metabolism* **7,** 11–20 (2008).

4. Hsu, P. P. & Sabatini, D. M. Cancer Cell Metabolism: Warburg and Beyond. *Cell* **134,** 703–707 (2008).

5. Sauer, U. Metabolic networks in motion: 13C-based flux analysis. *Molecular systems biology* **2,** 62 (2006).

6. Wiechert, W. 13C metabolic flux analysis. *Metabolic engineering* **3,** 195–206 (2001).

7. Jang, C., Chen, L. & Rabinowitz, J. D. Metabolomics and Isotope Tracing. *Cell* **173,** 822–837 (2018).

8. Fendt, S.-m., Bell, E. L., Keibler, M. A., Olenchock, B. A., Mayers, J. R., Wasylenko, T. M., Vokes, N. I., Guarente, L., Heiden, V. M. G. & Stephanopoulos, G. Reductive glutamine metabolism is a function of the a-ketoglutarate to citrate ratio in cells. *Nature Communications* **4,** 1–11 (2013).

9. Cordes, T. & Metallo, C. M. in *High-Throughput Metabolomics: Methods and Protocols* (ed D'Alessandro, A.) 219–241 (Springer New York, New York, NY, 2019).

10. Locasale, J. W., Grassian, A. R., Melman, T., Lyssiotis, C. A., Mattaini, K. R., Bass, A. J., Heffron, G., Metallo, C. M., Muranen, T., Sharfi, H., Sasaki, A. T., Anastasiou, D., Mullarky, E., Vokes, N. I., Sasaki, M., Beroukhim, R., Stephanopoulos, G., Ligon, A. H., Meyerson, M., Richardson, A. L., Chin, L., Wagner, G., Asara, J. M., Brugge, J. S., Cantley, L. C. & Heiden, V. M. G. Phosphoglycerate dehydrogenase diverts glycolytic flux and contributes to oncogenesis. *Nature Publishing Group* **43** (2011).

11. Mayers, J. R., Torrence, M. E., Danai, V. L., Papagiannakopoulos, T., Davidson, S. M., Bauer, M. R., Lau, A. N., Ji, B. W., Dixit, P. D., Hosios, A. M., Muir, A., Chin, C. R., Freinkman, E., Jacks, T., Wolpin, B. M., Vitkup, D. & Vander Heiden, M. G. Tissue of origin dictates branched-chain amino acid metabolism in mutant Kras-driven cancers. *Science* **353,** 1161–1165 (2016).

12. Wallace, M., Green, C. R., Roberts, L. S., Lee, Y. M., McCarville, J. L., Sanchez-Gurmaches, J., Meurs, N., Gengatharan, J. M., Hover, J. D., Phillips, S. A., Ciaraldi, T. P., Guertin, D. A., Cabrales, P., Ayres, J. S., Nomura, D. K., Loomba, R. & Metallo, C. M. Enzyme promiscuity drives branched-chain fatty acid synthesis in adipose tissues. *Nature Chemical Biology* **14,** 1021–1031 (2018).

13. Badur, M. G., Muthusamy, T., Parker, S. J., Ma, S., Mcbrayer, K., Cordes, T., Magana, J. H., Guan, K.-l. & Christian, M. Oncogenic R132 IDH1 Mutations Limit NADPH for De Novo Lipogenesis through (D)2-Hydroxyglutarate Production in Fibrosarcoma Cells. *Cell Reports* **25,** 1018–1026 (2018).

14. Fan, J., Ye, J., Kamphorst, J. J., Shlomi, T., Thompson, C. B. & Rabinowitz, J. D. Quantitative flux analysis reveals folate-dependent. *Nature* **510,** 298–302 (2014).

15. Lewis, C. A., Parker, S. J., Fiske, B. P., Mccloskey, D., Gui, D. Y., Green, C. R., Vokes, N. I., Feist, A. M., Heiden, V. M. G. & Metallo, C. M. Tracing Compartmentalized NADPH Metabolism in the Cytosol and Mitochondria of Mammalian Cells. *Molecular Cell* **55,** 1–11 (2014).

16. Tautenhahn, R., Patti, G., Rinehard, D. & Siuzdak, G. XCMS Online: a web-based platform to process untargeted metabolomic data. *Anal Chem.* **84,** 5035–5039 (2013).

17. Röst, H. L., Sachsenberg, T., Aiche, S., Bielow, C., Weisser, H., Aicheler, F., Andreotti, S., Ehrlich, H.-c., Gutenbrunner, P., Kenar, E., Liang, X., Nahnsen, S., Nilse, L., Pfeuffer, J., Rosenberger, G., Rurik, M., Schmitt, U., Veit, J., Walzer, M., Wojnar, D., Wolski, W. E., Schilling, O. & Choudhary, J. S. OpenMS : a flexible open-source software platform for mass spectrometry data analysis. *Nature Methods* **13,** 741–748 (2016).

18. Cho, K., Mahieu, N., Ivanisevic, J., Uritboonthai, W., Chen, Y. J., Siuzdak, G. & Patti, G. J. IsoMETLIN: A database for isotope-based metabolomics. *Analytical Chemistry* **86,** 9358–9361 (2014).

19. Millard, P., Delépine, B., Guionnet, M., Heuillet, M., Bellvert, F., Létisse, F. & Wren, J. IsoCor: Isotope correction for high-resolution MS labeling experiments. *Bioinformatics* **35,** 4484–4487 (2019).

20. Jungreuthmayer, C., Neubauer, S., Mairinger, T., Zanghellini, J. & Hann, S. ICT: Isotope correction toolbox. *Bioinformatics* **32,** 154–156 (2016).

21. Du, D., Tan, L., Wang, Y., Peng, B., Weinstein, J. N., Wondisford, F. E., Su, X. & Lorenzi, P. L. ElemCor: Accurate data analysis and enrichment calculation for high-resolution LC-MS stable isotope labeling experiments. *BMC Bioinformatics* **20,** 1–9 (2019).

22. Heinrich, P., Kohler, C., Ellmann, L., Kuerner, P., Spang, R., Oefner, P. J. & Dettmer, K. Correcting for natural isotope abundance and tracer impurity in MS-, MS/MS- and high-resolution-multiple-tracer-data from stable isotope labeling experiments with IsoCorrectoR. *Scientific Reports* **8,** 1–10 (2018).

23. Melamud, E., Vastag, L. & Rabinowitz, J. D. Metabolomic Analysis and Visualization Engine for LC–MS Data. *Analytical Chemistry* **82,** 9818–9826 (2010).

24. Chong, J., Soufan, O., Li, C., Caraus, I., Li, S., Bourque, G., Wishart, D. S. & Xia, J. MetaboAnalyst 4.0: towards more transparent and integrative metabolomics analysis. *Nucleic Acids Research* **46,** 486–494 (2018).

25. Droste, P., Miebach, S., Niedenführ, S., Wiechert, W. & Nöh, K. Visualizing multi-omics data in metabolic networks with the software Omix: a case study. *BioSystems* **105,** 154–161 (2011).

26. Norsigian, C. J., Pusarla, N., McConn, J. L., Yurkovich, J. T., Dräger, A., Palsson, B. O. & King, Z. BiGG Models 2020: multi-strain genome-scale models and expansion across the phylogenetic tree. *Nucleic Acids Research* **48,** 1–5 (2019).

27. King, Z. A., Dräger, A., Ebrahim, A., Sonnenschein, N., Lewis, N. E. & Palsson, B. O. Escher: A Web Application for Building, Sharing, and Embedding Data-Rich Visualizations of Biological Pathways. *PLoS Computational Biology* **11,** 1–13 (2015).

28. Qi, M., Wang, R., Jing, B., Jian, F., Ning, C. & Zhang, L. KEGG: Kyoto Encyclopedia of Genes and Genomes. *Nucleic Acids Research* **28,** 27–30 (2000).

29. Karp, P. D., Billington, R., Caspi, R., Fulcher, C. A., Latendresse, M., Kothari, A., Keseler, I. M., Krummenacker, M., Midford, P. E., Ong, Q., Ong, W. K., Paley, S. M. & Subhraveti, P. The BioCyc collection of microbial genomes and metabolic pathways. *Briefings in Bioinformatics* **20,** 1085–1093 (2018).

30. Fernandez, C. A., Des Rosiers, C., Previs, S. F., David, F. & Brunengraber, H. Correction of 13C mass isotopomer distributions for natural stable isotope abundance. *Journal of Mass Spectrometry* **31,** 255–262 (1996).

31. Semenza, G. L. HIF-1 : upstream and downstream of cancer metabolism. *Current Opinion in Genetics and Development* **20,** 1–10 (2010).

32. Metallo, C. M., Gameiro, P. A., Bell, E. L., Mattaini, K. R., Yang, J., Hiller, K., Jewell, C. M., Johnson, Z. R., Irvine, D. J., Guarente, L., Kelleher, J. K. & Vander, M. G. Reductive glutamine metabolism by IDH1 mediates lipogenesis under hypoxia. *Nature* **481,** 380–384 (2012).

Chapter 5

Analysis of high-resolution lipidomic data with Escher-Trace

5.1 Abstract

High-resolution mass spectrometry is an invaluable tool for identification and quantitation of biological macromolecules. These instruments have become particularly useful for measuring molecule classes containing numerous species of similar mass and structure, such as lipids. However, processing the large data sets generated by high-resolution mass spectrometers is time intensive. Layering stable isotope tracing onto lipidomic experiments allows for tremendous insight into intracellular fluxes, however, further complicates analysis. Here we present an analytical pipeline which accelerates discovery of metabolic insights from these dense data sets through integration of El-MAVEN and the Escher-Trace visualization platform.

5.2 Introduction

Mass spectrometry has been an essential technique for compound identification by m/z fingerprinting, since its invention in the mid-20th century. However, as the specificity of the compounds to be quantified increases, absolute quantitation is complicated by limitations in differential mass resolution between similarly composed or isobaric molecules. In recent decades, advances in instrumentation have produced high-resolution mass spectrometers (HRMS) which are further able to resolve isobaric species, ultra-high-performance liquid chromatography (UHPLC), allowing for separation and quantitation of a significantly larger number of molecules, as well as tandem mass spectrometers which include additional quadrupoles or collision cells to break apart molecules, enabling secondary confirmation of their composition by MS2 [1]. The budding field of lipidomics has particularly benefited from adoption of high-resolution tandem mass spectrometry. Lipids are highly abundant in cells, and serve numerous essential tasks including formation of membranes, energy storage, protein modification, and signaling. The lipidome contains thousands of species classified across eight categories: fatty acyls, glycerolipids, glycerophospholipids, sphingolipids, sterols, prenol lipids, saccharolipids, and polyketides [2, 3]. Numerous unique species exist within each of these classes differing in backbone base, head group, and acyl-chain composition (both in length and saturation level) [4]. Differences between these species can be as small as the relative positioning of acyl-chains or the location of double bonds on conjugated fatty acids, producing unique species with identical masses. Utilizing high-resolution tandem mass spectrometry for lipidomic analysis allows for identification of numerous isobaric lipid species, which would be indistinguishable if using nominal resolution single quadrupole instruments. This advancement has also led to an increase in the volume of data generated per sample, requiring increasingly computationally intense analysis. Layering on stable isotope tracers to lipidomic experiments permits quantitation of lipid metabolism fluxes, however, also adds another dimension of complexity to analysis.

Various software packages and workflows exist for analyzing high-resolution mass spectrometry data. Vendor software's (such as Agilent Technologies' MassHunter) are used for peak detection and alignment. LipidMS, LipiDex, and LipidIMMS enable species identification [5–7]. MAVEN facilitates quantitation of high-resolution MS metabolite labeling, but it is not designed for data visualization with metabolic network topology [8]. Currently no software is specifically catered toward analysis of stable isotope tracing lipidomics. Escher-Trace fulfills this need for nominal resolution mass spectrometry. Its easy-to-use graphical user interface makes it possible for users to quickly upload tracing data sets, correct for natural isotope abundance, and visualize their data in the context of a metabolic map, however, the correction algorithm and data input are currently unfit for handling HRMS data. We have expanded Escher-Trace's functionality, implementing integration with El-MAVEN, a popular MAVEN distro built by Elucidata, using an intermediate Matlab script (Escher-Trace_HRMS.m) to allow for visualization and analysis of HRMS data in Escher-Trace.

The original analysis capabilities of Escher-Trace can be leveraged for interpretation of HRMS data. Users will benefit from abundance normalization, metabolite quantitation, enrichment calculation, the ability to quickly sift through all data types of all metabolites, alter graph aesthetics, as well as additional features described in the original Escher-Trace publication [9]. New features have also been added specifically catering to the needs of users analyzing complex high-resolution large molecule tracing data sets. These include the ability to automatically hide isotopologues with low labeling from mass isotopomer distributions, allowing for compression of otherwise unruly graphs into a cleaner format which still communicates all critical information, as well as allowing all labeling and abundance data to be exported from Escher-Trace in the form of a CSV table with a single click, allowing for downstream statistical analysis to performed outside of the platform.

5.3 Implementation

The analytical pipeline for visualizing high-resolution mass spec data in Escher-Trace requires a few preliminary steps (Fig. 1). Data files generated by high-resolution mass spectrometers are typically in vendor specific file formats (.RAW, .raw, .wiff, .d and more). These files need to be converted into mzXML files using freely available file converters such as MSConvert from Proteowizard [10]. The mzXML files are then uploaded to El-MAVEN for peak identification and alignment. El-MAVEN is a commercially available distribution of the MAVEN software package, developed by Elucidata [11]. In El-MAVEN, users are able to bookmark data (including isotopologue labeling) from metabolites of interest. As part of the pipeline, users bookmark all desired metabolites of interest and then use El-MAVEN's built in export data to CSV functionality, producing a CSV file containing the abundances of all identified isotopologues detected for each bookmarked metabolite across all sample files. However, the isotopologue abundances in this El-MAVEN generated CSV file are not corrected for natural isotope abundance and the isotopologues are often presented in nonsequential order.

At this point, users are generally required to perform time consuming manual reorganization of the isotopologue data and subsequently correct for natural isotopologue abundance one metabolite at a time, using additional freely available high-resolution correction software [12–15]. These steps can instead be performed automatically using the Escher-Trace_HRMS.m Matlab script. The script utilizes an existing correction algorithm for high-resolution mass spectrometer data which was produced at Princeton University by Professor Joshua Rabinowitz's lab [16]. The algorithm differs from the correction matrix method utilized by Escher-Trace in two ways: (1) because high-resolution mass spectrometers are able to resolve elemental isotopologues, only natural abundance of ^{13}C is utilized for building the correction matrix used in the matrix calculations required to subtract natural isotope abundance from the experimental labeling distributions, (2) a linear solver is used to ensure that the corrected isotopologue distributions sum to 100% and

contain no negative labeling. This intermediary Matlab script is currently necessary as a robust JavaScript linear solver library is not available, so no such solver can be included directly into the Escher-Trace web interface. The Matlab script generates an new CSV file, whose name can be distinguished by the inclusion of "_corrected_ET_import" tacked on to the uploaded file's name.

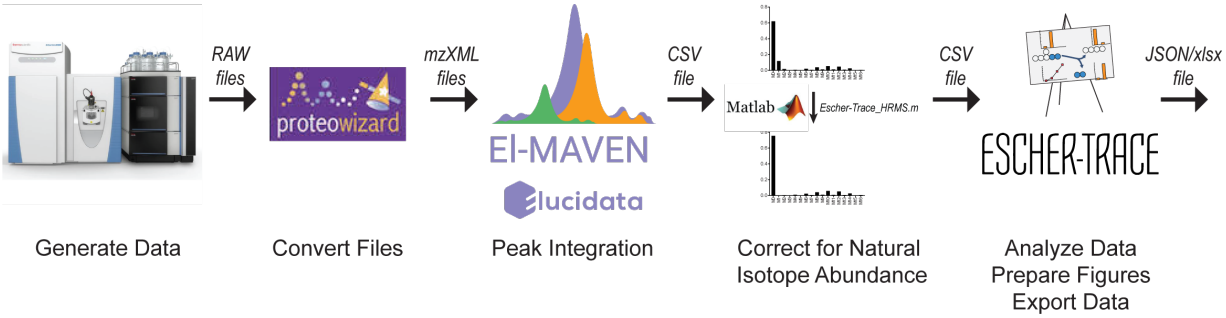

Figure 5.1: **Escher-Trace HRMS analysis pipeline.**

This newly generated CSV file can be imported into the updated Escher-Trace interface which now includes an additional file upload type **MAVEN** (Fig. 2). Alternatively, if isotope correction is not necessary, users can directly upload the CSV data file output from El-MAVEN as a MAVEN file as well. After upload of the file, the user will be walked through the standard Escher-Trace data organization steps and finally the data will be visualized on an Escher map [17] (Fig. 3). From here the user is able to click and drag their figures and access the standard Escher-Trace functionality including: (1) accessing metabolite abundance, labeling, and enrichment data, (2) normalizing abundances to an experimental condition or internal standard, (3) quantifying metabolite abundances to a labeled internal standard, (4) generating graphs comparing metabolite data across metabolites, (5) visualizing kinetic data in time course graphs, (6) altering graph aesthetics, and (7) saving and reloading work spaces using the Escher-Trace main menu and context menus.

Within the Escher-Trace interface additional features have been added including **Enter Label Limit %** under the **Data Displayed** heading in the Escher-Trace menu. This feature enables the user to input a number that will set a boundary value, and isotopologues across all

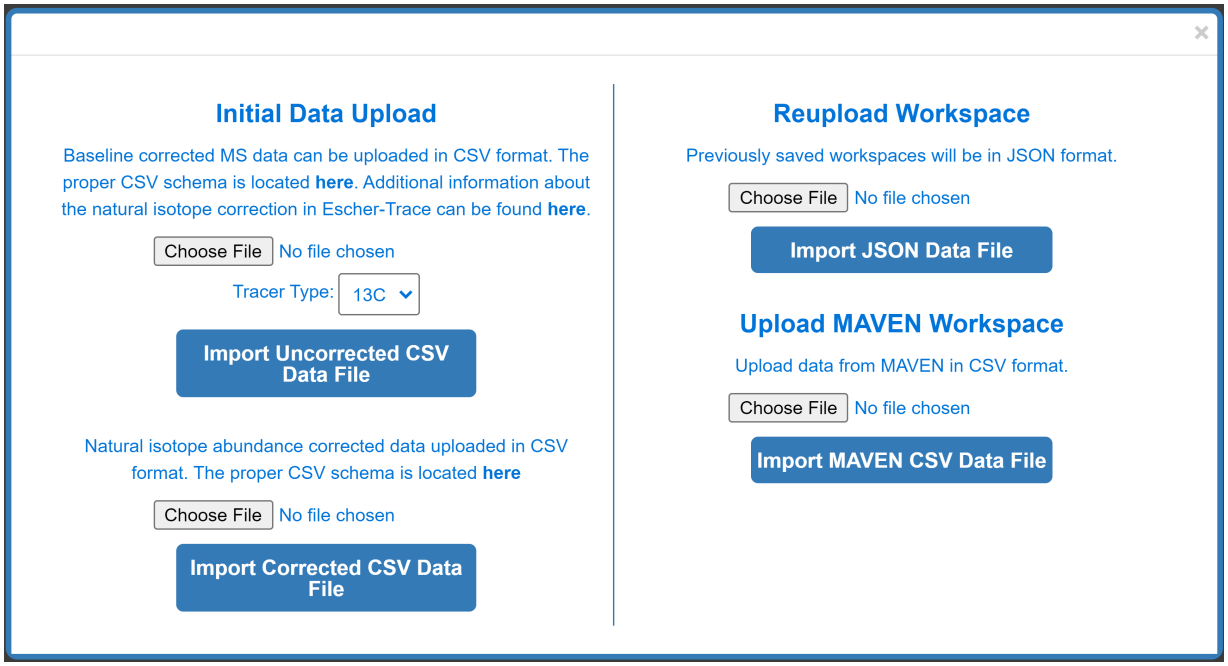

Figure 5.2: **Uploading El-MAVEN data to Escher-Trace.**

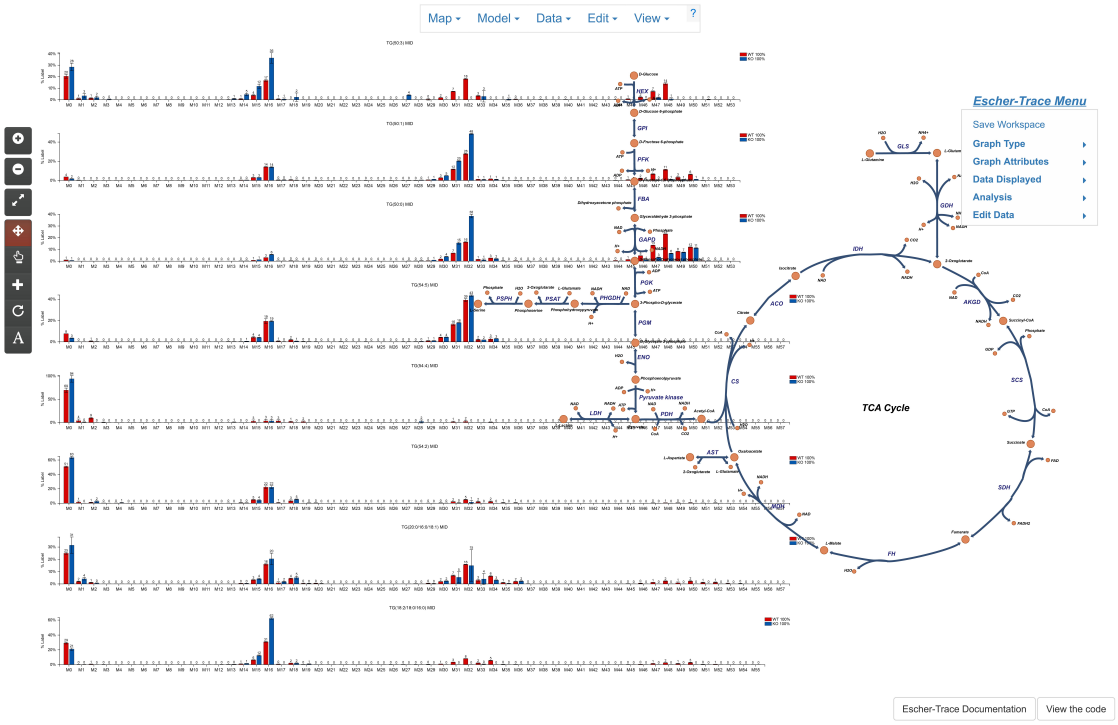

Figure 5.3: **Initial visualization of HRMS data in Escher-Trace.**

metabolites which contain labeling percentages below the set value, across every experimental condition, will be hidden from Escher-Trace graphs. This feature becomes increasingly useful for interpreting labeling of large metabolites, such as lipid species, many of which can contain >50 carbons. Visualization of the labeling distributions of these species in standard bar graphs can produce unwieldy plots which are difficult to interpret. However, depending on the applied tracer, in such large species many isotopologues will contain negligible amounts of labeling (<1%), and hiding these species facilitates more direct interpretation of the changes in isotopologues containing significant label (Fig. 4a).

The ability for users to export labeling and abundance data from Escher-Trace has also been added. This feature can be accessed by selecting **Export Data** directly from the Escher-Trace menu. Selecting this option will download a CSV file containing the total abundances and isotopic labeling patterns for all metabolites loaded to Escher-Trace. This feature was commonly requested from users of the original release of Escher-Trace who wanted to use the tool specifically for its nominal resolution natural isotope abundance correction capabilities and simply export their corrected data. Having the ability to export all abundance and labeling data directly from Escher-Trace is even more necessary for the HRMS workflow introduced here, as compiling all such information directly from MAVEN/El-MAVEN files requires significant manual data reorganization and summation in Excel. Once the data file is downloaded, the user is free to perform advanced statistical analysis on their data as they please.

Lastly, users are now able to generate graphs with split Y axes by right clicking the graph of interest and selecting **Change Graph** $\rightarrow$ **Y axis**. These graph types are common in scientific literature and this functionality is particularly useful when labeling distributions, enrichments, or abundances vary significantly between experimental conditions, allowing the user to simultaneously highlight both large as well as subtle alterations within the same figure panel (Fig. 4b).

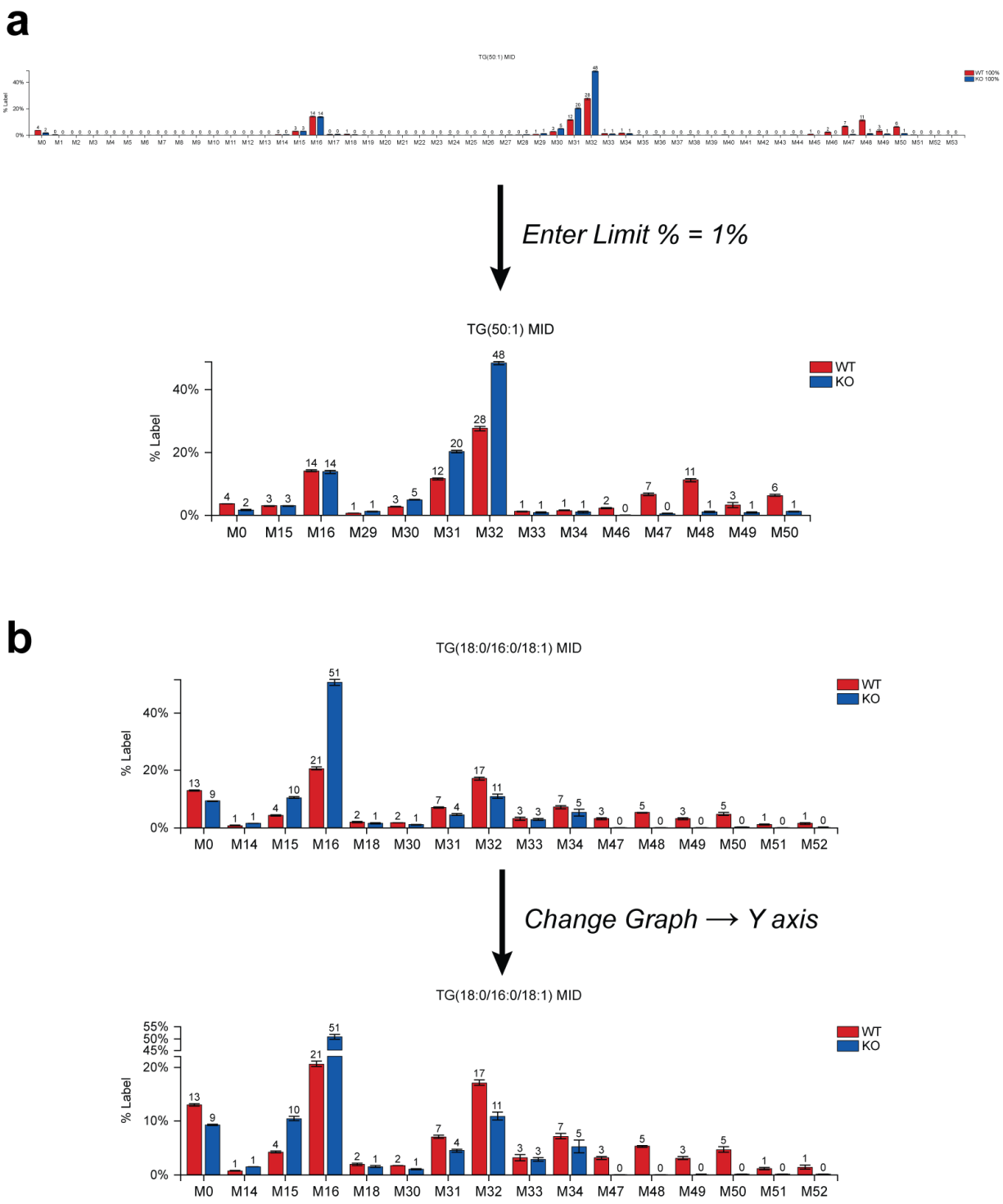

Figure 5.4: **New features in Escher-Trace.**A) Enter Limit % functionality makes it possible to automatically clean up MIDs containing disparate labeling across isotopologues. B) Change Graph → Y axis enables y-axis of Escher-Trace graphs to be split.

5.4 Discussion

High-resolution mass spectrometry is an exceptionally valuable analytical tool, allowing for quantitation of more molecules than any other mass spectrometer system to date. The technology has been widely adopted in the biotechnology and pharmaceutical sector in addition to basic science research [18]. However, analysis of the data generated by HRMS is time consuming and can be difficult to interpret due to the wealth of information it contains. The analysis is further complicated when the data sets are produced from stable isotope tracing experiments. These experiments are highly valuable and provide insight on intracellular fluxes, however, require additional preprocessing of the data including natural isotope correction.

By expanding Escher-Trace to be able to handle incorporation of HRMS data, we have presented an analysis pipeline which accelerates discovery of metabolic insights from these dense data sets. We provide a Matlab script which directly processes El-MAVEN outputs and automatically corrects for natural isotope abundance, removing time spent on tedious manual data curation. Furthermore, by permitting the output file generated by the Matlab script, as well as raw El-MAVEN outputs, to be directly imported into Escher-Trace, we have automated the means of visualizing HRMS data in the context of metabolic maps, improving interpretation and communication of the data.

There is still room for improvement in the presented analysis pipeline. Incorporating the HRMS correction algorithm and a linear solver into Escher-Trace would allow for removal of the Matlab data processing step and further improve the efficiency of the pipeline. Currently there are few options for solving linear systems of equations with constraints using JavaScript, however such a library would be massively beneficial to the broader web development and research communities. Alternatively, a server could be established which would host the Matlab or a similar python natural isotope correction script, enabling user submitted data to be processed on the server side and sent back via PHP, freeing the user of downloading and running the script

on their personal machine. As HRMS datasets facilitate quantitation of a larger number of metabolites than nominal resolution machines, advanced plotting options would be beneficial including volcano plots, which are commonly used in lipidomics and metabolomics literature to identify interesting species and trends in data. Implementation of a statistics library would also be beneficial for both recognizing and visualizing statistically significant findings in Escher-Trace. Once a robust statistical JavaScript library becomes available, implementation of this feature set should be routine as the data structure of metabolite and labeling data in Escher-Trace is simple to navigate. Lastly, creation of more robust Escher maps which focus on whole lipid assembly and/or include a broader range of metabolites in general, would be beneficial as the number and diversity of molecules quantified from typical HRMS experiments is much greater than that of nominal resolution GC-MS experiments.

Overall, the HRMS Escher-Trace expansion extends the data visualization functionality of Escher-Trace to a wider user base and demonstrates the opportunity to continue to grow the platform for incorporation of additional data types which eventually could facilitate interpretation of biological phenotypes from multi-omics level data.

5.5 Acknowledgements

We thank all members of the Metallo laboratory for their support and helpful discussions. Support for AK and C.M.M. was provided by NSF CAREER Award #1454425 (C.M.M.). The funding bodies did not play any roles in the design of the study and collection, analysis, and interpretation of data and in writing the manuscript.

Chapter 5, in full, is currently being prepared for submission for publication. Avi Kumar is the primary author of this publication. Christian M. Metallo is the corresponding author of this publication.

5.6 References

1. Gowda, G. A. N. & Djukovic, D. in *Mass Spectrometry in Metabolomics: Methods and Protocols* (ed Raftery, D.) 3–12 (Springer New York, New York, NY, 2014). https://doi.org/10.1007/978-1-4939-1258-2_1.

2. Fahy, E., Subramaniam, S., Murphy, R., Nishijima, M., Raetz, C., Shimizu, T., Spener, F., Meer, G., Wakelam, M. & Dennis, E. Update of the LIPID MAPS comprehensive classification system for lipids. *The Journal of Lipid Research* **50,** S9–S14 (2009).

3. Shevchenko, A. & Simons, K. Lipidomics: Coming to grips with lipid diversity. *Nature Reviews Molecular Cell Biology* **11,** 593–598 (2010).

4. Harayama, T. & Riezman, H. Understanding the diversity of membrane lipid composition. *Nature Reviews Molecular Cell Biology* **19,** 281–296 (2018).

5. Alcoriza-Balaguer, M. I., García-Cañaveras, J. C., López, A., Conde, I., Juan, O., Carretero, J. & Lahoz, A. LipidMS: An R Package for Lipid Annotation in Untargeted Liquid Chromatography-Data Independent Acquisition-Mass Spectrometry Lipidomics. *Analytical Chemistry* **91,** 836–845 (2019).

6. Hutchins, P. D., Russell, J. D. & Coon, J. J. LipiDex: An Integrated Software Package for High-Confidence Lipid Identification. *Cell Systems* **6,** 621–625.e5 (2018).

7. Zhou, Z., Shen, X., Chen, X., Tu, J., Xiong, X. & Zhu, Z. J. LipidIMMS Analyzer: Integrating multi-dimensional information to support lipid identification in ion mobility - Mass spectrometry based lipidomics. *Bioinformatics* **35,** 698–700 (2019).

8. Melamud, E., Vastag, L. & Rabinowitz, J. D. Metabolomic Analysis and Visualization Engine for LC–MS Data. *Analytical Chemistry* **82,** 9818–9826 (2010).

9. Kumar, A., Mitchener, J., King, Z. A. & Metallo, C. M. Escher-Trace: A web application for pathway-based visualization of stable isotope tracing data. *BMC Bioinformatics* **21,** 1–10 (2020).

10. Adusumilli, R. & Mallick, P. in *Methods in Molecular Biology* (eds Comai, L., Katz, J. E. & Mallick, P.) 339–368 (Humana Press, New York, NY, 2017).

11. Agrawal, S., Kumar, S., Sehgal, R., George, S., Gupta, R., Poddar, S. & Jha, A. in *Methods in Molecular Biology* (ed D'Alessandro, A.) 403–430 (Humana Press, New York, NY, 2019).

12. Du, D., Tan, L., Wang, Y., Peng, B., Weinstein, J. N., Wondisford, F. E., Su, X. & Lorenzi, P. L. ElemCor: Accurate data analysis and enrichment calculation for high-resolution LC-MS stable isotope labeling experiments. *BMC Bioinformatics* **20,** 1–9 (2019).

13. Heinrich, P., Kohler, C., Ellmann, L., Kuerner, P., Spang, R., Oefner, P. J. & Dettmer, K. Correcting for natural isotope abundance and tracer impurity in MS-, MS/MS- and high-resolution-multiple-tracer-data from stable isotope labeling experiments with IsoCorrectoR. *Scientific Reports* **8,** 1–10 (2018).

14. Jungreuthmayer, C., Neubauer, S., Mairinger, T., Zanghellini, J. & Hann, S. ICT: Isotope correction toolbox. *Bioinformatics* **32,** 154–156 (2016).

15. Millard, P., Delépine, B., Guionnet, M., Heuillet, M., Bellvert, F., Létisse, F. & Wren, J. IsoCor: Isotope correction for high-resolution MS labeling experiments. *Bioinformatics* **35,** 4484–4487 (2019).

16. Su, X., Lu, W. & Rabinowitz, J. D. Metabolite Spectral Accuracy on Orbitraps. *Analytical Chemistry* **89,** 5940–5948 (2018).

17. King, Z. A., Dräger, A., Ebrahim, A., Sonnenschein, N., Lewis, N. E. & Palsson, B. O. Escher: A Web Application for Building, Sharing, and Embedding Data-Rich Visualizations of Biological Pathways. *PLoS Computational Biology* **11,** 1–13 (2015).

18. Xian, F., Hendrickson, C. L. & Marshall, A. G. High resolution mass spectrometry. *Analytical Chemistry* **84,** 708–19 (2012).

Chapter 6

Conclusions

Lipid metabolism is dysregulated in multiple metabolic disease states. Only a subset of cell types, such as highly proliferative cancer cells, undergo *de novo* lipogenesis to support their function and/or proliferation. The goal of this dissertation was to profile changes in fatty acid metabolism in cancer cells upon disruption of lipogenic synthesis and nutrient utilization, as well as expand the tools available for analyzing metabolic datasets.

The first chapter, titled "Profiling fatty acid metabolism using stable isotope tracing" provides an overview of relevant literature concerning metabolic reprogramming of mammalian cells under highly proliferative disease states. This work introduces the multi-organelle nature of lipid metabolism, and discusses the therapeutic window targeting related pathways provides. Additionally, a review of the advancements in instrumentation as well as modeling frameworks for profiling intracellular metabolic flux are discussed. Overall, this section considers the relevance of studying metabolic alterations in disease states and presents the techniques utilized to survey them.

The second chapter, titled "NaCT/SLC13A5 facilitates citrate import and metabolism under nutrient-limited conditions" examines the impact of extracellular citrate uptake on sodium citrate transporter, NaCT, -expressing cell types. Citrate is abundant in human plasma, but absent

in most cell culture medias, so its impact on cell metabolism is ignored in most *in vitro* studies. We found that supplemented extracellular citrate was utilized for TCA anaplerosis as well as fatty acid metabolism in hepatoma and neuronal cell lines, however its presence had minimal impact on either cell type in nutrient rich conditions. We identified that citrate uptake, by NaCT, was protective against glutamine deprivation as well as zinc-induced cell toxicity in hepatoma cells. These findings demonstrate that non-canonical nutrient sources, such as citrate, provide utility to cells experiencing stress. Future work will involve utilizing more physiologically relevant model systems to investigate NaCT activity and citrate uptake's role in protecting neuronal cells against metal ion toxicity.

The third chapter, titled "ATP-citrate lyase deficiency highlights critical sources of lipogenic acetyl-CoA in cancer cells" investigates cytosolic acetyl-CoA synthesis in lipogenic cells by genetically targeting ATP-Citrate Lyase (ACLY) and/or acetyl-CoA Synthetase (ACSS2) and quantifying fatty acid metabolism in liver and lung derived cancer cell lines. The study confirmed that utilization of acetate, by ACSS2, for fatty acid synthesis was upregulated upon ACLY-knockout. Furthermore, alternative acetyl-CoA synthesis mechanisms including *de novo* acetate synthesis as well as peroxisomal β-oxidation were found to be active and increasingly essential to growth in ACLY-deficient cells. These results demonstrate that multiple layers of network redundancy can compensate for deficiencies in metabolic enzymes. Future work should focus on quantifying the magnitude of these effects in an *in-vivo* system and explore their implications in the context of whole-body lipid physiology.

The fourth chapter, titled "Escher-Trace: A Web Application for Pathway-Based Visualization of Stable Isotope Tracing Data" details the feature set and provides a walk through of the new web-based data visualization platform, Escher-Trace. The website allows users to correct nominal resolution stable isotope traced data for natural isotope abundance, generate publication quality graphs of metabolite labeling, and present data in the context of pathways. This work confirmed that overlaying labeling data on top of pathway maps improves interpretation

of complex metabolic data sets. Future work should add functionality and allow for incorporation of additional -omic level data types in the visualization platform.

The fifth chapter, titled "Analysis of high-resolution lipidomic data with Escher-Trace" introduces a data analysis pipeline for interpretation of high-resolution mass spectrometer data. The pipeline enables users to visualize high-resolution data in Escher-Trace by making the platform compatible with El-MAVEN data outputs. An intermediate Matlab script is provided to process El-MAVEN outputs and perform natural abundance correction using an existing algorithm developed specifically for correction of high-resolution data. Future work will incorporate statistical packages as well as advanced graphing options, allowing users to identify and plot statistical significance within Escher-Trace.

The metabolic network acts in concert with environmental cues and signaling cascades to maintain cellular homeostasis. This dissertation highlights the utility of probing metabolic pathways using existing techniques and introduces new tools which contextualize the data. Taken together these chapters demonstrate the benefits of building comprehensive visualization platforms for metabolic datasets and establishes that fatty acid synthesis is highly plastic in lipogenic cells. Understanding these modes of reprogramming, and building tools which enable such findings, will aid researchers in discovery of underlying disease mechanisms and identification of unique therapeutic targets.

Chapter S1

Supplement to Chapter 2

S1.1 Supplemental Tables and Figures

Table S1.1: MFA of compartmental citrate catabolism in Huh7 hepatoma cells grown under hypoxia. Related to Figure 4.

Pathway/Reaction	Flux (fmol/cell/hr)	Lower bound (fmol/cell/hr)	Upper bound (fmol/cell/hr)
Glycolysis (net fluxes)			
Glc.x → G6P	682	644.7	749.4
G6P → F6P	682	264.1	719.3
F6P → DHAP + GAP	681	593.1	714.9
DHAP → GAP	681	593.1	714.9
GAP → 3PG	1362	1245	1475
3PG → PEP	1362	1245	1475
PEP → Pyr.c	1362	1245	1475
Pyr.c → Lac	1375	1306	1449
Lac → Lac.x	1375	1306	1449
Pyr.c → Ala	3.589	3.176	3.981
Pyr.m → Ala	0.1301	0.05217	0.1871
Pentose Phosphate Pathway (net fluxes)			
G6P → P5P + CO2	1.00E-07	0	430.2
P5P + P5P → S7P + GAP	-0.4812	-0.5423	161.2
S7P + GAP → F6P + E4P	-0.4812	-0.5423	161.2
P5P + E4P → F6P + GAP	-0.4812	-0.5423	161.2
Pyruvate Oxidation and Anaplerotic Reactions (net fluxes)			

Table S1.1 – continued from previous page

Pathway/Reaction	Flux (fmol/cell/hr)	Lower bound (fmol/cell/hr)	Upper bound (fmol/cell/hr)
Cit.x → Cit.e	9.648	9.099	10.42
Cit.e → Cit.c	10.01	9.458	10.78
Pyr.c → Pyr.m	4.631	4.097	5.264
Pyr.m + CO2 → Oac.m	14.54	11.97	18.54
Mal.m → Pyr.m + CO2	19.9	15.9	22.68
Mal.c → Pyr.c + CO2 21.51	18.46	24.92	
Pyr.m → AcCoA.m + CO2	9.862	7.82	11.71
FAO → AcCoA.m	7.791	5.094	9.553
Glu.m → α-KG.m	-2.385	-10.69	45.04
Gln → Glu.c	27.7	27.39	28.14
Gln.x → Gln	29.69	29.53	29.86
Glu.c → Glu.x	3.914	1.731	5.86
Glu.c → Glu.m	-4.74E-11	-8.364	54.98
α-KG.c → Glu.c	-21.4	-30.19	32.48
α-KG.m → α-KG.c	-34.07	-42.24	-26.44
TCA Cycle (net fluxes)			
AcCoA.m + Oac.m → Cit.m	17.65	15.99	19.19
Cit.m → α-KG.m + CO2	-0.5944	-1.901	1.646
α-KG.m → Suc + CO2	31.09	26.99	34.96
Suc → Fum.m	31.09	26.99	34.96
Fum.m → Mal.m	31.09	26.99	34.96
Mal.m → Oac.m	5.665	-0.3408	9.143
Oac.m → Asp.m	2.553	-1.954	4.303
Mal.c → Oac.c	-2.83E-14	-17.13	4.285
Oac.c → Asp.c	15.22	0.2183	17.8
Asp.c → Fum.c	15.99	2.24E-13	18.6
Mal.c → Fum.c	-15.99	-18.6	0
Mal.c → Mal.m	-5.527	-14.49	-1.005
Asp.m → Asp.c	2.553	-1.954	4.303
Cit.c → α-KG.c + CO2	12.67	10.98	14.97
Cit.m → Cit.c	18.25	16.38	20.73
Biomass			
Cit.c → AcCoA.c + Oac.c	15.22	12.6	16.9
0*AcCoA.c + 0*AcCoA.c + 0*AcCoA.c + 0*AcCoA.c + 0*AcCoA.c + 0*AcCoA.c + 0*AcCoA.c + 0*AcCoA.c → Palm.s	0.00769	0	Inf
Palm.d → Palm.s	0.1254	0	Inf
114*Asp.c + 152*Glu.c + 152*Glu.m + 237*Ala + 127*Gln + 970*AcCoA.c +	0.01569	0.01299	0.01742

Table S1.1 – continued from previous page

Pathway/Reaction	Flux (fmol/cell/hr)	Lower bound (fmol/cell/hr)	Upper bound (fmol/cell/hr)
92*P5P → Biomass			
Dilution/Mixing			
0*Pyr.c → Pyr.mnt	0.9488	0.9335	0.9643
0*Pyr.m → Pyr.mnt	0.05123	0.03573	0.06649
0*Mal.c → Mal.mnt	0.02303	1.00E-07	0.09788
0*Mal.m → Mal.mnt	0.977	0.9021	1
0*Asp.c → Asp.mnt	1	1.00E-07	1
0*Asp.m → Asp.mnt	1.00E-07	0	1
0*Fum.m → Fum.mnt	0.8298	0.6784	0.9363
0*Fum.c → Fum.mnt	0.1702	0.0637	0.3216
0*Cit.m → Cit.mnt	0.1439	1.00E-07	1
0*Cit.c → Cit.mnt	0.8561	0	1
0*Glu.m → Glu.mnt	1	0.9606	1
0*Glu.c → Glu.mnt	1.00E-07	0	0.03941
0* α-KG.m → α-KG.mnt	0.4998	1.00E-07	1
0* α-KG.c → α-KG.mnt	0.5002	0	1
Pyr.mnt → Pyr.fix	1	1	1
Asp.mnt → Asp.fix	1	1	1
Mal.mnt → Mal.fix	1	1	1
Fum.mnt → Fum.fix	1	1	1
Cit.mnt → Cit.fix	1	1	1
α-KG.mnt → α-KG.fix	1	1	1
Glu.mnt → Glu.fix	1	1	1
Glycolysis (exchange fluxes)			
G6P ← F6P	1.00E-07	0	Inf
DHAP ← GAP	0.00932	0	Inf
GAP ← 3PG	24.34	0	Inf
Pyr.c ← Lac	1.00E-07	0	Inf
Pentose Phosphate Pathway (exchange fluxes)			
P5P + P5P ← S7P + GAP	1.00E-07	0	Inf
S7P + GAP ← F6P + E4P	1.00E-07	0	Inf
P5P + E4P ← F6P + GAP	301.1	0	Inf
Anaplerotic Reactions (exchange fluxes)			
Cit.e ← Cit.c	0.3594	0.3217	0.382
Glu.m ← α-KG.m	1.563	0	Inf
Glu.c ← Glu.m	1.00E-07	0	61.6
α-KG.c ← Glu.c	1.00E-07	0	Inf
α-KG.m ← α-KG.c	157.6	0	Inf
TCA Cycle (exchange fluxes)			

Table S1.1 – continued from previous page

Pathway/Reaction	Flux (fmol/cell/hr)	Lower bound (fmol/cell/hr)	Upper bound (fmol/cell/hr)
Cit.m ← α-KG.m + CO2	1.00E-07	0	2.92
Suc ← Fum.m	0.001999	0	Inf
Fum.m ← Mal.m	3.35E+05	364.3	Inf
Mal.m ← Oac.m	69.2	32.19	178.2
Oac.m ← Asp.m	1.00E-07	0	Inf
Mal.c ← Oac.c	1.00E-07	0	Inf
Oac.c ← Asp.c	0.05184	0	Inf
Mal.c ← Fum.c	1768	0	Inf
Mal.c ← Mal.m	1.00E-07	0	4.497
Asp.m ← Asp.c	0.3676	0	Inf
Cit.c ← α-KG.c + CO2	1.00E-07	0	2.124
Cit.m ← Cit.c	1.00E-07	0	Inf

SSR = 170.4 Expected SSR = [141.2 214.6] (95.0% conf., 176 DOF)

Compartment abbreviations: c, cytosol; m, mitochondrial; mnt, measured (utilized to indicate that measured MIDs reflect aggregated metabolite labeling across all compartments); x, extracellular; e, extracellular exchange intermediate (utilized in order to allow for incorporation of both citrate uptake and efflux).

Table S1.2: **Metabolite fragments considered in MFA. Related to Figure 4.**

Metabolite	Carbons	Formula	Mass (m/z)
Pyruvate	1,2,3	$C_6H_{12}O_3NSi$	174
Lactate	2,3	$C_{10}H_{25}O_2Si_2$	233
Lactate	1,2,3	$C_{11}H_{25}O_3Si_2$	261
Alanine	2,3	$C_{10}H_{26}ONSi_2$	232
Alanine	1,2,3	$C_{11}H_{26}O_2NSi_2$	260
α-KG	1,2,3,4,5	$C_{14}H_{28}O_5NSi_2$	346
Malate	1,2,3,4	$C_{18}H_{39}O_5Si_3$	419
Succinate	1,2,3,4	$C_{12}H_{25}O_4Si_2$	289
Fumarate	1,2,3,4	$C_{12}H_{23}O_4Si_2$	287
Aspartate	1,2	$C_{14}H_{32}O_2NSi_2$	302
Glutamate	1,2,3,4,5	$C_{19}H_{42}O_4NSi_3$	432
Glutamine	1,2,3,4,5	$C_{19}H_{43}O_3N_2Si_3$	431
Palmitate	1-16	$C_{17}H_{34}O_2$	270

Table S1.3: **Oligonucleotide sequences used in this study. Related to Figures 1 and 5.**

Primer name	Sequence	Application
ACLY (human) fwd	TCGGCCAAGGCAATTTCAGAG	qRT-PCR
ACLY (human) rev	CGAGCATACTTGAACCGATTCT	qRT-PCR
SLC13A5 (human) fwd	CTGCCACTCGTCATTCTGATG	qRT-PCR
SLC13A5 (human) rev	ATGTTGGTGTCCTTCATGTACTG	qRT-PCR
r18s (human) fwd	AGTCCCTGCCCTTTGTACACA	qRT-PCR
r18s (human) rev	CGATCCGAGGGCCTCACTA	qRT-PCR
Slc13a5 (rat) fwd	GGTGCACAGATGTCATCCCA	qRT-PCR
Slc13a5 (rat) rev	AGCATGTTGGTGTCCGTCAT	qRT-PCR
r18s (rat) fwd	AGAAACGGCTACCACATCCA	qRT-PCR
r18s (rat) rev	CTCGAAAGAGTCCTGTATTGT	qRT-PCR
SLC13A5 (human) PCR fwd	AGGCATCCCATAGTGACCCT	Target Site PCR Primer
SLC13A5 (human) PCR rev	CACAGAACTGCCGGAGTTGT	Target Site PCR Primer

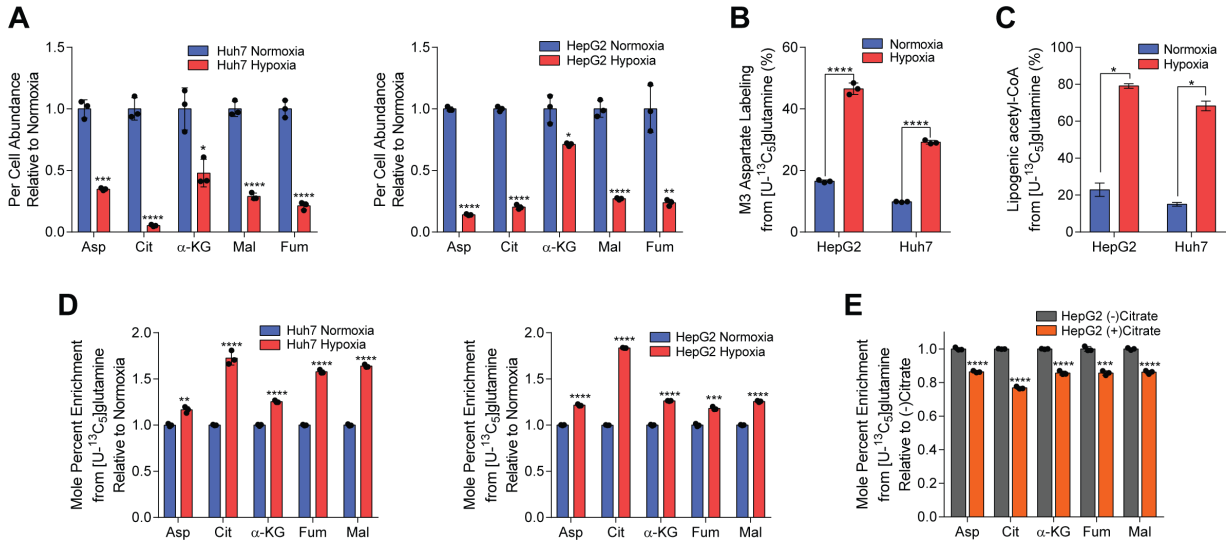

Figure S1.1: **Citrate dilutes central carbon pathway labeling in hepatocellular carcinoma and neuronal cells in hypoxia. Related to Figure 2.** A) Per cell abundances of TCA intermediates in Huh7 (left) and HepG2 (right) cells grown in normoxia or hypoxia for 48 hours, relative to normoxia (n=3). B) Percent labeling of M3 aspartate from [U-$^{13}C_5$]glutamine in HepG2 and Huh7 cells grown in normoxia or hypoxia for 48 hours (n=3). C) Percent of lipogenic acetyl-CoA contributed by [U-$^{13}C_5$]glutamine in HepG2 and Huh7 cells grown in normoxia or hypoxia for 48 hours (n=3). D) Mole percent enrichment of TCA intermediates from [U-$^{13}C_5$]glutamine in Huh7 (left) and HepG2 (right) cells grown in normoxia or hypoxia for 48 hours, relative to normoxia (n=3).E) Mole percent enrichment of TCA intermediates from [U-$^{13}C_5$]glutamine in HepG2 cells grown in hypoxia $\pm$ 500 μM citrate for 48 hours, relative to (-) citrate (n=3). Asp, aspartate; Cit, citrate; α-KG, α-ketoglutarate; Fum, fumarate; Mal, malate. In (A,B,D,E) data are plotted as mean $\pm$ SD. Statistical significance is relative to normoxia (A,B,D) or (-) citrate (E) as determined by two-sided Student's t-test with *, P value < 0.05; **, P value < 0.01; ***, P value < 0.001, ****, P value < 0.0001. In (C) data are plotted as mean $\pm$ 95% confidence interval (CI). Statistical significance by non-overlapping confidence intervals, *. Unless indicated, all data represent biological triplicates. Data shown are from one of at least two separate experiments.

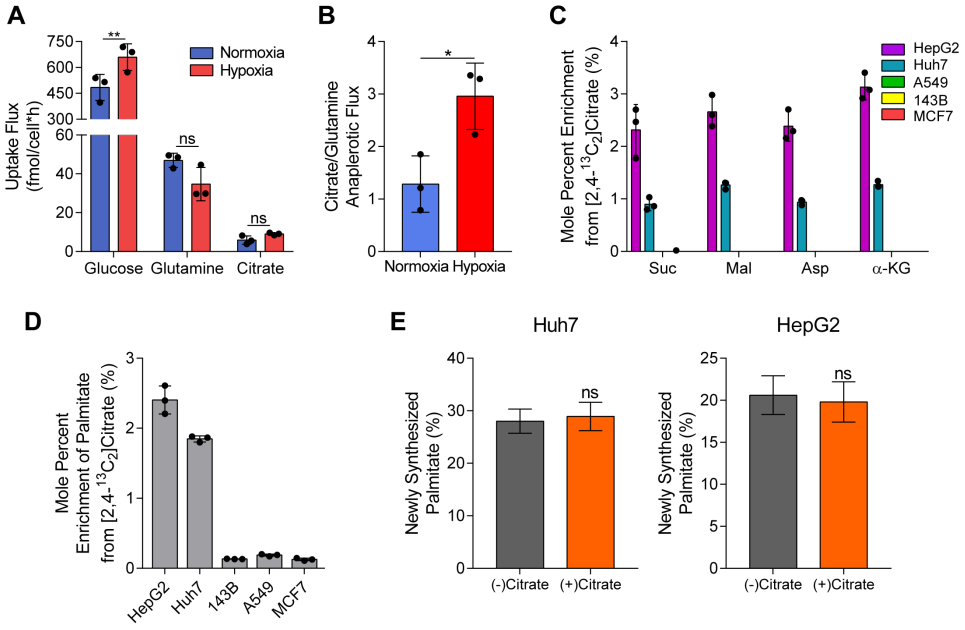

Figure S1.2: **Exogenous citrate is metabolized for TCA anaplerosis and fatty acid synthesis. Related to Figure 3.** A) Glucose, glutamine, and citrate uptake flux over 48 hours in Huh7 cells grown in normoxia or hypoxia (n=3). B) Ratio of net citrate to anaplerotic glutamine flux over 48 hours in Huh7 cells grown in normoxia or hypoxia. Anaplerotic flux of glutamine calculated by subtracting media glutamate efflux from glutamine uptake (n=3). C) Mole percent enrichment of TCA intermediates from 500 μM [2,4-$^{13}C_2$]citrate in cancer cells grown in hypoxia for 48 hours (n=3). D) Palmitate mole percent enrichment from 500 μM [2,4-$^{13}C_2$]citrate in cancer cells grown in hypoxia for 48 hours (n=3). E) De novo synthesis of palmitate $\pm$ 500 μM citrate in Huh7 (left) and HepG2 (right) cells grown in hypoxia over 48 hours (n=3). Suc, succinate; Mal, malate; Asp, aspartate; α-KG, α-ketoglutarate. In (A-D) data are plotted as mean $\pm$ SD. Unless indicated, all data represent biological triplicates. Statistical significance is relative to normoxia (A,B) as determined by two-sided Student's t-test with *, P value < 0.05; **, P value < 0.01; ***, P value < 0.001, ****, P value < 0.0001. In (E) data are plotted as mean $\pm$ 95% confidence interval (CI). Statistical significance by non-overlapping confidence intervals, *. Data shown are from one of at least two separate experiments.

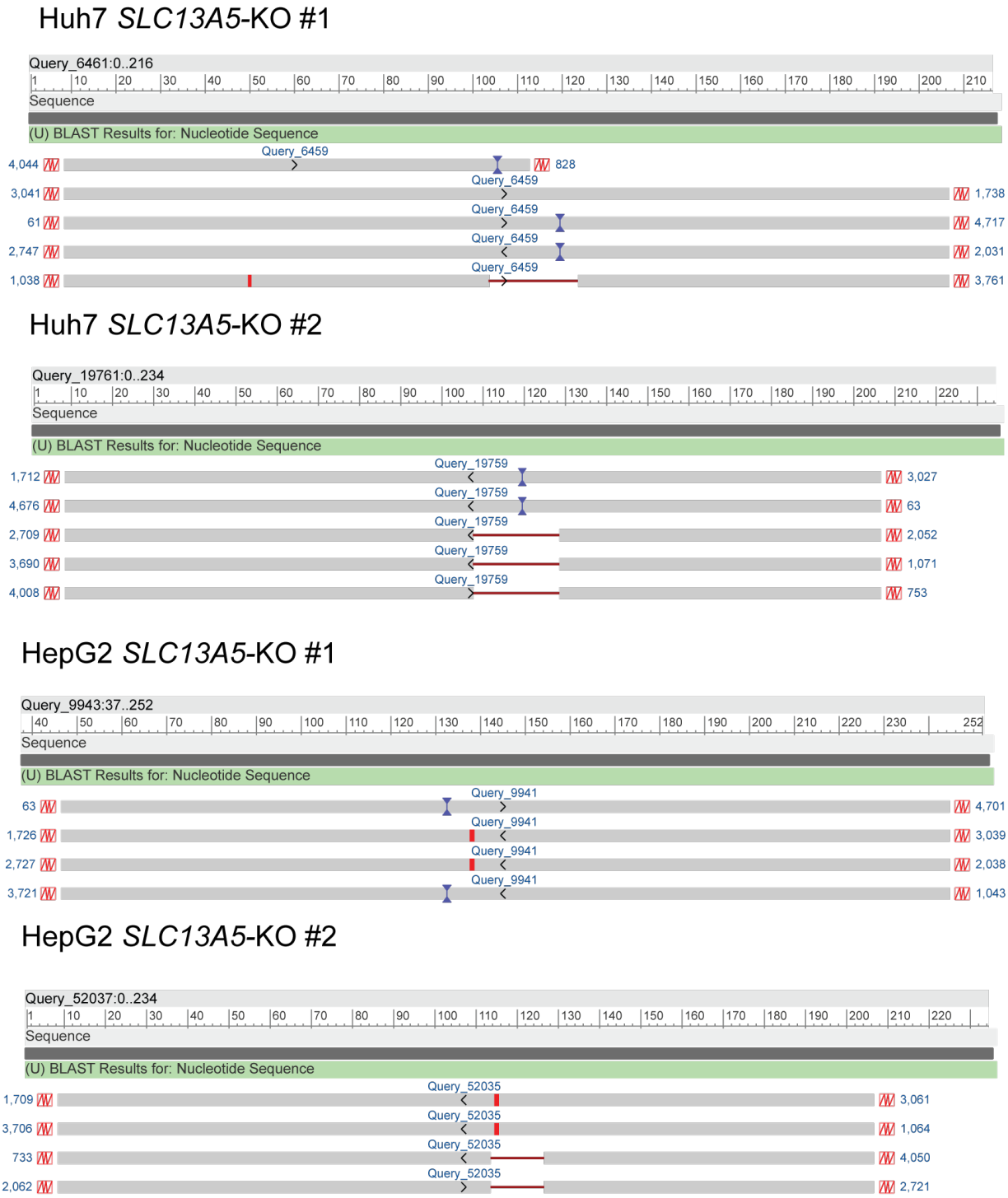

Figure S1.3: **Alignment of DNA sequences obtained from CRISPR/Cas9 HCC SLC13A5-KO clones. Related to Figure 5.** Sequences aligned using NCBI BLASTN suite [1]. Results were visualized using NCBI Viewer 3.41.1.

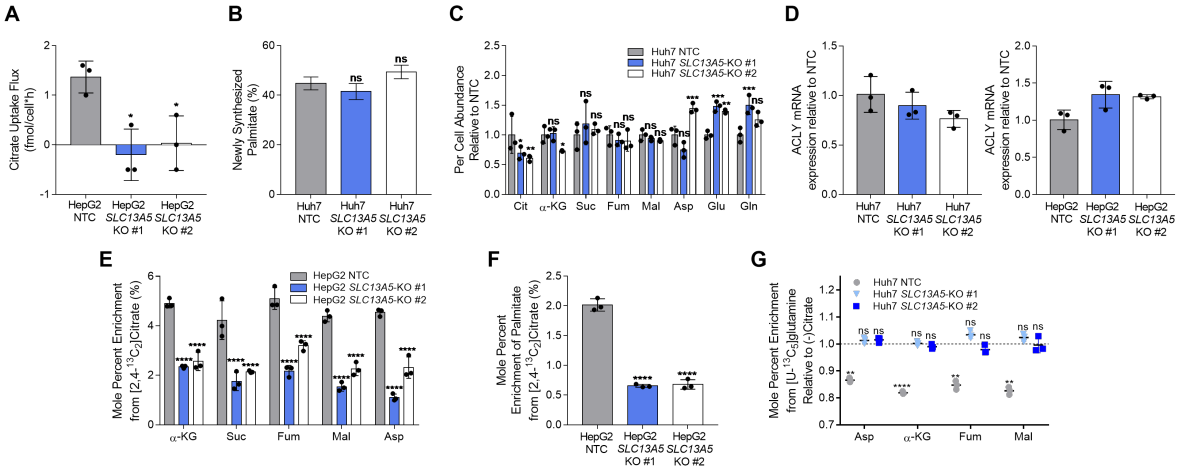

Figure S1.4: **NaCT supports extracellular citrate import and metabolism in hepatocellular carcinoma cells. Related to Figure 5.**A) Citrate uptake flux in HepG2 NTC and SLC13A5-KO cells grown in hypoxia for 48 hours (n=3). B) De novo synthesis of palmitate in Huh7 NTC and SLC13A5-KO cells grown in hypoxia for 48 hours (n=3). C) Per cell abundance of metabolites in Huh7 NTC and SLC13A5-KO cells grown in hypoxia for 48 hours, relative to NTC (n=3). D) ACLY mRNA expression in NTC and SLC13A5-KO Huh7 (left) and HepG2 (right) cells grown in normoxia, relative to NTC (n=3). E) Mole percent enrichment of TCA intermediates from [2,4-$^{13}C_2$]citrate in HepG2 NTC and SLC13A5-KO cells grown in hypoxia for 48 hours (n=3). F) Mole percent enrichment of palmitate from [2,4-$^{13}C_2$]citrate in HepG2 NTC and SLC13A5-KO cells grown in hypoxia for 48 hours (n=3). G) Mole percent enrichment of TCA intermediates from [U-$^{13}C_5$]glutamine in Huh7 NTC and SLC13A5-KO cells $\pm$ 500 μM citrate grown in hypoxia for 48 hours, relative to (-) citrate (n=3). Cit, citrate; α-KG, α-ketoglutarate; Suc, succinate; Fum, fumarate; Mal, malate; Asp, aspartate; Glu, glutamate; Gln, glutamine. In (A,C-F) all graphs data are plotted as mean $\pm$ SD. Statistical significance is relative to NTC as determined by One-way ANOVA w/ Dunnet's method for multiple comparisons (A,C-F) or relative to (-) citrate as determined by two-sided Student's t-test (G) with *, P value < 0.05; **, P value < 0.01; ***, P value < 0.001, ****, P value < 0.0001. In (B) data are plotted as mean $\pm$ 95% confidence interval (CI). Statistical significance by non-overlapping confidence intervals, *. Unless indicated, all data represent biological triplicates. Data shown are from one of at least two separate experiments.

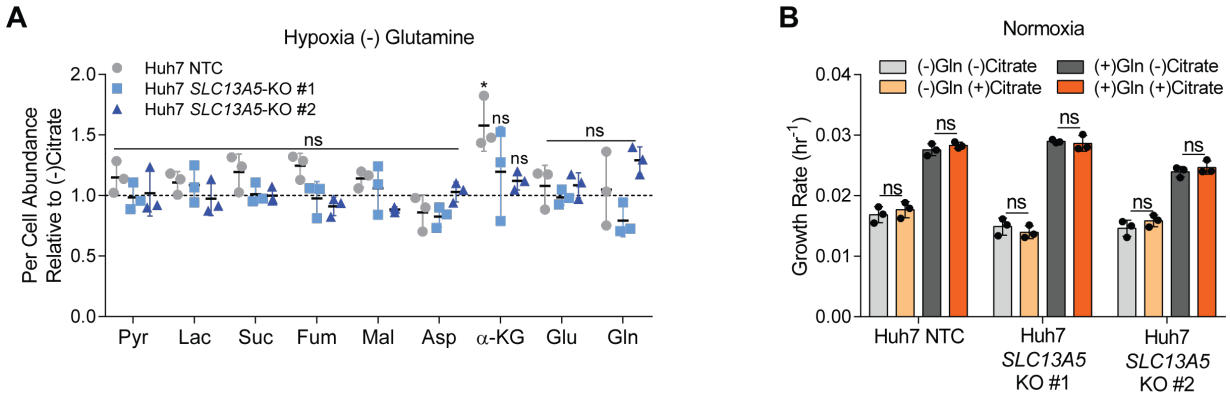

Figure S1.5: **NaCT facilitates growth under nutrient stress and resistance to zinc toxicity. Related to Figure 6.** A) Per cell abundances of central carbon metabolites in Huh7 NTC and SLC13A5-KO cells grown without glutamine in hypoxia $\pm$ 500 μM citrate for 48 hours, relative to (-) citrate (n=3). B) Growth rates of Huh7 NTC and SLC13A5-KO cells grown in high glucose DMEM $\pm$ 4mM glutamine $\pm$ 500 μM citrate in normoxia for 4 days (n=3). Pyr, pyruvate; Lac, lactate; Suc, succinate; Fum, fumarate; Mal, malate; Asp, aspartate; α-KG, α-ketoglutarate; Glu, glutamate; Gln, glutamine. In all graphs data are plotted as mean $\pm$ SD. Statistical significance is determined by two-sided Student's t-test relative to (-) citrate (A); or determined by Two-way ANOVA w/ Tukey's method for multiple comparisons relative to (-) citrate (B) with *, P value < 0.05; **, P value < 0.01; ***, P value < 0.001, ****, P value < 0.0001. Unless indicated, all data represent biological triplicates. Data shown are from one of at least two separate experiments.

Chapter S2

Supplement to Chapter 3

S2.1 Supplemental Tables and Figures

Table S2.1: **Metabolite fragments considered in MFA. Related to Figure 4.**

Metabolite	Carbons	Formula	Mass (m/z)
Pyruvate	1,2,3	$C_6H_{12}O_3NSi$	174
Lactate	2,3	$C_{10}H_{25}O_2Si_2$	233
Lactate	1,2,3	$C_{11}H_{25}O_3Si_2$	261
Alanine	2,3	$C_{10}H_{26}ONSi_2$	232
Alanine	1,2,3	$C_{11}H_{26}O_2NSi_2$	260
α-KG	1,2,3,4,5	$C_{14}H_{28}O_5NSi_2$	346
Malate	1,2,3,4	$C_{18}H_{39}O_5Si_3$	419
Succinate	1,2,3,4	$C_{12}H_{25}O_4Si_2$	289
Fumarate	1,2,3,4	$C_{12}H_{23}O_4Si_2$	287
Aspartate	1,2	$C_{14}H_{32}O_2NSi_2$	302
Glutamate	1,2,3,4,5	$C_{19}H_{42}O_4NSi_3$	432
Glutamine	1,2,3,4,5	$C_{19}H_{43}O_3N_2Si_3$	431
Palmitate	1-16	$C_{17}H_{34}O_2$	270

Table S2.2: **Oligonucleotide sequences used in this study. Related to Figures 1 and 5.**

Primer name	Sequence	Application
ACLY (human) fwd	TCGGCCAAGGCAATTTCAGAG	qRT-PCR
ACLY (human) rev	CGAGCATACTTGAACCGATTCT	qRT-PCR
SLC13A5 (human) fwd	CTGCCACTCGTCATTCTGATG	qRT-PCR
SLC13A5 (human) rev	ATGTTGGTGTCCTTCATGTACTG	qRT-PCR
r18s (human) fwd	AGTCCCTGCCCTTTGTACACA	qRT-PCR
r18s (human) rev	CGATCCGAGGGCCTCACTA	qRT-PCR
Slc13a5 (rat) fwd	GGTGCACAGATGTCATCCCA	qRT-PCR
Slc13a5 (rat) rev	AGCATGTTGGTGTCCGTCAT	qRT-PCR
r18s (rat) fwd	AGAAACGGCTACCACATCCA	qRT-PCR
r18s (rat) rev	CTCGAAAGAGTCCTGTATTGT	qRT-PCR
SLC13A5 (human) PCR fwd	AGGCATCCCATAGTGACCCT	Target Site PCR Primer
SLC13A5 (human) PCR rev	CACAGAACTGCCGGAGTTGT	Target Site PCR Primer

Figure S2.1: ***ACLY*-KO rewires central carbon metabolism and leads to a reduction of palmitate synthesis in cancer cells, related to Figure 1.** A) Western blots of ACLY, ACSS2, and actin in WT and *ACLY*-KO HepG2 (left), HAP1 (middle), and 634T (right) cells. B) Growth rates of WT and *ACLY*-KO HepG2 (left), HAP1 (middle), and 634T (right) cells grown in high glucose DMEM +10% FBS for 4 days. C) Mole percent enrichment of TCA intermediates from [U-$^{13}C_6$]glucose in A549 *ACLY*-KO cells cultured in high glucose DMEM +10% dFBS for 72 hours (n=3). D) Schematic of extracellular [2,4-$^{13}C_2$]citrate catabolism. Filled circles are ^{13}C, empty circles are 12C. Faded metabolite labeling and arrows are reduced by ACLY knockout. E) Ratio of the relative abundance of M1/M2 TCA intermediates from [2,4-$^{13}C_2$]citrate in HepG2 WT and *ACLY*-KO cells cultured in high glucose DMEM +10% dFBS + 500 μM citrate for 72 hours (n=3). F) Mass isotopomer distribution of α-KG from [2,4-$^{13}C_2$]citrate in HepG2 WT and *ACLY*-KO cells cultured in high glucose DMEM +10% dFBS + 500 μM citrate for 72 hours (n=3). G) Enrichment (1-M0) of palmitate from [2,4-$^{13}C_2$]citrate in HepG2 WT and *ACLY*-KO cells cultured in high glucose DMEM +10% dFBS + 500 μM citrate for 72 hours (n=3). H) De novo synthesis of palmitate in WT and *ACLY*-KO HepG2 (left) and 634T (right) cells cultured in high glucose DMEM +10% dFBS (n=3). I) Mole percent enrichment of palmitate from [U-$^{13}C_6$] glucose in HAP1 WT and *ACLY*-KO cells cultured in high glucose DMEM +10% dFBS (n=3). Enrichment of palmitate from glucose in the HAP1 *ACLY*-KO cell lines was too low to obtain precise DNL flux measurements, however, this lack of labeling suggests that *de novo* palmitate synthesis in the HAP1 cells is inhibited by *ACLY*-KO as well. J) Percent of lipogenic acetyl-CoA contributed by [U-$^{13}C_6$]glucose in WT and *ACLY*-KO HepG2 (left) and 634T (right) cells cultured in high glucose DMEM +10% dFBS (n=3). In (B,C,E-G, and I) data are plotted as mean $\pm$ SD. Statistical significance is relative to WT as determined by One-way ANOVA w/ Dunnet's method for multiple comparisons with *, P value < 0.05; **, P value < 0.01; ***, P value < 0.001, ****, P value < 0.0001. In (H, J) data are plotted as mean $\pm$ 95% confidence interval (CI). Statistical significance by non-overlapping confidence intervals, *. Unless indicated, all data represent biological triplicates. Data shown are from one of at least two separate experiments.

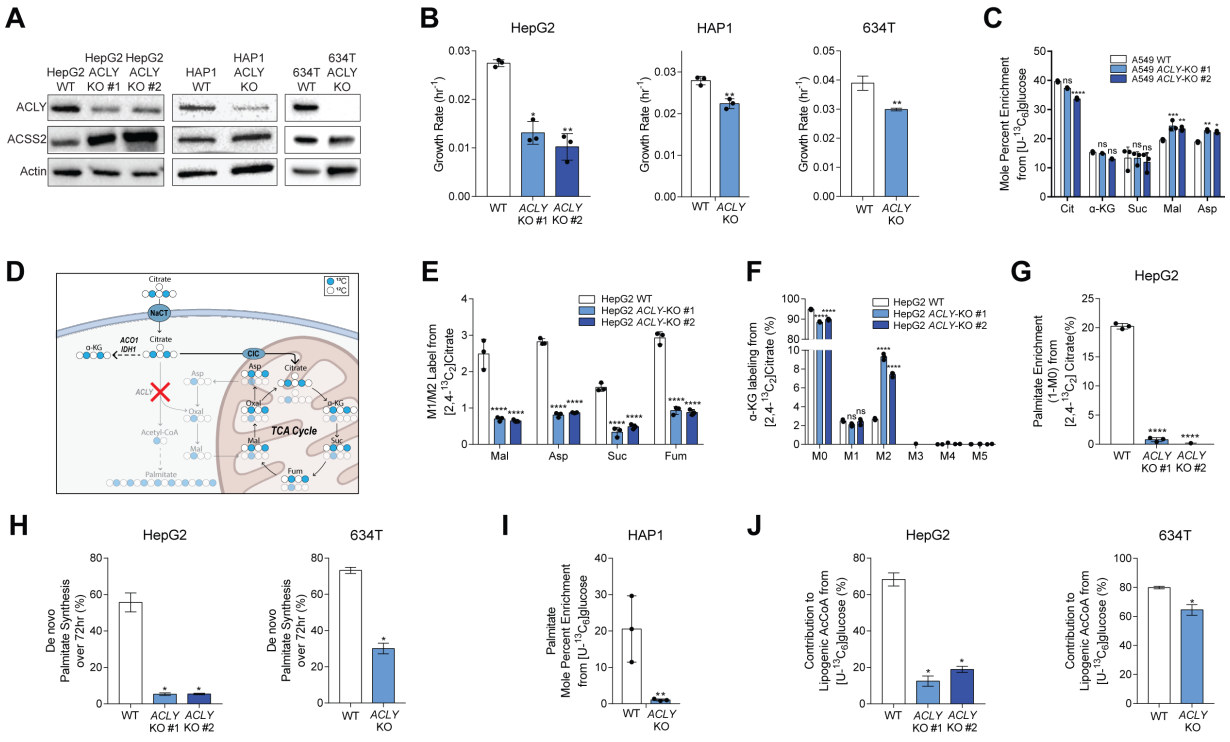
A
HepG2 WT
HepG2 ACLY KO #1
HepG2 ACLY KO #2
HAP1 WT
HAP1 ACLY KO
634T WT
634T ACLY KO
ACLY
ACSS2
Actin
B
HepG2
HAP1
634T
Growth Rate (hr-1)
WT
ACLY KO #1
ACLY KO #2
ACLY KO
C
A549 WT
A549 ACLY-KO #1
A549 ACLY-KO #2
Mole Percent Enrichment from [U-13C6]glucose
Cit
α-KG
Suc
Mal
Asp
D
Citrate
NaCT
ACO1
IDH1
α-KG
CIC
ACLY
Oxal
Acetyl-CoA
Mal
Palmitate
Asp
Fum
TCA Cycle
E
HepG2 WT
HepG2 ACLY-KO #1
HepG2 ACLY-KO #2
M1/M2 Label from [2,4-13C2]Citrate
Mal
Asp
Suc
Fum
F
α-KG labeling from [2,4-13C2]Citrate (%)
M0
M1
M2
M3
M4
M5
G
HepG2
Palmitate Enrichment (1-M0) from [2,4-13C2] Citrate(%)
H
HepG2
634T
De novo Palmitate Synthesis over 72hr (%)
I
HAP1
Palmitate Mole Percent Enrichment from [U-13C6]glucose
J
HepG2
634T
Contribution to Lipogenic AcCoA from [U-13C6]glucose (%)

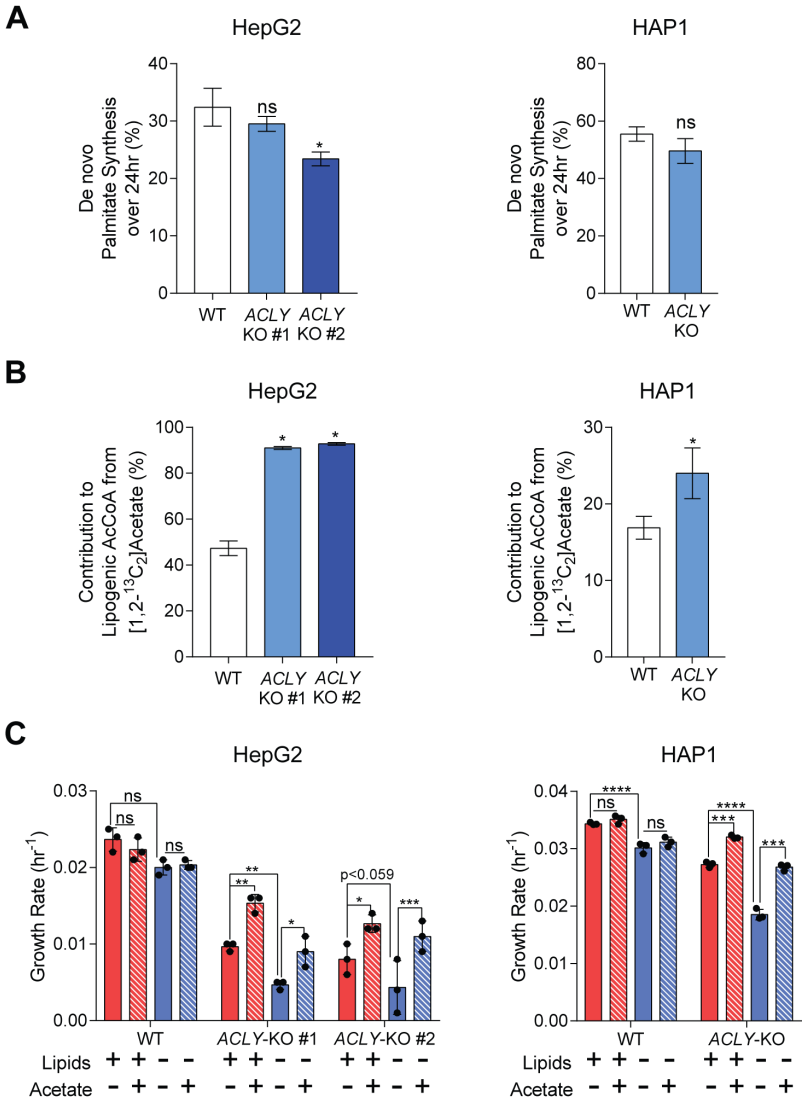

Figure S2.2: ***ACLY*-KO growth and fatty acid synthesis is rescued with addition of extracellular acetate, related to Figure 2.** A) De novo synthesis of palmitate in HepG2 (left) and HAP1 (right) WT and *ACLY*-KO cells cells cultured in high glucose DMEM +10% dFBS + 1 mM acetate for 24 hours (n=3). B) Percent of lipogenic acetyl-CoA contributed by [1,2-$^{13}C_2$]acetate in HepG2 (left) and HAP1 (right) WT and *ACLY*-KO cells cultured in high glucose DMEM +10% dFBS + 1 mM acetate for 24 hours (n=3). C) Growth rates of HepG2 (left) and HAP1 (right) and WT and *ACLY*-KO cells grown in high glucose DMEM +10% dFBS or delipidated dFBS $\pm$ 1 mM acetate for 4 days (n=3). In (A, B) data are plotted as mean $\pm$ 95% confidence interval (CI). Statistical significance by non-overlapping confidence intervals, *. In (C) data are plotted as mean $\pm$ SD. Statistical significance is determined by Two-way ANOVA w/ Tukey's method for multiple comparisons with *, P value < 0.05; **, P value < 0.01; ***, P value < 0.001, ****, P value < 0.0001. Unless indicated, all data represent biological triplicates. Data shown are from one of at least two separate experiments.

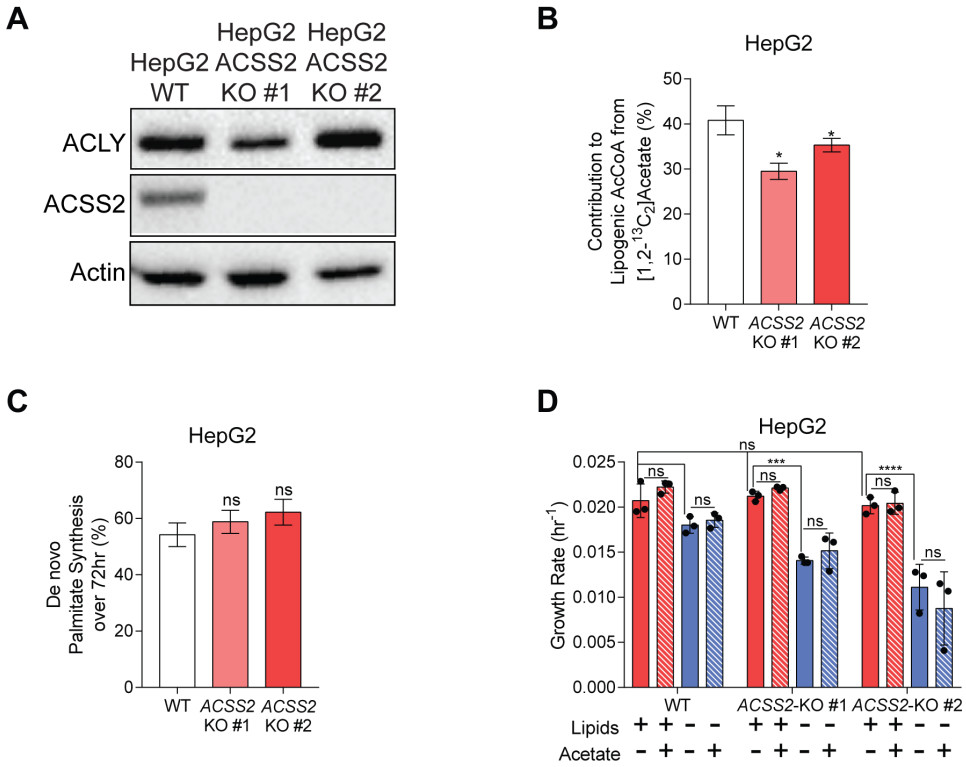

Figure S2.3: ***ACSS2*-KO attenuates catabolism of exogenous acetate with minimal effect on glucose catabolism, related to Figure 3.** A) Western Blots of ACLY, ACSS2, and actin in HepG2 WT and *ACSS2*-KO cells. B) Percent of lipogenic acetyl-CoA contributed by [1,2-$^{13}C_2$] acetate in HepG2 *ACSS2*-KO cells cultured in high glucose DMEM +10% dFBS + 1 mM acetate for 24 hours (n=3). C) De novo synthesis of palmitate in HepG2 *ACSS2*-KO cells cultured in high glucose DMEM +10% dFBS for 72 hours (n=3). D) Growth rates of HepG2 WT and *ACSS2*-KO cells grown in high glucose DMEM +10% dFBS or delipidated dFBS $\pm$ 1 mM acetate for 4 days (n=3). In (B, C) data are plotted as mean $\pm$ 95% confidence interval (CI). Statistical significance by non-overlapping confidence intervals, *. In (D) data are plotted as mean $\pm$ SD. Statistical significance is determined by Two-way ANOVA w/ Tukey's method for multiple comparisons (D) with *, P value < 0.05; **, P value < 0.01; ***, P value < 0.001, ****, P value < 0.0001. Unless indicated, all data represent biological triplicates. Data shown are from one of at least two separate experiments.

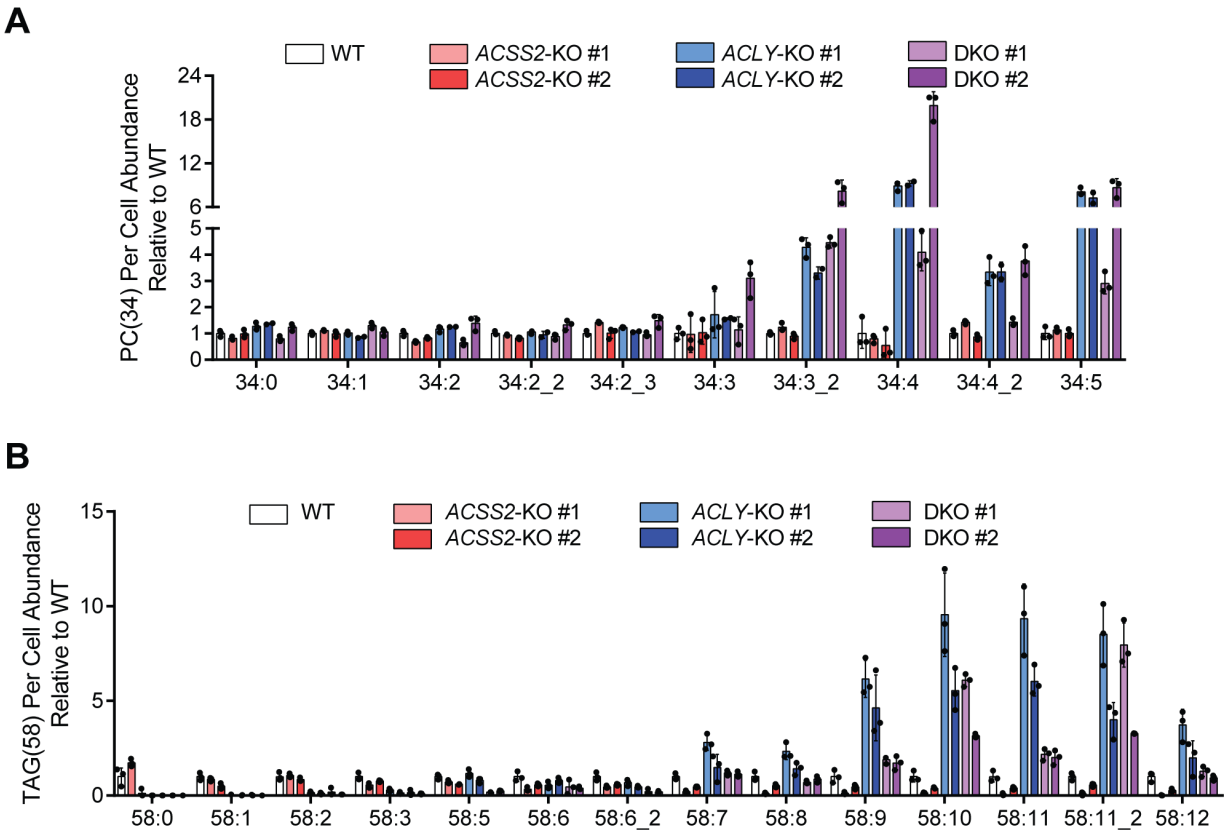

Figure S2.4: ***ACLY/ACSS2*- cells are reliant on extracellular lipids, with minimal change in protein acetylation, related to Figure 4.**A) PC(34) per cell abundance of A549 WT, *ACSS2*-KO, *ACLY*-KO, *ACLY/ACSS2*-DKO cells cultured in high glucose DMEM +10% FBS for 2 days (n=3). B) TAG(58) per cell abundance of A549 WT, *ACSS2*-KO, *ACLY*-KO, *ACLY/ACSS2*-DKO cells cultured in high glucose DMEM +10% FBS for 2 days (n=3). Data are plotted as mean ± 95% confidence interval (CI). Unless indicated, all data represent biological triplicates.

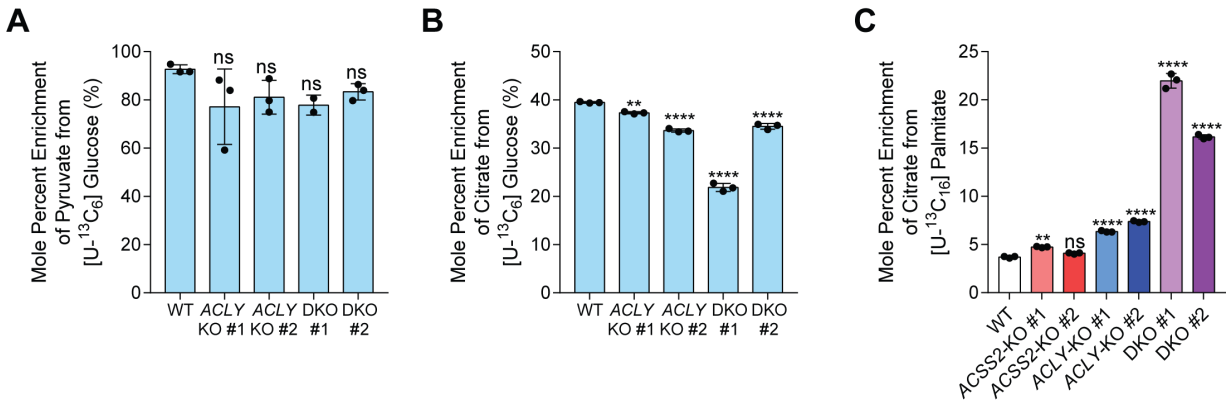

Figure S2.5: **Disruption of canonical acetyl-CoA synthesis induces alternative synthesis pathways, related to Figure 5.** A) Mole percent enrichment of pyruvate from [U-$^{13}C_6$] glucose in A549 WT, *ACLY*-KO, *ACLY/ACSS2*-DKO cells cultured in high glucose DMEM +10% dFBS for 72 hours (n=3). B) Mole percent enrichment of citrate from [U-$^{13}C_6$] glucose in A549 WT, *ACLY*-KO, *ACLY/ACSS2*-DKO cells cultured in high glucose DMEM +10% dFBS for 72 hours (n=3). C) Mole percent enrichment of citrate from [U-$^{13}C_{16}$] palmitate in A549 WT, *ACSS2*-KO, *ACLY*-KO, *ACLY/ACSS2*-DKO cells (n=3). Data are plotted as mean $\pm$ SD. Statistical significance relative to WT as determined by One-way ANOVA w/ Dunnet's method for multiple comparisons with *, P value < 0.05; **, P value < 0.01; ***, P value < 0.001, ****, P value < 0.0001. Unless indicated, all data represent biological triplicates. Data shown are from one of at least two separate experiments.

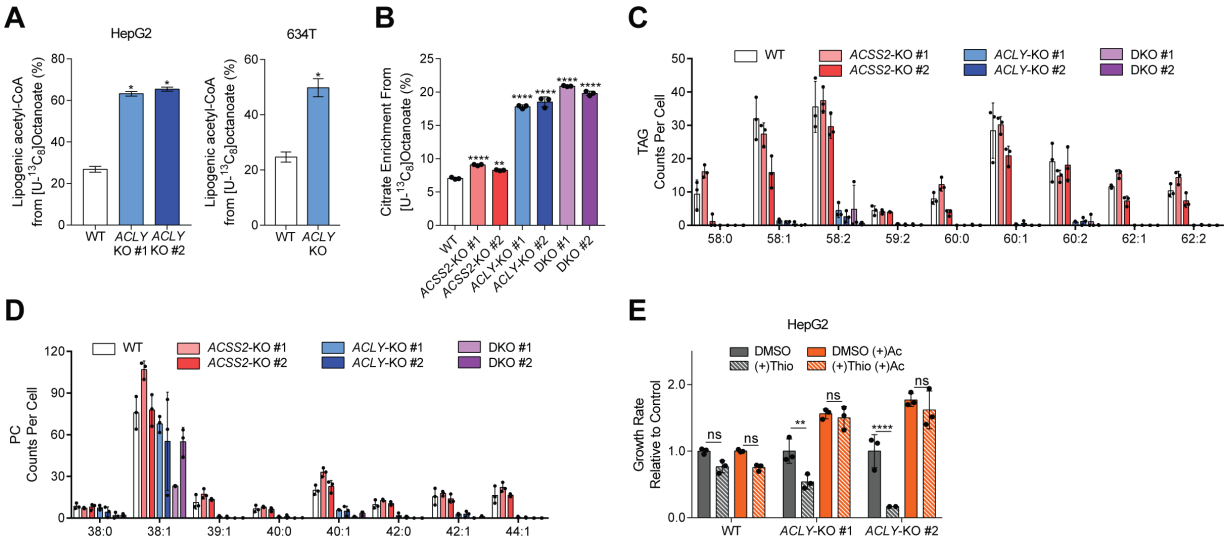

Figure S2.6: **Peroxisomal β-oxidation becomes a major source of lipogenic acetyl-CoA with ACLYKO and *ACLY/ACSS2* DKO, related to Figure 6.** A) Percent of lipogenic acetyl-CoA contributed by [U-$^{13}C_8$] octanoate in WT and *ACLY*-KO HepG2 (left) and 634T (right) cells cultured in high glucose DMEM +10% dFBS + 500 μM octanoate for 24 hours (n=3). B) Mole percent enrichment of citrate from [U-$^{13}C_8$] octanoate in A549 WT, *ACSS2*-KO, *ACLY*-KO, *ACLY/ACSS2*-DKO cells cultured in high glucose DMEM +10% dFBS + 500 μM octanoate for 24 hours (n=3). C) Saturated, mono- and di-unsaturated TAG per cell abundances of A549 WT, *ACSS2*-KO, *ACLY*-KO, *ACLY/ACSS2*-DKO cells cultured in high glucose DMEM +10% FBS 2 days (n=3). D) Saturated and monounsaturated PC per cell abundances of A549 WT, *ACSS2*-KO, *ACLY*-KO, *ACLY/ACSS2*-DKO cells cultured in high glucose DMEM +10% FBS 2 days (n=3). E) Growth rates of HepG2 WT and *ACLY*-KO cells grown in high glucose DMEM +10% dFBS $\pm$ 2.5 μM thioridazine $\pm$ 1 mM acetate for 4 days (n=3). In (A) data are plotted as mean $\pm$ 95% confidence interval (CI). Statistical significance by non-overlapping confidence intervals, *. In (B-E) data are plotted as mean $\pm$ SD. Statistical significance as determined by One-way ANOVA w/ Dunnet's method for multiple comparisons relative to WT(A,B), or DMSO (E) with *, P value < 0.05; **, P value < 0.01; ***, P value < 0.001, ****, P value < 0.0001. Unless indicated, all data represent biological triplicates. Data shown are from one of at least two separate experiments.